Dynamics of strain and domains in single crystal and ceramic ferroelectrics under an alternating electric field using stroboscopic time-resolved X-ray diffraction

DISSERTATION

zur Erlangung des Grades eines Doktors der Naturwissenschaften

vorgelegt von

M. Sc. Hyeokmin Choe

eingereicht bei der Naturwissenschaftlich-Technische Fakultät, Physik

der Universität Siegen

Siegen 2018

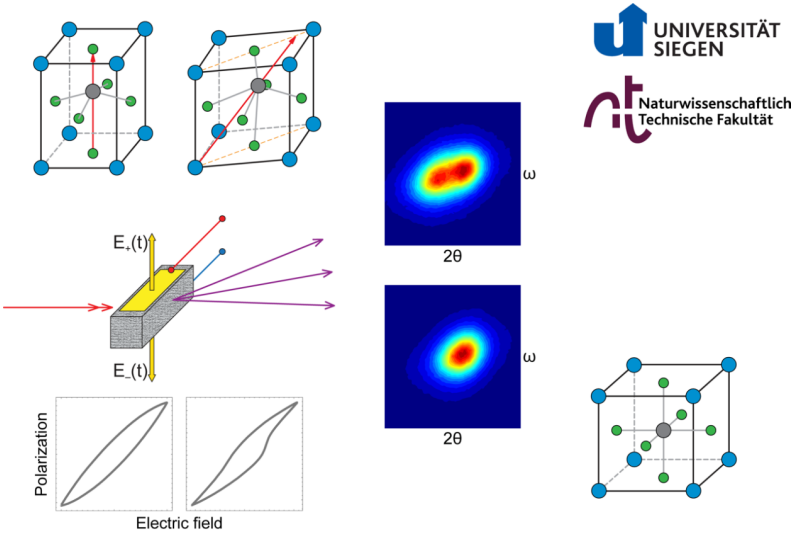

Gutachter:

Prof. Ullrich Pietsch

Prof. Semën Gorfman

Prüfer:

Prof. Hugh Simons

Prof. Otfried Gühne

Tag der mündichen Prüfung:

February 26, 2018

Abstract

CHOE, HYEOKMIN. Dynamics of strain and domains in single crystal and ceramic ferroelectrics under an alternating electric field using stroboscopic time-resolved X-ray diffraction

It is known that the dynamics of ferroelectric materials can be seen over a range of macroscopic, microscopic, and mesoscopic length scales. Thus, the response time of ferroelectrics due to an external perturbation will change on each specific length scale. In particular, the atomic dynamics occurs much faster compared to the response of the macroscopic lattice, whereas time scales of mesoscopic dynamics are a mixture ranging from the nano- to the milli-second regime. Developing an experimental method that covers multiple time scales allows for selective identification of the specific changes on each time scale and their influence on the ferroelectrics. If an experimental approach can be developed with multiple time resolutions, the response of the ferroelectrics can be selectively identified the dominant time and length scales under an external perturbation. Stroboscopic time-resolved X-ray diffraction is a very powerful tool to probe dynamical changes in ferroelectrics. Using a multi-channel analyzer data-acquisition system with nanosecond time resolution opens the possibility of observing the dynamics of ferroelectrics on multiple length scales. This state-of-the-art method allows for a better understanding of the dynamic processes in ferroelectrics and provides new insights for the design of advanced (e.g. smart and environmentally friendly) functional materials.

The development of the new data-acquisition systems and their applications in stroboscopic time-resolved X-ray diffraction are described in Chapter 4. Chapter 5 studies the relationship between the piezoelectricity and the polarization rotation of $Na_{0.5}Bi_{0.5}TiO_3$ (NBT) single crystal under an alternating electric field using synchrotron-based time-resolved high-resolution reciprocal space mapping. Chapter 6 investigates the origin of the enhanced piezoelectric activity in uniaxial $Sr_{0.5}Ba_{0.5}Nb_2O_6$ (SBN50) ferroelectrics. Chapter 7 discusses the mechanism of the electric field-induced polarization reversal and strain in perovskite-based $0.94BaTiO_3$-$0.06BiZn_{0.5}Ti_{0.5}O_3$ (BT-BZT) ferroelectric ceramics under an alternating electric field using stroboscopic time-resolved high-energy X-ray powder diffraction.

Zusammenfassung

CHOE, HYEOKMIN. Dynamik der Dehnung und Domänen im Einkristall- und Keramik-Ferroelektrika unter einem alternierenden elektrischen Feld mit Hilfe der stroboskopischen zeitaufgelösten Röntgenbeugung

Es ist bekannt, dass die Dynamik von ferroelektrischen Materialien über eine Reihe von makroskopischen, mikroskopischen und mesoskopischen Längenskalen beobachtet werden kann. Deshalb ändert sich die Ansprechzeit der Ferroelektrika aufgrund einer externen Störung auf jeder der spezifischen Längenskalen. Insbesondere tritt die Dynamik des atomaren Gitters im Vergleich zur Antwort des makroskopischen Gitters wesentlich schneller auf, während die Zeitskalen der mesoskopischen Dynamik im Bereich von Nano- bis zu Milli-Sekunden liegen. Die Entwicklung einer experimentellen Methode, die multiple Zeitskalen umfasst, ermöglicht die selektive Identifikation der spezifischen Änderungen auf jeder Der genannten Zeitskalen und ihrem Einfluss auf das Ferroelektrikum. Wenn es gelänge, einen experimentellen Ansatz mit den multiplen Zeitauflösungen zu entwickeln, Könnte man die jeweils dominante Zeit- und Längenskala für die Antwort der Ferroelektrika unter Einfluß einer externen Störung selektiv Identifizieren. In dieser Arbeit wird gezeigt, daß die strobiskopische zeitaufgelöste Röntgenbeugung ein sehr mächtiges Instrument ist, um dynamische Änderungen in Ferroelektrika zu untersuchen. Die Verwendung eines Mehrkanal-Analysator-Datenerfassungssystems mit Nanosekunden-Zeitauflösung eröffnet die Möglichkeit, um die Dynamik der Ferroelektrika auf multiplen Längenskalen zu beobachten. Diese hochmoderne Methode ermöglicht ein besseres Verständnis der dynamischen Prozesse in Ferroelektrika und bietet eine neue Einsicht in das Design fortschrittlicher (z. B. intelligenter und umweltfreundlichen) Funktionsmaterialien.

Die Entwicklungen von neuen Datenerfassungssystemen und ihre Anwendungen in der stroboskopischen zeitaufgelösten Röntgenbeugung werden in Kapitel 4 beschrieben. Kapitel 5 diskutiert die Beziehung zwischen Piezoelektrizität und Polarisationsrotation von $Na_{0.5}Bi_{0.5}TiO_3$ (NBT) Einkristallen unter einem alternierenden elektrischen Feld mit Hilfe Synchrotron-basierter, zeitaufgelöster und hochauflösender reziproker Gitterkarten. Kapitel 6 zeigt den Ursprung der verstärkten piezoelektrischen Aktivität in uniaxialen $Sr_{0.5}Ba_{0.5}Nb_2O_6$ (SBN50) Ferroelektrika. Kapitel 7 beschreibt der Mechanismus der elektrischen Feld-induzierten Polarisationsumkehr und die Dehnung in Perovskit-basierten $0.94BaTiO_3$-$0.06BiZn_{0.5}Ti_{0.5}O_3$ (BT-BZT) ferroelektrischen

Keramiken, unter einem alternierenden elektrischen Feld bei gleichzeitiger Verwendung der stroboskopischen zeitaufgelösten hochenergetischen Röntgenpulverbeugung.

Table of Contents

Chapter 1

Introduction – It is time to explore the exciting new world!

1.1. Motivation

The investigation of structural dynamics in modern functional materials has attracted both fundamental and material scientists because the structural response of a material to external perturbations (e.g. electric field, mechanical stress or change of temperature) characterizes its physical or/and chemical properties. The representative functionalities of materials, which express their response to electrical perturbations, are *piezoelectricity* and *ferroelectricity*.

- *Piezoelectricity* is an ability to convert electrical energy into mechanical energy and *vice versa*. The direct piezoelectric effect is a dielectric response to a mechanical perturbation, on the other hand, the converse piezoelectricity is a mechanical response to an external electrical perturbation.

- *Ferroelectricity* describes the property of a material to develop spontaneous polarization in the absence of an external electric field. This polarization can be switched (e.g. inverted) by applying an electric field against the polarization direction. Sometimes the polarization can be switched between more than two energetically equivalent states corresponding to a minimum of the free energy in the material under the application of an external electric field.

The functionalities can be seen in such material as $BaTiO_3$ and $Pb(Zr,Ti)O_3$, since the discovery of ferroelectricity from Rochelle salts by Valasek in 1921 [1]. Ferroelectric materials have been applied in many devices (e.g. actuators, sensors, frequency generators, and car fuel injectors, etc.) due to their useful physical properties such as electromechanical coupling (e.g. piezoelectricity and electrostriction). Despite applications in many devices, the functionalities in ferroelectrics remain a long-lasting research subject. Understanding the physical properties in ferroelectrics will eventually lead to an improved design of, and allow for the development of advanced (e.g. smart and environmental friendly), new materials. It is known that the dynamics of physical properties in ferroelectrics involves different – microscopic, macroscopic, and mesoscopic – length and time scales. The atomic dynamics are much faster compared to the macroscopic lattice responses. On the other hand, the mesoscopic dynamics are

very likely to range between the corresponding macroscopic and atomic values. Their corresponding time scales spread from the nano- to the milli-second regime. Therefore, many experiments have been performed in an attempt to observe all these processes in real time. However, the conventional techniques have limited capability to explore all the processes simultaneously. For example, optical microscopy, transmission electron microscopy (TEM), and piezoelectric force microscopy (PFM) are able to probe surfaces but they have limited sensitivity to measure the lattice parameters. X-ray diffraction methods have been used to overcome these limitations due to their ability to cover a broad range of length scales. X-ray diffraction can measure crystal lattice parameters. Since the electric field-induced atomic displacements are relatively small with respect to the inter-atomic distances, conventional X-ray diffraction is not sensitive enough. In order to overcome this disadvantage, *in situ* experiments, in particular stroboscopic time-resolved X-ray diffraction methods, were used instead. In general, the stroboscopic techniques involve the application of a repetitive external perturbation and the collection of the repeatable responses of a material. In other words, the small response of the material to the external perturbation can be measured by summing up during multiple cycles. This technique is very useful for *in situ* data collection during measurement of functional materials under an alternating electric field. However, the methods for stroboscopic time-resolved X-ray diffractions are not yet fully developed.

The aim of this work is the development of a stroboscopic time-resolved X-ray diffraction method for studying strain and domain dynamics in ferroelectric single crystals and ceramics under an alternating external electric field.

1.2. Stroboscopic time-resolved diffraction methods

One of the stroboscopic time-resolved X-ray diffraction methods uses a multi-channel analyzer data-acquisition system which is explained in more detail in Chapter 4.

Pioneering works on the subject of the stroboscopic time-resolved diffraction methods using the multi-channel analyzer were carried out by Puget & Godefroy [2], Lissalde & Peuzin [3], and Fujimoto [4–6]. Pietsch & Unger [7] firstly applied this technique to study the changing of the bond charges of GaAs to an external electric field. Paturle et al. [8] developed the 3-step modulation method to synchronize the signal from the single-photon counter with the applied 3-step – positive, zero, and negative – electric fields. This method was successfully used to investigate piezoelectric properties under external perturbations in the 1990s [9–14]. Guillot et al. [15] developed a new data-

acquisition system with four time-channels, which can modulate four different field steps. Afterwards, this system was used by many research studies, including von Reeuwijk et al. [16,17], Larsson et al. [18], and Hansen et al. [19] to study electric field-induced piezoelectric/ferroelectric responses. At the same time, Gorfman et al. [20–22] and Schmidt et al. [23] successfully developed a new system with 10000 channels and 100 nanosecond resolution enabling the investigation of the dynamics of piezoelectric/ferroelectric responses down to the sub-microseconds time scale [24,25].

Another type of stroboscopic method is based on the pump-probe technique. This method is implemented by using a bunch-structured modern synchrotron X-ray source. It is essential to synchronize between the periodic external perturbation(s) (pump) and the repeated X-ray bunch(s) (probe). X-ray diffraction is measured by using these probe pulses with a certain delay time relative to the pump pulses. The measurement is repeated for many different delay times, i.e. the time resolution of an experiment can be defined by each width of the probe pulses and the delay times between pump and probe pulses. According to the state-of-the-art of modern synchrotron facilities, the width of the X-ray bunches ranges between 44–60 ps [26–28]. The X-ray single bunches are generally repeated with a certain frequency depending on the operation modes in synchrotron facilities. Since modern pixel area detectors (e.g. Pilatus, Eiger, etc.) can be gated with an opening time less than the given time period, this pump-probe technique has also been implemented in various studies of dynamical responses in ferroelectrics, especially for thin film materials.

To summarize, the multi-channel analyzer allows for the utilization of a full X-ray beam, which gives the option of working without a beam chopper or a bunch structure, thus this data-acquisition system can be implemented at a synchrotron and neutron source, or even at a home-laboratory diffractometer system. On the other hand, the pump-probe technique requires a bunch-structured X-ray beam.

1.3. Structural dynamics study of strain and domains in ferroelectrics using stroboscopic time-resolved diffraction techniques

The introduced stroboscopic time-resolved X-ray diffraction methods in the previous section have been widely implemented for the investigation of dynamics in ferroelectrics. This section reviews the previous studies on structural dynamics of strain

and domains in ferroelectrics using stroboscopic time-resolved diffraction methods. For the purpose of clarification, this review divides into three categories based on the materials system used: (1) ferroelectric thin films, (2) bulk ceramics, and (3) bulk single crystals.

1.3.1. Ferroelectric thin films

Ferroelectric thin films have recently attracted interest due to their numerous applications in electronic devices such as ferroelectric random-access memories (FeRAMs) and piezoelectric microelectromechanical systems (Piezo-MEMS) for next-generation computers and telecommunication devices. Since these devices are working at high frequencies, it is important to understand their dynamical response in the pico- and the nano-second time regime. Zolotoyabko et al. [29] observed the field-induced lattice distortion of $BaTiO_3$ thin films under the application of a high-frequency electric field (~ sub-GHz) in order to investigate their structural relaxation. They improved the stroboscopic time-resolved X-ray diffraction with a pump-probe technique down to sub-nanosecond resolution and implemented it to measure the relaxation time at 72 ~ 521 MHz frequencies. Grigoriev et al. [30] developed a pump-probe time-resolved X-ray diffraction method to measure the piezoelectric response of $Pb(Zr,Ti)O_3$ (PZT) thin films using 10 ns electric pulses. The time resolution in this experiment was approached down to ~300 ps, allowing for the observation of the angular shift of the diffraction peak during the electrical pulse's leading/falling edge time scales. Sakata et al. [31] and Nakashima et al. [32] implemented the pump-probe time-resolved X-ray micro-diffraction method to determine the piezoelectric response time in a highly strained $BiFeO_3$ ferroelectric thin films under applied (~hundreds of nanoseconds) electric pulses. Jo et al. [33] used the time-resolved X-ray micro-diffraction to study periodically poled domain dynamics of $PbTiO_3/SrTiO_3$ superlattice thin films. They could observe the electric field-induced responses of striped ferroelectric domains from the satellite diffraction peaks on the nanosecond time scale. Chen et al. [34] successfully employed the time-resolved X-ray micro-diffraction to investigate electric field-induced strains in $BaTiO_3/CaTiO_3$ superlattice thin films from the nano- to the milli-second range, because the different piezoelectric response under those electric pulses can indicate an evidence of different ferroelectric processes. Fujisawa et al. [35] demonstrated direct observation of the intrinsic piezoelectric response of $Pb(Zr_{0.35},Ti_{0.65})O_3$ single crystal thin films under the applied (~hundreds of nanoseconds) electric pulses, and hence they improved the pump-probe time-resolved X-ray diffraction method to

measure simultaneously both the dielectric and the structural responses. The observed piezoelectric constants and electrostrictive coefficients agreed well with the expected theoretical values. Cosgriff et al. [36] implemented a time-resolved X-ray micro-diffraction to study the electric field-induced structural transformation of a highly strained $BiFeO_3$ thin film under applied sub-microsecond electric pulses. Accordingly, they successfully observed the structural transition between the rhombohedral-like and the tetragonal-like phases on the sub-microsecond time scale.

1.3.2. Bulk ceramics

Ferroelectric bulk ceramics are widely used in electromechanical applications not only due to their high piezoelectric response, but also because of their hysteretic and nonlinear properties. For this reason, many research studies have used *in situ* time-resolved diffraction methods to study the dynamical response of bulk ferroelectrics. Unlike the case of thin films, the response of bulk ceramics appears on much longer characteristic time scale. Jones et al. [37] and Daniels et al. [38] studied the domain wall motions in tetragonal PZT bulk ceramics under applied 1 Hz sub-coercive electric fields to limit the effect of induced fatigue. They measured the {002} powder diffraction peak profiles as a function of time and electric field. Based on the data they could correlate the change of the integrated intensity ratio (I_{002}/I_{200}) with a domain wall motion under the applied electric field. The authors successfully observed the dynamics of the electromechanical response with tens-of-microsecond resolution. Daniels et al. [39] and Pramanick et al. [40] did similar studies of the domain wall motion dynamics using a stroboscopic time-resolved X-ray diffraction method implementing a pixel area detector. Time resolution was 133 ms, which was limited by the acquisition frame rate of the used area detector. Pramanick et al. [41] implemented stroboscopic time-resolved neutron diffraction to observe the structural response of PZT bulk ceramics under cyclic electric fields in the frequency range between 1 and 500 Hz. They successfully obtained the lattice deformation from the {111} diffraction profiles with ~30 μs resolution. Jones et al. [42] and Tutuncu et al. [43] employed the stroboscopic time-resolved neutron diffraction method with the sub-millisecond resolution. They found that the diffraction peak separates during the application of cyclic electric fields between 0.01 and 10 Hz frequencies where the separation corresponds to different phases of $0.36BiScO_3$-$0.64PbTiO_3$ ceramics. Seshadri et al. [44] have reported on time-resolved neutron diffraction studies of tetragonal PZT ceramics with 10 μs resolution. The authors found that an enhanced extrinsic domain wall motion shows at low frequencies.

These stroboscopic time-resolved powder diffraction methods under an applied alternating electric field become more and more popular in the investigation of ferroelectric bulk ceramics [45–47].

1.3.3. Bulk single crystals

Harrison et al. [48] used stroboscopic time-resolved single crystal X-ray diffraction methods with ~10 ms resolution to study the ferroelastic domain dynamics in perovskite-based $LaAlO_3$ single crystal as a function of an alternating mechanical stress (0.01–50 Hz). Navirian et al. [49] applied the time-resolved X-ray diffraction method with a microsecond resolution to observe electric field-induced strain waves during the ferroelastic domain switching of KH_2PO_4 single crystal. Moriyoshi et al. [50] implemented a pump-probe high-energy single crystal X-ray diffraction method with 4 μs resolution to investigate the lattice response in a tetragonal $BaTiO_3$ bulk single crystal under a dynamical step-like electric field. They showed a time-dependent tetragonality during the field-induced piezoelectric vibration. Wooldridge et al. [51] and Vecchini et al. [52] developed a new measurement system which can simultaneously record the time-resolved X-ray diffraction profiles and the electrical polarization loops under an alternating electric field. It was applied to study electric field-induced phase transitions in a $Pb(Mg_{1/3}Nb_{2/3})O_3$-$xPbTiO_3$ bulk single crystal using 0.01–1 Hz AC electric fields, with ~25 ms resolution.

To summarize, the three different material systems categorized show the current state of stroboscopic time-resolved diffraction methods as follows:

(1) Up till now, ferroelectric *thin films* have only been investigated at synchrotron facilities. The main reason is that modern synchrotron facilities can provide a brilliant and intense X-ray source and allow for probing of time resolution down to the pico- and the nano-second using their bunch structures and overcoming the main disadvantages of a home-laboratory diffractometer system.

(2) Ferroelectric *bulk ceramics* have been investigated using stroboscopic time-resolved powder diffraction methods with microsecond time resolution. None of these have been used with nanosecond resolution to date.

(3) Studies on ferroelectric *bulk single crystals* are not abundant with respect to the time-resolved diffraction methods, furthermore the time resolution is limited to millisecond.

Based on the discussion in this section, many research studies have tried to improve the stroboscopic time-resolved diffraction techniques. Revolutionarily work is being performed in different ways with respect to the boundaries of the response time scale in different material systems. Those boundaries will finally converge on the nanosecond time regime.

1.4. The present work

This thesis explores new possibilities regarding the applications of a multi-channel analyzer data-acquisition system. The novel stroboscopic data-acquisition systems have been developed for this study, which provides time resolution down to nanosecond. In doing so, the systems have been successfully applied for several stroboscopic time-resolved X-ray diffraction experiments with various ferroelectrics.

This thesis is organized as follows:

Chapter 2 introduces the fundamental physics of ferroelectric materials.

Chapter 3 describes the basic physical principles of X-ray diffraction, which are single crystal X-ray diffraction and powder diffraction.

Chapter 4 presents the developments of the novel data-acquisition systems and the applications in stroboscopic time-resolved X-ray diffraction methods. Section 4.1 introduces the operating principles of the developed data-acquisition system. Section 4.2 provides examples of the applications which have developed new strategies for stroboscopic time-resolved X-ray diffraction experiments, and explains how the system performs (more details are described in Appendix A).

Chapter 5 discusses the investigation of the monoclinic distortion and polarization rotation in a $Na_{0.5}Bi_{0.5}TiO_3$ (NBT) single crystal under an alternating electric field using synchrotron-based time-resolved high-resolution reciprocal space mapping. This chapter emphasizes the importance of the relationship between the piezoelectricity and the polarization rotation in the monoclinic distortion.

Chapter 6 studies the origin of the enhanced piezoelectric activity in uniaxial ferroelectrics. The $Sr_{0.5}Ba_{0.5}Nb_2O_6$ (SBN50) single crystal is selected for the uniaxial ferroelectrics, and the piezoelectric response in the form of correlation between lattice parameter and domain size is measured using stroboscopic time-resolved X-ray diffraction rocking curve scanning. This chapter discusses that the observed high piezoelectricity in uniaxial ferroelectrics can be explained by a new mechanism, which may be affected by the nucleation of small ferroelectric domains under an applied electric field.

Chapter 7 describes the stroboscopic time-resolved X-ray powder diffraction study of $BaTiO_3$-based polycrystalline ferroelectric ceramics under an alternating electric field. This chapter discusses the mechanism of the electric field-induced polarization reversal and strain in perovskite-based ferroelectrics by utilizing small intensity differences between Friedel pairs.

Chapter 8 is the summary of the thesis.

1.5. List of publications in association with this work

Most of the results presented in this thesis have been published in separated articles and presented in the conferences. The following publications and conferences list are in related to this thesis.

(1) List of contributed publications:

Choe, H., Heidbrink, S., Ziolkowski, M., Pietsch, U., Dyadkin, V., Gorfman, S., and Chernyshov, D. *A microcontroller for in situ single-crystal diffraction measurements with a PILATUS-2M detector under an alternating electric field*. Journal of Applied Crystallography, **50**, 975–977 (2017). – (Chapter 4)

Choe, H., Gorfman, S., Heidbrink, S., Pietsch, U., Vogt, M., Winter, J., and Ziolkowski, M. *Multichannel FPGA-Based Data-Acquisition-System for Time-Resolved Synchrotron Radiation Experiments*. IEEE Transactions on Nuclear Science, **64**(6), 1320–1326 (2017). – (Chapter 4)

Choe, H., Gorfman, S., Hinterstein, M., Ziolkowski, M., Knapp, M., Heidbrink, S., Vogt, M., Bednarcik, J., Berghäuser, A., Ehrenberg, H., and Pietsch, U. *Combining high time and angular resolutions: time-resolved X-ray powder diffraction using a multi-channel*

analyser detector. Journal of Applied Crystallography, **48**, 970–974 (2015). – (Chapter 4)

Gorfman, S., Choe, H., Shvartsman, V. V., Ziolkowski, M., Vogt, M., Strempfer, J., Łukasiewicz, T., Pietsch, U., and Dec, J. *Time-Resolved X-Ray Diffraction Reveals the Hidden Mechanism of High Piezoelectric Activity in a Uniaxial Ferroelectric*. Physical Review Letters, **114**, 097601 (2015). – (Chapter 6)

Gorfman, S., Simons, H., Iamsasri, T., Prasertpalichat, S., Cann, D. P., Choe, H., Pietsch, U., Watier, Y., and Jones, J. L. *Simultaneous resonant x-ray diffraction measurement of polarization inversion and lattice strain in polycrystalline ferroelectrics*. Scientific Reports, **6**, 20829 (2016). – (Chapter 7)

(2) List of attended conferences:

Choe, H., Bieker, J., Pietsch, U., Ruett, U., Thomas, P. A., and Gorfman, S. *Time-resolved reciprocal space mapping of $Na_{0.5}Bi_{0.5}TiO_3$ single crystal under an alternating electric field*. 25th Annual Meeting of the German Crystallographic Society (DGK) 2017, Karlsruhe, Germany, March 27–30, 2017

Choe, H., Bieker, J., Pietsch, U., Ruett, U., Thomas, P. A., and Gorfman, S. *Time-resolved reciprocal space mapping of $Na_{0.5}Bi_{0.5}TiO_3$ single crystal under an alternating electric field*. 2016 Joint IEEE ISAF/ECAPD/PFM Conference, Darmstadt, Germany, August 21–25, 2016. – (Chapter 5)

Choe, H., Pietsch, U., Dec, J., Ruett, U., and Gorfman, S. *Time-resolved reciprocal space mapping probes the piezoelectricity in uniaxial $Sr_{0.5}Ba_{0.5}Nb_2O_6$ ferroelectrics*. 24th Annual Meeting of the German Crystallographic Society (DGK) 2016, Stuttgart, Germany, March 14–17, 2016

Choe, H., Gorfman, S., Shvartsman, V. V., Pietsch, U., and Dec, J. *Time-resolved X-ray diffraction on uniaxial $Sr_xBa_{1-x}Nb_2O_6$ ferroelectric single crystals under electric field*. 13th European Meeting on Ferroelectricity (EMF 2015), Porto, Portugal, June 28 – July 3, 2015 – (Chapter 6)

Gorfman, S., Choe, H., Dec, J., Ziokowski, M., Pietsch, U., and Łukasiewicz, T. *Time-resolved X-ray diffraction study of $Sr_{0.5}Ba_{0.5}Nb_2O_6$ under external electric field*. 22nd Annual Meeting of the German Crystallographic Society (DGK) 2014, Berlin, Germany, March 17–20, 2014

Chapter 2

Ferroelectric materials

This chapter describes the fundamentals of ferroelectric materials. General remarks of the most important physical concepts are introduced in order to understand ferroelectric materials and their microstructural features. The description of following sections is based on the textbook by Griffiths [53], Heywang, Lubitz & Wersing [54], Jona & Shirane [55], Newnham [56], Nye [57], and Rabe, Ahn & Triscone [58], and from review papers by Devonshire [59] and Gorfman [25].

2.1. General remarks on ferroelectrics

2.1.1. Dielectric polarization and dielectric permittivity

The polarization is a key concept of ferroelectricity. A simplified scheme of electric polarization is presented in Figure 2.1(a), showing a single atom consisting of an electron cloud surrounding a positively charge nucleus.

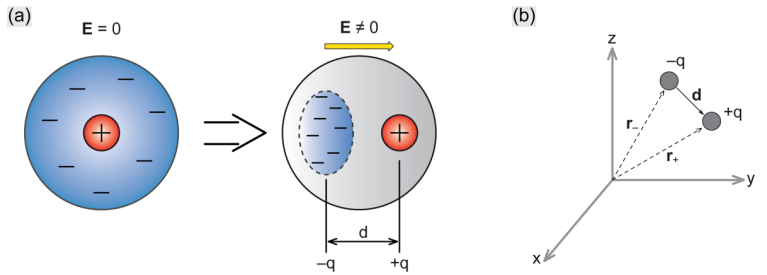

Figure 2.1 A schematic illustration (modified from Griffiths [53], pp.149–151) of an electric dipole moment: (a, b) A dielectric supports charge by acquiring a polarization in an external electric field on a microscopic scale – two opposite charges, $-q(\boldsymbol{r})$ and $+q(\boldsymbol{r})$, are separated by a distance $\boldsymbol{d}$.

In the presence of an external electric field, the electron cloud is pulled towards the positive pole of the field. The center of the positive (q^+) and negative (q^-) charges is separated by a certain distance $\boldsymbol{d}$ and thus an electric dipole moment $\boldsymbol{p}$, pointing opposite to the electric field, is induced and defined by,

$$\boldsymbol{p} = q \cdot \boldsymbol{r}_+ - q \cdot \boldsymbol{r}_- = q \cdot (\boldsymbol{r}_+ - \boldsymbol{r}_-) = q \cdot \boldsymbol{d} \tag{2-1}$$

where $\boldsymbol{d}$ is the distance between the negative and positive charge, and $\boldsymbol{r}_+$, $\boldsymbol{r}_-$ are the distance of positive and negative charges from the origin, respectively (see Figure 2.1(b)).

The total polarization $\boldsymbol{P}$ of a bulk material is defined as the sum of all microscopic polarizations $\boldsymbol{p}$ (of the atoms/molecules) normalized by the volume V:

$$\boldsymbol{P} = \frac{\sum \boldsymbol{p}}{V} \tag{2-2}$$

The physical dimension of the electric polarization is *C/m²*. In other words, the polarization $\boldsymbol{P} = 0$ does not mean that a material does not contain dipole moments, but only that the vector sum of all dipole moments is zero. In this case, the dipole moments are randomly oriented in the material.

A *polarization* P_i (*C/m²*) of a dielectric material is related to the applied electric field E_j (*V/m*) as follows:

$$P_i = \chi_{ij}\, \kappa_0\, E_j \tag{2-3}$$

where χ_{ij} (*F/m*) is the dielectric susceptibility tensor of a material and κ_0 is the dielectric permittivity of a vacuum (κ_0 = 8.854187817×10^{-12} *F/m*). Equation (2-3) is valid only for linear materials or in the linear range of nonlinear materials. In dielectrics, the presence of an external electric field E_i causes a dielectric displacement field D_i (*C/m²*), which is the sum of the electric displacement field of vacuum and the induced polarization P_i:

$$D_i = \kappa_0\, E_i + P_i \tag{2-4}$$

Combining Equations (2-3) and (2-4) gives

$$D_i = \left(\delta_{ij} + \chi_{ij}\right) \kappa_0 E_j = \kappa_{ij} E_j \quad (2\text{-}5)$$

where δ_{ij} is the Kronecker delta and κ_{ij} is the *dielectric permittivity* of a material.

2.1.2. Piezoelectricity

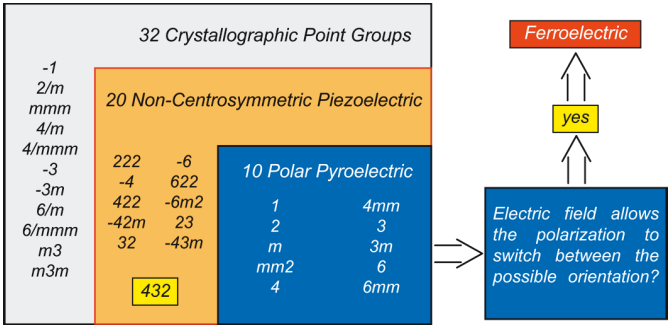

Figure 2.2 The relationship between crystallographic point groups and piezoelectric, pyroelectric, ferroelectric properties. There is no crystallographic distinction between a pyroelectric-ferroelectric material and a pyroelectric non-ferroelectric material. The '432' point group is not piezoelectric, even though it is non-centrosymmetric.

Piezoelectricity is an important physical property of many functional materials, which was firstly discovered in an α-quartz crystal by Jacques and Pierre Curie [60]. For understanding the piezoelectric activity of materials, it is crucial to consider general rules of crystal symmetry. Figure 2.2 shows an overview of all point groups – *a set of symmetry operators describing the point symmetry of a three-dimensional crystalline object* (De Graef & McHenry [61], p. 193) – and their properties. The point symmetry of three-dimensionally periodic solids can be described by one of the 32 point groups. Based on their symmetries, 21 of them are non-centrosymmetric and 11 groups are centrosymmetric. The piezoelectric effects exist only in non-centrosymmetric crystals,

but the point group '432' can also be excluded because all the piezoelectric coefficients vanish. Thus, a piezoelectric activity occurs in 20 out of the 21 non-centrosymmetric groups. Among them, 10 groups are pyroelectric, which has a property that the crystal is polar and the polarity is temperature dependent. If the polarization direction can be inverted by an external electric field then the crystal is also called ferroelectric. The explicit definition of ferroelectricity is given in the next sections.

The piezoelectricity can be mathematically described by two basic equations (Nye, [57]): one is for the *direct piezoelectric effect* and another is for the *converse piezoelectric effect* (see Figure 2.3). The direct piezoelectric effect is the development of electric polarization in response to applied mechanical stress:

$$P_i = d_{ijk}\,\sigma_{jk} \tag{2-6}$$

where P_i is the polarization vector, d_{ijk} is the third-rank tensor of the piezoelectric coefficient, and σ_{jk} is the mechanical stress tensor (Nye [57], p. 111; Newnham [56], p. 87). σ_{jk} indicates the mechanical force in the direction j transmitted through the surface, which is normal to the direction k.

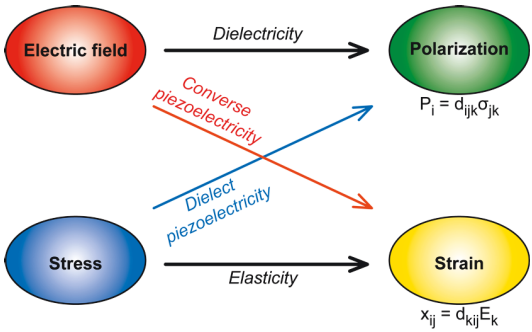

Figure 2.3 Relationship between the electrical and mechanical properties of a material (electromechanical couplings), showing the names of the properties and the variables (modified from Nye [57]).

The converse piezoelectric effect is the mechanical deformation in response to an external electric field:

$$x_{ij} = d_{kij} E_k \tag{2-7}$$

where x_{ij} is the strain tensor and E_k is the applied electric field. The reason of the equality between the direct and converse piezoelectric coefficients is based on thermodynamic arguments (Newnham [56], pp. 38, 88; Nye [57], pp. 115, 181).

Piezoelectric materials hence convert electrical energy into mechanical energy, and vice versa. The microscopic origin of the direct piezoelectric effect is the atomic displacement due to lattice deformations. Accordingly, a separation of charges produces polarization in a material. On the contrary, the converse piezoelectric effect is the other way around: an applied electric field causes the displacement of atoms in the unit cell and then the macroscopic deformation of the material can be observed.

2.1.3. Ferroelectricity

The physical properties of ferroelectric materials are used in many technologically important devices and hence it is essential to understand the fundamental principles of ferroelectricity to develop new materials.

Ferroelectricity is a phenomenon which was for the first time discovered in Rochelle salts by Valasek [1]. In general ferroelectrics have the following properties:

- A ferroelectric crystal has a spontaneous polarization (P_S), upon cooling below a phase transition temperature (Curie temperature, T_C).
- Ferroelectrics undergo a thermally driven phase transition from paraelectric to ferroelectric phases through the Curie temperature. The phase transition can be accompanied by small displacement of some atoms (ions) from their originally centrosymmetric positions.

- The direction of the polarization in ferroelectrics can be reversed by the application of an external electric field, i.e. spontaneous polarization can switch into the opposite direction. Furthermore, the remnant polarization can be easily re-oriented along the crystallographic axis under external perturbations. The

non-volatile random-access memory devices use the possibility of polarization switching property in order to read and write data.

- The dipole moments of a ferroelectric are not oriented towards the same direction, because it would be energetically unfavorable due to depolarization fields in the material. These are called 'domains', and have different orientation relative to each other. The domains are separated by 'domain walls' with a typical width of a few unit cells, in which the polarization is successively changed from one into the other orientation. Therefore, domain walls possess internal strains and increase the overall energy of the material, which is the reason why the density of domain walls is in an energetic balance with the number of domains. Domain wall motion under external influences can be crucial for defining properties of ferroelectrics.

- Ferroelectrics can have an efficient electromechanical coupling for many applications because they are accompanied with an enhanced piezoelectric activity.

2.1.4. Electrostriction

As discussed in Section 2.1.2, the piezoelectric effect exists only in non-centrosymmetric materials. However, in the presence of an external electric field, centrosymmetric materials also show strain but it is proportional to the square of the field strength. This second order phenomenon is called an '*electrostriction*'.

The electrostriction (see Figure 2.4) must be introduced by quadratic terms and the effect can be written by,

$$x_{ij} = Q_{klij} P_k P_l \tag{2-8}$$

where x_{ij} is the strain tensor, Q_{ijkl} is the electrostrictive tensor and P_k, P_l are the polarization.

From Equation (2-8) the polarization, P_k and P_l are consisted by,

$$P_k = P_k^0 + \epsilon_0 \epsilon_{kl} E_l \quad , \quad P_k = P_l^0 + \epsilon_0 \epsilon_{lk} E_k \tag{2-9}$$

where P_k^0, P_l^0 are the spontaneous polarizations, and both $\epsilon_0\epsilon_{kl}E_l$ and $\epsilon_0\epsilon_{lk}E_k$ are the field-induced components.

Substituting Equation (2-9) to (2-8), the electrostriction is extended as follows,

$$x_{ij} = Q_{klij}\left(P_k^0 \cdot P_l^0 + \epsilon_0\epsilon_{lk}P_k^0E_k + \epsilon_0\epsilon_{kl}P_l^0E_l + (\epsilon_0)^2\epsilon_{kl}\epsilon_{lk}E_lE_k\right) \quad (2\text{-}10)$$

On the right-hand side of Equation (2-10), the term $Q_{klij}\left(\epsilon_0\epsilon_{lk}P_k^0E_k + \epsilon_0\epsilon_{kl}P_l^0E_l\right)$ is shown the linearity with the applied electric field, which can be considered as the piezoelectric effects. The effective piezoelectric coefficient (i.e. the applied electric field is along E_k) can be accordingly given by,

$$d_{kij} = 2Q_{klij}\epsilon_0\epsilon_{lk}P_k^0 \quad (2\text{-}11)$$

From Equation (2-11), it can be concluded that the electrostriction can mimic piezoelectric effects in ferroelectrics [62].

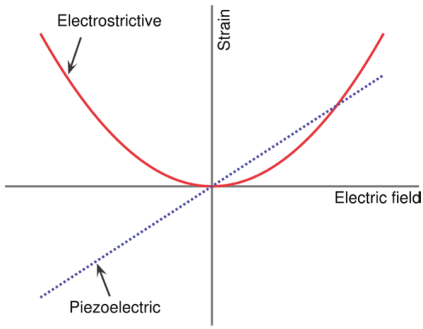

Figure 2.4 A schematic plot of the comparison between the electrostriction (red curve) and the piezoelectric activity (blue dot line) as a function of electric field. The electrostriction follows Equation (2-10) and the piezoelectric response follows Equation (2-7).

2.2. Polarization switching and hysteresis loop in ferroelectrics

The following description is based on the textbooks by Lines & Glass [63] and Xu [64], and from a review paper by Jin et al. [65].

One of the most important properties of a ferroelectric is the ability of polarization switching under a strong electric field (exceeding the so-called 'coercive field'). The polarization switching is characterized by measuring the hysteretic polarization versus electric field relationship (P–E loop) below the Curie temperature (T_C).

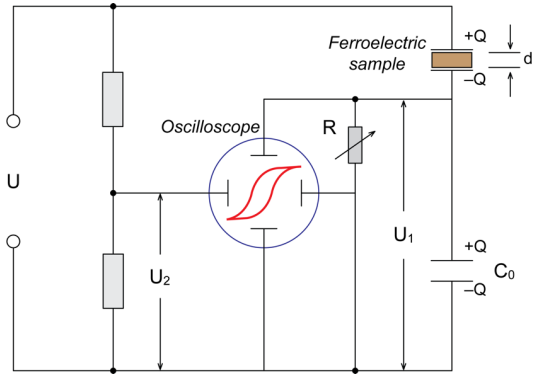

Figure 2.5 Schematic circuit of Sawyer–Tower bridge for observing Polarization–Electric field loop characterization of ferroelectrics (Variables are explained in the text). Modified from Jin et al. [65].

A popular method for observing the hysteresis loop is the Sawyer-Tower circuit, which was firstly developed by Sawyer and Tower [66]. The advantage of this circuit is an ability to characterize the real ferroelectric properties by measuring hysteresis loops. The measurement (see Figure 2.5) is performed as follows:

(1) An AC bipolar electric field is applied across the ferroelectric capacitor, here the voltage U across the ferroelectric capacitor can plot as a voltage monitor U_2 on the horizontal axis of an oscilloscope.

(2) A linear capacitor (with large capacitance, C_0) is connected in series with the ferroelectric sample, hence the voltage U_1 across the linear capacitor is proportional to the polarization P_i of the ferroelectrics. As introduced in Section 2.1.1, the dielectric displacement D_i and the polarization P_i are connected by Equation (2-4). Comparing to the large polarization P_i, the contribution by $\kappa_0 E_i$ can be ignored. Therefore, the experimentally obtained D_i is considered as P_i. However, the original form of the Sawyer-Tower circuit is no longer used, due to replacement by state-of-the-art electronic devices. In the newly developed commercial equipment, P_i is collected through charge or electrical current integration technique following with compensation by a variable resistor R.

The polarization–electric field hysteresis (P–E loop) and the strain–electric field hysteresis (x–E curve) in ferroelectrics are shown in Figure 2.6.

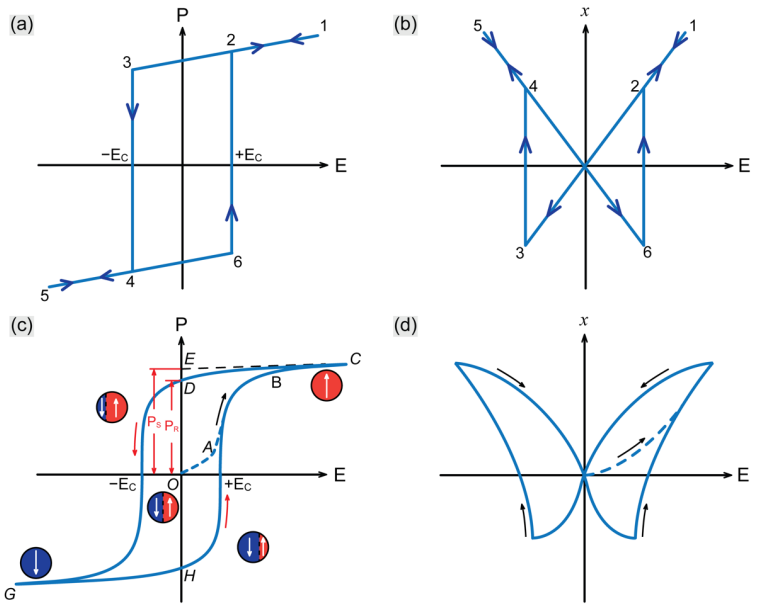

Figure 2.6 Switching and hysteresis of a ferroelectric (modified from Jona & Shirane [55]): (a) Polarization–Electric field (P–E), and (b) Strain–Electric field (x–E) hysteresis loops in an ideal ferroelectric single crystal. (c, d) Real material cases.

In ideal ferroelectrics, the polarization hysteresis loop has a rectangular (skew) shape, as shown in Figure 2.6(a). As the electric field strength reaches the coercive field ($+E_C/-E_C$), the polarization becomes zero, moreover, the polarization starts to switch into the opposite direction, immediately. These are marked as arrows between points **3** – **4** and **6** – **2** in Figure 2.6(a). The ferroelectric becomes a single domain at the strong electric fields, which significantly exceed the coercive fields: i.e. the direction of the polarization in all domains is aligned along the same field direction. Thus, an ideal hysteresis loop has a symmetrical shape: i.e. the positive/negative coercive fields and positive/negative remnant polarizations are equal. The polarization switching under an external electric field leads to strain–electric field hysteresis curves in ferroelectrics (see Figure 2.6(b)). This strain–electric field hysteresis is due to three types of ferroelectric effects: one is the normal converse piezoelectric effect of the lattice, and the other two are due to domain switching and domain wall motion. The straight parts **1** – **3** and **5** – **6** in Figure 2.6(b) represent the linear piezoelectric component of the strain. The slopes of these lines determine the piezoelectric coefficients. At points, **3** and **6**, the coercive field is reached, thus the spontaneous polarization is reversed and the piezoelectric effect changes its sign.

The loops for the real materials are shown in Figure 2.6(c) and (d). In the virgin state at the point **O**, the material possesses no macroscopic polarization and domain walls are formed to minimize the free energy of the material. A linear P–E loop is generated under a weak electric field, the so-called *sub-coercive field*, because the field is not strong enough to switch any domains: i.e. the material will respond similar to the normal dielectrics described in Equation (2-3). This response corresponds to the segment **OA** of P–E loop in Figure 2.6(c). When the electric field strength is high enough, the polarization within the domains will start to switch towards the field direction (**AB**). If the polarization vector of all domains is aligned along the applied field direction, it will reach a saturation state (**BC**). At this saturation sate, the material will be composed of a single domain. Decreasing the electric field strength, the value of the polarization will decrease (**BD**) but does not go back to zero. During this procedure, some of domains will remain aligned along the field direction, thus the material will exhibit a remnant polarization (P_R). In principle, a spontaneous polarization (P_S) is equal to the saturation state of the electric displacement extrapolated to the zero field (**CBE**). However, the remnant polarization may be different from the spontaneous polarization, because a domain wall motion can start before the electric filed reaches the coercive field in the real material.

2.3. Domain patterns in ferroelectrics

As introduced in Section 2.1.3, a domain in ferroelectrics is defined as a small region of a material where an electrical polarization (or a strain) is uniform and can be oriented along crystallographic directions in order to minimize free energy. A system of ferroelectric domains is usually a result of a structural phase transition that has a lower symmetry below a Curie temperature T_C. The *Landau-Devonshire model* is applied to describe ferroelectric phase transitions. The free energy of the ferroelectric system is expressed as,

$$\boldsymbol{G} = G_0 + \frac{\alpha}{2}\boldsymbol{P}^2 + \frac{\beta}{4}\boldsymbol{P}^4 + \frac{\gamma}{6}\boldsymbol{P}^6 + \cdots \quad (2\text{-}12)$$

where $\boldsymbol{G}$ is the free energy, $\boldsymbol{P}$ is the polarization, G_0 is the free energy for zero polarization and α, β, and γ are coefficients.

The coefficient α corresponds to a temperature parameter ($\alpha = \alpha'(T - T_0)$) where T_0 is the ferroelectric transition temperature (Curie-Weiss temperature). The energy well can have a different shape depending on their coefficients. There are two types of phase transitions, first and second order. The order of the transition depends on the sign of the coefficient β in Equation (2-12).

(1) First-order phase transitions

A *First-order phase transition* occurs when the parameter β is negative. The Curie temperature can be defined as the temperature at which $G = 0$ and $\frac{\partial G}{\partial P} = 0$ for $P \neq 0$. The T_C is higher than T_0 ($T_0 < T_C$) for the case of first-order phase transition. This indicates that even above the ferroelectric transition temperature, there are two stable polarization states and that the system will not become paraelectric where T_0 is reached until T_C. This shows over a range of temperature, from T_0 to above T_C (see Figure 2.7(a)).

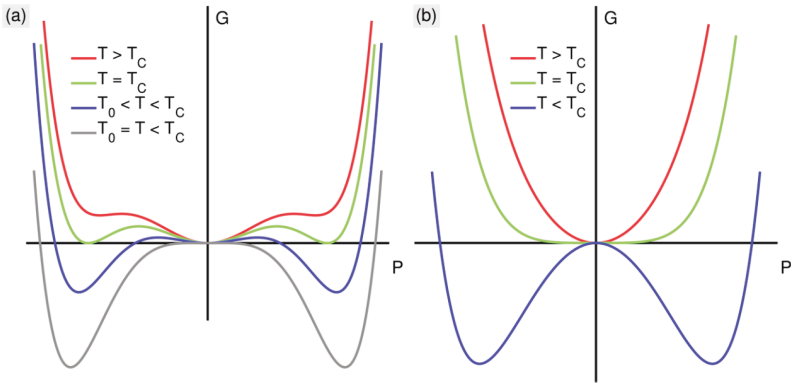

Figure 2.7 Free energy for (a) first-order and (b) second-order phase transitions. For the first-order phase transition, the polarization decreases until T_C, where it discontinuously drops to zero. For the second-order case, the system is ferroelectric below T_0, which is shown by the double well and a paraelectric phase above T_0 temperature.

(2) Second-order phase transitions

A *Second-order phase transition* occurs when the parameter β is positive. From Equation (2-12), the energy wells become both above ($\alpha > 0$) and below ($\alpha < 0$) the transition temperature. Above T_0, there is a single energy well. This means that the transition temperature (T_0) is equal to the Curie temperature (T_C), which is the temperature at which the paraelectric phase becomes more stable than the ferroelectric one. Figure 2.7(b) shows this second-order phase transition.

Considering the second-order phase transition theory and going through the phase transition, domains of opposite polarization are formed.

An applied external electric field can induce a switching phenomenon, which has different types of domains separated from its neighboring domains by domain walls. The types of domains in ferroelectrics can be categorized by *ferroelastic* (non-180°) and *inversion* (180°) domains. Figure 2.8 shows a schematic view of the possible domain patterns. It represents what happen when the material undergoes a phase transition, for example, (a) from cubic to rhombohedral symmetry and (b) from tetragonal to another tetragonal symmetry in uniaxial ferroelectrics, respectively. The

important thing is that the phase transition causes a strain in the crystal, i.e. the polarization direction is lying on the crystallographic directions to be a minimum of the free energy. The strained ferroelastic domains are shown in Figure 2.8(a). The domain walls connect the oriented domain components. The change of the volumetric fractions contributes to the overall macroscopic strain. The variation of the fractions due to an external electric field yields the 'extrinsic' electromechanical coupling. A single ferroelastic domain may also separate into a set of 180° ferroelectric domains (same colors in Figure 2.8(a)) which have same strain making them macroscopically undistinguishable (refer to Figure 2.8(b)) because of the identical crystallographic structure. Consequently, inversion domains ideally do not deform a crystal, while ferroelastic domains do. Therefore, the main difference between both types of domains is that 180° ferroelectric domains only affect the macroscopic polarization, but ferroelastic domains typically contain both parameters involving the electric polarization and the mechanical strain.

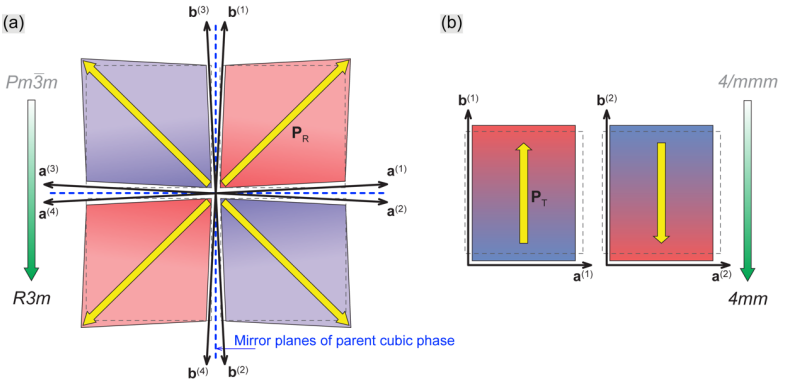

Figure 2.8 Illustration of the possible domain patterns. (a) A phase transition with ferroelastic domains (cubic to rhombohedral). (b) Case of 180° ferroelectric phase transition (tetragonal to tetragonal) in uniaxial ferroelectrics.

2.4. Electromechanical coupling in ferroelectrics

Ferroelectrics are widely used in many applications because of their enhanced electromechanical coupling. This section introduces the representative enhanced physical properties and their applications in ferroelectrics. The following description is based on a review paper by Damjanovic [67].

2.4.1. Intrinsic and extrinsic contributions to the piezoelectric properties in ferroelectrics

Piezoelectricity in ferroelectrics may be driven by intrinsic and extrinsic mechanisms. Intrinsic contributions originate from atomic displacements within the individual unit cells of a material under an external stress or an electric field, which subsequently cause the change of the crystal lattice parameters. This phenomenon is in general observed in non-polar piezoelectric materials such as α-quartz. However, a similar piezoelectric response occurs in ferroelectrics as well, where an additional contribution from extrinsic mechanism exists. This arises from the domain wall motion and the change of the volumes possessing different polarization or strain. Accordingly, the extrinsic effects can be controlled by domain engineering, while the intrinsic piezoelectric responses are dependent on the inter-atomic distances or chemical bonds.

2.4.2. Morphotropic phase boundary and enhanced piezoelectric effect

The term 'morphotropic phase boundary' has been frequently used to refer to the phase transition between the tetragonal and the rhombohedral ferroelectric phases as a result of varying the compositions [68]. Most studies on morphotropic phase boundaries have been performed on perovskite-based ferroelectrics or piezoelectrics, such as $Pb(Zr,Ti)O_3$ and $BaTiO_3$.

A typical temperature-composition phase diagram for $Pb(Zr,Ti)O_3$ is shown in Jaffe et al. [69]. Other studies [70–72] showed that a monoclinic phase exists between the tetragonal and rhombohedral phases in a narrow composition range of $Pb(Zr,Ti)O_3$ materials. They indicated that the monoclinic structure can be pictured as a 'bridge' between the tetragonal and rhombohedral phase structures.

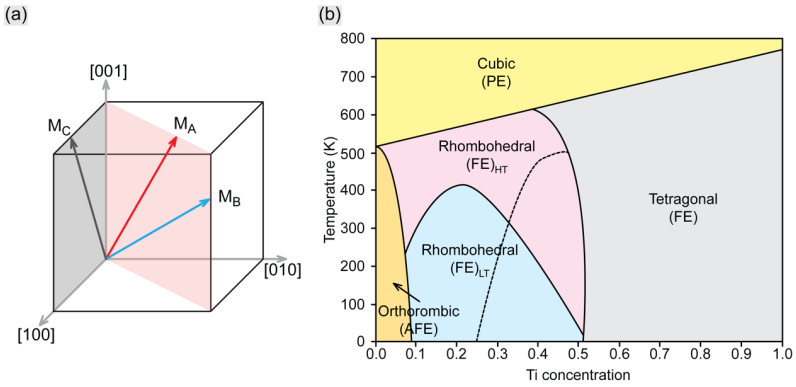

Figure 2.9 (a) A schematic illustration of the possible monoclinic phases, M_A, M_B and M_C. (b) Phase diagram for $Pb(Zr,Ti)O_3$: The dashed line shows the boundary between M_A and M_B phase structure (modified from Zhang et al. [73]).

Prior to the discovery of monoclinic phases, only rhombohedral, orthorhombic, and tetragonal phases were experimentally observed in perovskite ferroelectrics [63]. After that, the possible monoclinic phases, namely, M_A, M_B, and M_C, have been observed by various research studies [71,74–76]. Figure 2.9(a) shows the possible monoclinic phases. The polarization vector of M_A and M_B phases is lying on the (110) plane, while the polarization of M_C is on the (101) mirror plane. Recently, the nature of the monoclinic phase across the Zr-rich and morphotropic phase boundary region of $Pb(Zr,Ti)O_3$ phase diagram is described in detail by Zhang et al. [73] (see Figure 2.9(b)). Long-range average rhombohedral and both long- and short-range monoclinic regions coexist in all compositions. In addition, a boundary between a monoclinic M_A structure and another monoclinic M_B structure has been established.

For the simple-structured pure compound ferroelectrics such as $BaTiO_3$, Fu & Cohen [77] theoretically studied for the effect of an enhanced piezoelectricity. They suggested that it could be driven by polarization rotation induced by an external electric field [78]. Ahart et al. [68] experimentally confirmed the theoretical predictions of morphotropic phase boundary in $PbTiO_3$ single crystal under high pressure. This opened a possibility to discover materials with a strong electromechanical coupling and a simple structure.

2.4.3. Application of ferroelectrics

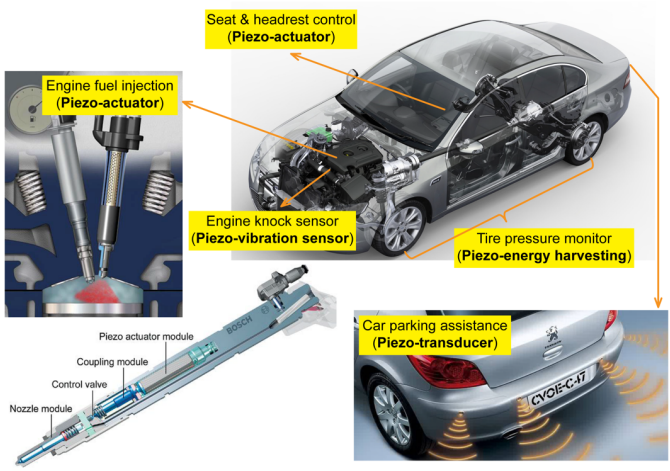

Figure 2.10 Representative applications of the piezoelectric properties (e.g. transducer, actuator, etc.) in an automobile-related industry. (Pictures from Ford Motor Company, Keko Equipment, Bosch Mobility Solution, and AutoOne Electrics, respectively.)

Because of their efficient electromechanical coupling, ferroelectrics are used in numerous applications (see Figure 2.10) ranging from everyday life products to a specific industry area with large scales:

- Transducers and sensors can be found in microphones, guitar pickups, or in sensors of electrical drum pads and also are numerously used in automotive or medical (ultrasound) applications [79,80].

- Actuating applications are of special importance for industry, e.g. in car fuel injection devices [81,82], or in positioning systems [83]. In these cases, ferroelectric multilayer actuators are mostly used, which show high strain and high force in both quasi-static and dynamic applications.

- Energy harvesters [84,85], which transform deformation into electrical energy, are developing for the future to alternative power sources [86].

- Even more exotic applications, such as ultrasonic micro-motors for industrial and medical products, could be developed by using ferroelectrics and appropriate processing techniques [87].

- Finally, ferroelectric thin films play a key role in piezoelectric microelectromechanical systems (Piezo-MEMS) because of the miniaturization of sensors and actuators [88].

2.5. Crystallography of ferroelectric perovskites

This section describes how the crystal structure changes upon the phase transitions between centrosymmetric and non-centrosymmetric crystals. Nowadays, the most interesting model systems in ferroelectrics is the 'perovksite structure'. The term 'perovskites' comes from the mineral perovskite calcium titanate ($CaTiO_3$).

The perfect perovskite structure is constructed with a general formula $\mathbf{ABO_3}$. It has the centrosymmetric structure at high temperatures i.e. above a Curie temperature, all unit cell edges are 90° to each other and have the same length: The **A** atom is in the position [0, 0, 0], and the **B** atom is in the position [1/2, 1/2, 1/2], and the oxygen atom is in the cubic phase. Below the Curie temperature, the crystal structure is distorted to a non-centrosymmetric, which displaces **B** atom (or **A**) out of the center of an oxygen octahedron.

The perovskite structure can also be explained in reference to atoms **A** and **B**. The **B** atom is surrounded by 6 oxygen atoms while the **A** atom is surrounded by 12. Figure 2.11(a) and (b) illustrate the neighborhood of **B** (**A**) atom, for example the perovskite $BaTiO_3$. It shows the bonding Ti-O and Ba-O, and an oxygen polyhedra with respect to the neighborhood atoms. Ti atom (**B** position) has 6 equidistance oxygen neighbors exhibiting a centrosymmetric structure when it is exactly in the center of the oxygen octahedra. However, when it is displaced outside the center of the octahedra then a polarization will occur. Similarly, the same can be said regarding the Ba atom (**A** position). If the bonds Ba-O is considered, then the Ba atom is surrounded by 12 oxygens, which is called oxygen cage. So, if this atom is in the center of the oxygen cage then the structure is centrosymmetric. Such configuration cannot have any polarization, however a displacement in any direction would result in an induced polarization in the crystal, and thus an induced strain. Examples of perovskite ferroelectrics are barium titanate ($BaTiO_3$), potassium niobate ($KNbO_3$), lead titanate

($PbTiO_3$), lead zirconate titanate ($Pb(Zr,Ti)O_3$), sodium bismuth titanate ($Na_{0.5}Bi_{0.5}TiO_3$), and so on.

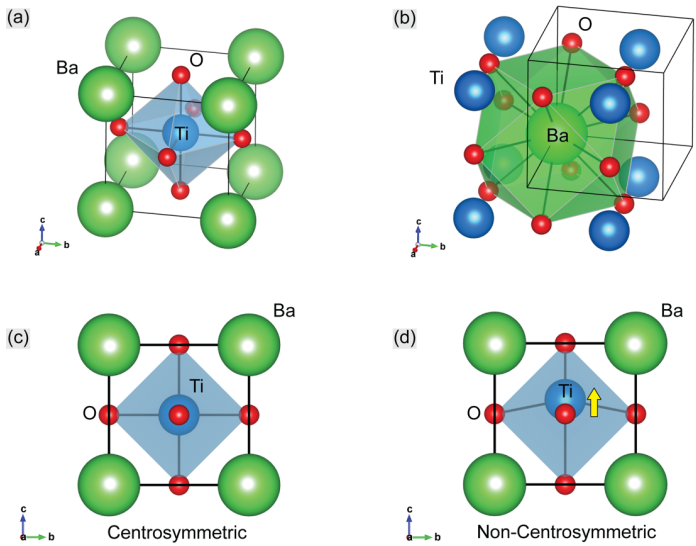

Figure 2.11 Illustrations for the perovskite structure of $BaTiO_3$: **A** atom is Barium (Ba), and **B** atom is Titanium (Ti), drawn using the VESTA package [89]. (a) The six oxygen neighbors are around Ti atom. (b) The case of 12 oxygen neighbors around Ba atom. (c) A centrosymmetric structure of the $BaTiO_3$. (d) A displacement of Ti atom creates a non-centrosymmetric structure.

Chapter 3

X-ray diffraction

X-ray diffraction is nowadays the main tool to characterize crystal structures. This chapter introduces the basic principles of X-ray diffraction, following the textbooks by Ashcroft [90], De Graef & McHenry [61], Giacovazzo [91], Hammond [92], Jackson [93], and Warren [94].

3.1. Basic physical principle of X-ray diffraction

X-rays are electromagnetic waves with a wavelength ranging between 0.1 ~ 100 Å. The simplest description of X-ray diffraction can be approached by the *kinematical theory*. This theory assumes that X-rays are scattered so weakly at electrons, so that any re-scattering processes can be neglected and hence the total scattering amplitude of a crystal can be approximated by simply summing the scattering waves from each electron.

3.1.1. Scattering by electrons

Figure 3.1 illustrates a physical principle of scattering of a monochromatic X-ray beam with the wavelength λ. The electric field of a plane wave, with a wave vector of a primary X-ray beam $\boldsymbol{k}_0$, a polarization vector $\boldsymbol{\epsilon}_0$, an amplitude E_0 and $\boldsymbol{r}_e$ is a position of the electron from the origin, can be described as,

$$\boldsymbol{E}_0 = \boldsymbol{\epsilon}_0 E_0 \, exp(2\pi i \boldsymbol{k}_0 \cdot \boldsymbol{r}_e) \tag{3-1}$$

Classically an electron is forced to oscillate when the electric field of the wave is applied. The electric field of the outgoing wave at the distance R of the observation point can be written by (Jackson [93], p. 694),

$$\boldsymbol{E} = \boldsymbol{\epsilon} E \, exp(2\pi i \boldsymbol{k}_1 \cdot \boldsymbol{r}_e) = -\boldsymbol{\epsilon} \frac{r_e E_0 p}{R} \, exp(2\pi i (\boldsymbol{k}_1 - \boldsymbol{k}_0) \cdot \boldsymbol{r}_e) \cdot exp(2\pi i \boldsymbol{k}_1 \cdot \boldsymbol{r}_e) \tag{3-2}$$

where $\boldsymbol{\epsilon}$ is the polarization vector, p is the polarization factor, $\boldsymbol{k}_1$ is the wave vector of the scattered X-ray beam and r_e is the classical electron radius.

Through it, the amplitude of X-ray scattering can be described as a function of a scattering vector, defined as $\boldsymbol{H} \equiv \boldsymbol{k}_1 - \boldsymbol{k}_0$ (see Figure 3.1(a)) and it is,

$$E = \frac{r_e E_0 p}{R} exp(2\pi i\, \boldsymbol{H} \cdot \boldsymbol{r}_e) \tag{3-3}$$

Within the approximation of elastic scattering, the length of the wave vectors of the primary and scattered X-ray beam is the same and equals to $|\boldsymbol{k}_0| = |\boldsymbol{k}_1| = 1/\lambda$. The waves scattered at different scattering centers interfere with each other and hence the sum of two waves depends on the phase difference between them.

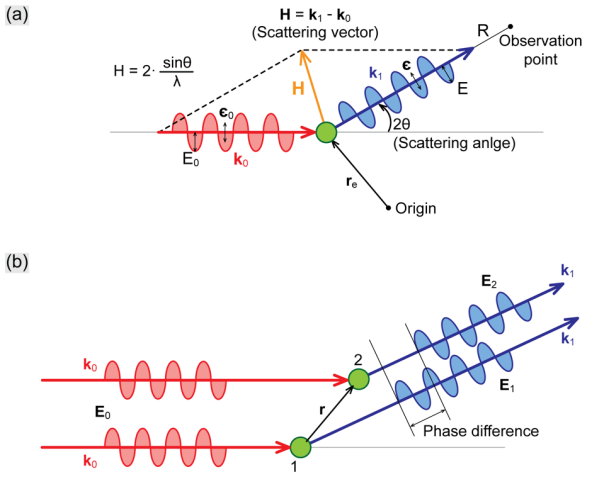

Figure 3.1 Sketch of X-ray scattering. (a) The geometric view of the scattering by an electron. Both the direction and polarization of X-ray photon have been changed by a scattering angle 2θ. (b) The X-ray electromagnetic waves ($\boldsymbol{E}_0$) with a same wave vector ($\boldsymbol{k}_0$) are scattered by two electrons, which are separated by the relative position $\boldsymbol{r}$. The scattered waves have the certain phase difference.

If there are two electrons (refer to Figure 3.1(b)), then an amplitude of the electric field $\boldsymbol{E}_1$ ($\boldsymbol{E}_2$) of the scattered wave from the single electron e_1 (e_2) can be defined by,

$$E_1 \propto E_0\, exp(2\pi i(\,\boldsymbol{k}_1 - \boldsymbol{k}_0)\cdot \boldsymbol{r}_1)\;\;,\quad E_2 \propto E_0\, exp(2\pi i(\,\boldsymbol{k}_1 - \boldsymbol{k}_0)\cdot \boldsymbol{r}_2) \tag{3-4}$$

where $\boldsymbol{r}_1$ ($\boldsymbol{r}_2$) is a position of the electron e_1 (e_2) from the origin. Thus, the amplitude of the electric field $\boldsymbol{E}_1$ is described as the $\boldsymbol{E}_2$,

$$E_2 = E_1 exp(2\pi i(\boldsymbol{k}_1 - \boldsymbol{k}_0)\cdot \boldsymbol{r}) \tag{3-5}$$

where $\boldsymbol{r}$ is the vector connecting two different electrons, and $2\pi i(\boldsymbol{k}_1 - \boldsymbol{k}_0)\cdot \boldsymbol{r}$ is the phase difference between waves '1' and '2'.

Consequently, a sum of those two electric fields of the scattered waves can be written by,

$$A(\boldsymbol{k}_1, \boldsymbol{k}_0) = E_1\{exp(2\pi i(\boldsymbol{k}_1 - \boldsymbol{k}_0)\cdot 0) + exp(2\pi i(\boldsymbol{k}_1 - \boldsymbol{k}_0)\cdot \boldsymbol{r})\} \tag{3-6}$$

3.1.2. Scattering by an atom

If the scattering from electrons within an atom will be considered, then the scattering amplitude is proportional to the integral summation over continuously distributed density of electrons,

$$A_{atom}(\boldsymbol{H}) = \int exp(2\pi i \boldsymbol{H}\cdot \boldsymbol{r}_a)\rho(\boldsymbol{r}_a)dV \tag{3-7}$$

where $\rho(\boldsymbol{r}_a)$ is the electron density which is the probability of finding an electron at any point, as described by their wave functions. Here, $\boldsymbol{r}_a$ is the electron-distribution around an atom, thus the $\rho(\boldsymbol{r}_a)dV$ is the amount of finding electrons in the small volume dV. From Equation (3-7), the *atomic scattering factor* is defined by,

$$f_a(\boldsymbol{H}) = \int exp(2\pi i \boldsymbol{H}\cdot \boldsymbol{r}_a)\rho_a(\boldsymbol{r}_a)dV \tag{3-8}$$

The atomic scattering factor is the amplitude of X-ray scattering by a single atom. This scattering factor depends only on the type of atom 'a' determining the electron density

distribution. A physical meaning of Equation (3-8) is that the total scattering $f_a(\boldsymbol{H})$ is found by summing over the total electrons in an atom, so that the scattering contributions from each elementary region ($\rho_a(\boldsymbol{r}_a)dV$) taking each phase difference ($exp(2\pi i\boldsymbol{H}\cdot\boldsymbol{r}_a)$) into account. The calculation of the scattering factor requires the knowledge of electron density from the wave function. However, there is no analytical form for the electron density of many-electron atoms, hence the atomic scattering factor can be approximated for each atom in a periodic table by methods of '*quantum chemistry*' [95,96]. It is a common practice to approximate the atomic scattering factor by the following empirical expression:

$$f_a\left(\frac{sin\theta}{\lambda}\right) = \sum_{i=1}^{4} a_i exp\left(-b_i \frac{sin^2\theta}{\lambda^2}\right) + c \qquad (3\text{-}9)$$

where the coefficients, a_i, b_i, and c, are tabulated for each atom of the periodic table in the '*International Tables for Crystallography: Volume C*' [97].

Figure 3.2 shows examples in which the atomic scattering factor is numerically estimated by Equation (3-9) for three atoms – Barium (Ba), Titanium (Ti), and Oxygen (O), respectively. For example, the f_a-curve of the oxygen atom (see Figure 3.2(c)) shows that it starts ('start' means $sin\theta/\lambda = 0$, which also means the scattering angle $2\theta = 0$) at 8 and decreases thereafter. This means that all 8 electrons of the oxygen atom are scattering in phase at zero scattering angle, but the scattering from all 8 electrons becomes out of phase when the $sin\theta/\lambda$ (also 2θ) value is increased.

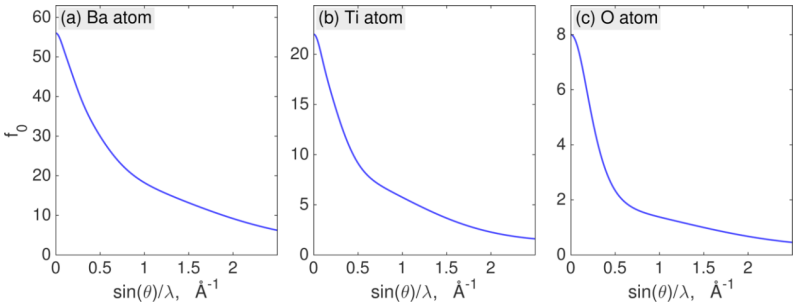

Figure 3.2 Atomic scattering factors of three different atoms – (a) Barium (Ba), (b) Titanium (Ti), and (c) Oxygen (O) – are numerically estimated by Equation (3-9).

3.1.3. Scattering by a crystal

The third step of the assembly is to add up the atoms inside one unit cell, hence the atomic scattering factors $f_a(\boldsymbol{H})$ of the different atoms are summed up, while taking the phase difference into account. If there are N atoms in the unit cell with the positions $\boldsymbol{R}_1$, $\boldsymbol{R}_2$, ... $\boldsymbol{R}_N$, then the scattering amplitude by a single unit cell is given by,

$$A_{unit\ cell}(\boldsymbol{H}) = \sum_{a=1} f_a(\boldsymbol{H}) exp\big(2\pi i \boldsymbol{H} \cdot (\boldsymbol{r}_{uc} + \boldsymbol{R}_a)\big)$$

$$= \sum_{a=1} exp(2\pi i \boldsymbol{H} \cdot \boldsymbol{R}_a) f_a(\boldsymbol{H}) \cdot exp(2\pi i \boldsymbol{H} \cdot \boldsymbol{r}_{uc}) \tag{3-10}$$

where $\boldsymbol{r}_{uc}$ is the position of the different unit cells in the crystal and $\boldsymbol{R}_a$ is the position of atom 'a' in the unit cell. Here, the *structure factor* $F(\boldsymbol{H})$ in a single unit cell is defined as follows,

$$F(\boldsymbol{H}) = \sum_{a=1} f_a(\boldsymbol{H}) exp(2\pi i \boldsymbol{H} \cdot \boldsymbol{R}_a) \tag{3-11}$$

where $\boldsymbol{R}_a = [x_a,\ \ y_a,\ \ z_a]$ is the atomic positions in the unit cell. The important thing is that the structure factor connects the crystal structure and the intensity of X-ray diffraction. Now, let us build an actual 3D periodic crystal, which can be described by the crystal *lattice* and the *unit cell*. Crystal lattice is a mathematical object, describing the periodicity of a crystal structure, hence the crystal lattice points can be represented with the basis vectors $\boldsymbol{a}_1$, $\boldsymbol{a}_2$, $\boldsymbol{a}_3$: $\boldsymbol{r}_{uc} = u\boldsymbol{a}_1 + v\boldsymbol{a}_2 + w\boldsymbol{a}_3$, where u, v, and w are integers. Accordingly, the sum of the scattering amplitude over the whole crystal can be written by,

$$A_{cryst}(\boldsymbol{H}) = \sum_a \underbrace{\left(\int exp(2\pi i \boldsymbol{H} \cdot \boldsymbol{r}_a)\rho(\boldsymbol{r}_a)dV\right)}_{atomic\ scattering\ factor\ f_a(\boldsymbol{H})} exp(2\pi i \boldsymbol{H} \cdot \boldsymbol{R}_a) \sum_{uvw} exp(2\pi i \boldsymbol{H} \cdot \boldsymbol{r}_{uc}) \tag{3-12}$$

$$= \underbrace{\sum_a f_a(\boldsymbol{H}) exp(2\pi i \boldsymbol{H} \cdot \boldsymbol{R}_a)}_{structure\ factor\ F(\boldsymbol{H})} \underbrace{\sum_u \sum_v \sum_w exp(2\pi i \boldsymbol{H} \cdot \boldsymbol{r}_{uc})}_{lattice\ sum} \tag{3-13}$$

The last term of lattice sum in Equation (3-13), $L(\boldsymbol{H}) \equiv \sum_u \sum_v \sum_w exp(2\pi i \boldsymbol{H} \cdot \boldsymbol{r}_{uc})$ depends on the geometry of the crystal lattice only. For the further analysis, it is convenient to express the scattering vector $\boldsymbol{H}$ with respect to the so-called '*reciprocal basis vectors*', $\boldsymbol{a}_1^*$, $\boldsymbol{a}_2^*$, and $\boldsymbol{a}_3^*$. They are defined by,

$$\boldsymbol{a}_i \cdot \boldsymbol{a}_j^* = \delta_{ij} \tag{3-14}$$

where δ_{ij} is the Kronecker delta (i.e. equal to 1 for $i = j$ and 0 for $i \neq j$). From the definition, the reciprocal basis vectors are described as follows,

$$\boldsymbol{a}_1^* = \frac{\boldsymbol{a}_2 \times \boldsymbol{a}_3}{V} \quad , \quad \boldsymbol{a}_2^* = \frac{\boldsymbol{a}_3 \times \boldsymbol{a}_1}{V} \quad , \quad \boldsymbol{a}_3^* = \frac{\boldsymbol{a}_1 \times \boldsymbol{a}_2}{V} \tag{3-15}$$

where V is the volume of the unit cell, $V = \boldsymbol{a}_1 \cdot (\boldsymbol{a}_2 \times \boldsymbol{a}_3)$.

Hence, the scattering vector is written by, $\boldsymbol{H} = h\boldsymbol{a}_1^* + k\boldsymbol{a}_2^* + l\boldsymbol{a}_3^*$, where h, k, and l are the coordinates of $\boldsymbol{H}$ relative to the dot product with each basis vector, $\boldsymbol{a}_1$, $\boldsymbol{a}_2$, $\boldsymbol{a}_3$, i.e. $h = \boldsymbol{H} \cdot \boldsymbol{a}_1$ (Warren [94], p. 31). According to Equation (3-14), the dot product between $\boldsymbol{H}$ and $\boldsymbol{r}_{uc}$ is:

$$\boldsymbol{H} \cdot \boldsymbol{r}_{uc} = hu + kv + lw \tag{3-16}$$

If the crystal consists of the N_a, N_b, and N_c unit cells along the three crystallographic axes $\boldsymbol{a}_1$, $\boldsymbol{a}_2$, and $\boldsymbol{a}_3$ respectively, then the summation in the $L(\boldsymbol{H})$ function is carried out by,

$$L(\boldsymbol{H}) = \sum_{u=0}^{a-1} exp(2\pi i h u) \sum_{v=0}^{b-1} exp(2\pi i k v) \sum_{w=0}^{c-1} exp(2\pi i l w) \tag{3-17}$$

According to the formula – '*the sum of n terms of the geometric progression*', Equation (3-17) can be re-written as follows,

$$L(\boldsymbol{H}) = \frac{1 - exp(2\pi i h N_a)}{1 - exp(2\pi i h)} \cdot \frac{1 - exp(2\pi i k N_b)}{1 - exp(2\pi i k)} \cdot \frac{1 - exp(2\pi i l N_c)}{1 - exp(2\pi i l)} \tag{3-18}$$

The intensity of X-ray scattering is the square of the absolute value of the amplitude, $I(\boldsymbol{H}) \sim |A(\boldsymbol{H})|^2$ and hence

$$|L(\boldsymbol{H})|^2 = \frac{sin^2(\pi N_a h)}{sin^2(\pi h)} \cdot \frac{sin^2(\pi N_b k)}{sin^2(\pi k)} \cdot \frac{sin^2(\pi N_c l)}{sin^2(\pi l)} \quad (3\text{-}19)$$

This expression is known as '*Laue interference function*'. Figure 3.3 shows the examples of the h-dependence of the Laue function (Equation (3-19)) for the different unit cell numbers. For example, there are two different material systems; one is 10 nm thin film and another is 1 μm bulk single crystal, but both of them have a same size of a unit cell 10 Å. Therefore, the number of unit cells is 10 and 1000, respectively. The peaks of the bulk single crystal are accordingly much higher and shaper than those of the thin film.

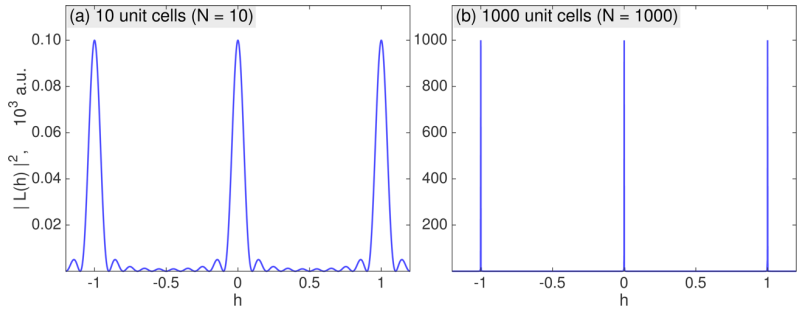

Figure 3.3 Laue function (Equation (3-19)) corresponding to the different numbers of unit cell; (a) N=10 and (b) N=1000 respectively. When the number of unit cell is increasing, the peaks become higher and sharper.

If the number of unit cells is sufficiently large in the crystal, i.e. (N_a, N_b, and N_c) → ∞, the intensity of X-ray scattering by a crystal is non-zero for the scattering vector $\boldsymbol{H}$ whose h, k, and l have integers. Therefore, strong diffraction intensities can be expected when $\boldsymbol{H}$ is equal to one of the corresponding reciprocal lattice vectors:

$$\boldsymbol{H} = h\boldsymbol{a}_1^* + k\boldsymbol{a}_2^* + l\boldsymbol{a}_3^* \quad (3\text{-}20)$$

where h, k, and l are integers. This is the so-called '*Laue equation*'.

3.2. Ewald sphere

Which part of reciprocal space is accessible on the X-ray diffraction pattern obtained from a still crystal? The answer is given by Ewald sphere construction with a monochromatic X-ray beam introducing in this section. The constructed Ewald sphere and the detectable reciprocal lattice point are sketched in Figure 3.4 and the recipe is explaining as follows:

- Draw the base line of the primary X-ray beam, and the incident wave vector $\boldsymbol{k}_0$. This vector is lying on the incident beam base line with length $1/\lambda$.

- Draw a sphere centered on the path of the incident beam ($\boldsymbol{k}_0$) with radius $1/\lambda$. The primary incident X-ray beam and the diffracted beam have the same wavelength, i.e. $|\boldsymbol{k}_0| = |\boldsymbol{k}_1| = 1/\lambda$. The diffracted wave vector $\boldsymbol{k}_1$ lies on the direction from a crystal to the detector. $\boldsymbol{k}_1$ can be translated into the center of the sphere. The scattering vector $\boldsymbol{H}$ $(= \boldsymbol{k}_1 - \boldsymbol{k}_0)$ completes the triangle from the tip of $\boldsymbol{k}_0$ to that of $\boldsymbol{k}_1$. Therefore, $\boldsymbol{H}$ from the crystal always points on the sphere surface.

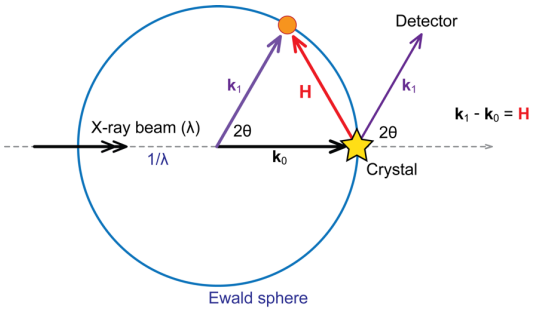

Figure 3.4 An illustration of Ewald sphere construction. The center of the Ewald sphere lies along an incoming primary X-ray beam with the radius $1/\lambda$. The origin of the reciprocal lattice is placed in the path of the incoming X-ray beam at the circumference of the Ewald sphere. When the crystal is rotated, the reciprocal lattice vector rotates, and when a reciprocal lattice point is on the surface of the Ewald sphere, the associated Bragg peaks are recording on the detector.

3.3. Single crystal X-ray diffraction

To observe the diffraction patterns from a single crystal, different types of experimental scan modes can be performed. This section demonstrates the rocking curve scan and the reciprocal space mapping, which are used in this work.

3.3.1. Diffraction pattern from a rotated crystal: rocking curve scan

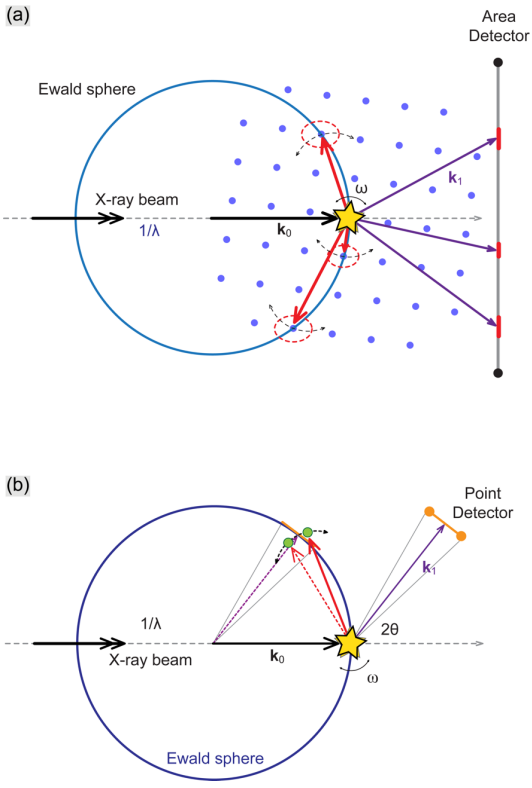

Figure 3.5 Illustrations of the ω-scan (rocking scan) mode. A crystal is rotated around one of a certain axis of the diffractometer, which is allowing the scattering vectors being able to intersect the Ewald sphere. (a) An area detector or (b) a single-photon counter is used to record the intensity map or/and profile of the diffracted signal.

In order to observe diffraction profile from a single Bragg peak, the Ewald sphere surface must intersect with the reciprocal lattice points as shown in Figure 3.5.

A rocking curve scan corresponds to rotating the crystal around one of certain diffractometer axes (refer to Figure 3.5). It allows a rotation of the scattering vectors being able to intersect the surface of the Ewald sphere during the scan. While the crossing scattering vectors through the Ewald sphere can be mapped on a two-dimensional area detector (Figure 3.5(a)), a one-dimensional diffraction profile as a function of the ω angle can be recorded using a single-photon counter (Figure 3.5(b)).

An example of the obtained rocking curve from a BiB_3O_6 single crystal using a single-photon counter [21,24] is shown in Figure 3.6. The rocking curve profile involves the following parameters: peak position (center of mass), integrated intensity, peak width (full width at half maximum), peak shape (asymmetry), and peak separation into components. The research results implementing this method will be discussed in more detail in Chapter 6 [98].

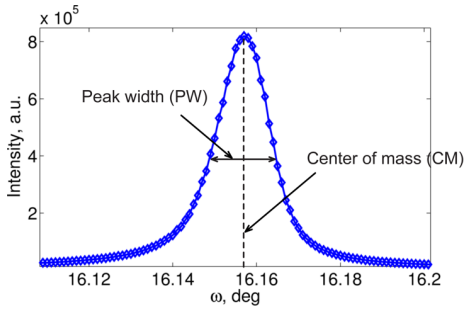

Figure 3.6 An example of rocking curve profile in the BiB_3O_6 single crystal [21,24]: the observed rocking curve can be determined as the integrated intensity (area of the peak), the peak positions (CM), and the peak widths (PW) for a simple single peak.

3.3.2. Reciprocal space mapping

Unlike one-dimensional rocking curve profile, a reciprocal space map is used to study complex, e.g. multi-domain structure of crystals where domains differ by their lattice parameters or just by the angles between the lattice planes and incident beam (ω). Thus, the reciprocal space mapping is useful method to determine the mesoscopic structural properties.

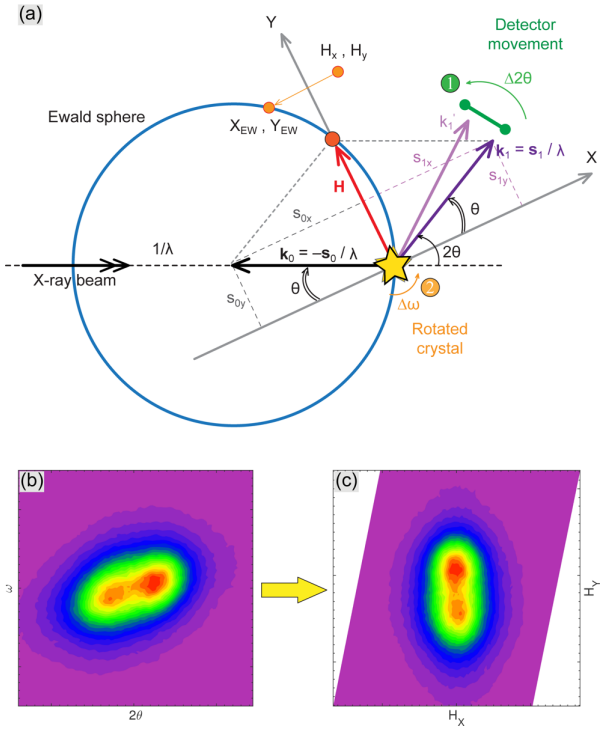

Figure 3.7 (a) Sketch of a conversion from angular coordinates into the Cartesian coordinates for the measured reciprocal space map (details are explained in the text). (b, c) Example of the transformation of the observed reciprocal space map from a $Na_{0.5}Bi_{0.5}TiO_3$ single crystal.

Reciprocal space maps can be measured using either a single-photon counter or a two-dimensional area detector for three-dimensional reciprocal space maps as well. This section represents measurements of two-dimensional reciprocal space maps using a single-photon counter and an analyzer crystal in order to provide a high angular resolution. A reciprocal space region can be mapped by collecting a series of ω rocking scans at various 2θ angles (defined by the position of the detector).

The obtained map can be converted from angular coordinates (ω, 2θ) into the Cartesian coordinates with the horizontal X-axis and the vertical Y-axis (H_X, H_Y) which are the Y-axis is along the scattering vector and the X-axis is perpendicular to it (see Figure 3.7(a)). This conversion is performed by defining the reciprocal space vector $\boldsymbol{H}$ (Equation (3-22)) with unit vectors $\boldsymbol{s}_0$ (from a crystal to a source) and $\boldsymbol{s}_1$ (from a crystal to a detector) for the incident and diffracted X-ray beam, respectively (Equation (3-21)).

$$\boldsymbol{s}_0 = \{-\cos\theta\ ,\ \ \sin\theta\}\ \ ,\ \ \boldsymbol{s}_1 = \{\cos\theta\ ,\ \ \sin\theta\} \tag{3-21}$$

Here, the unit vectors, $\boldsymbol{s}_0$ and $\boldsymbol{s}_1$, are projected on the Cartesian coordinates system. Thus, the reciprocal lattice vector $\boldsymbol{H}$ can be written by,

$$\boldsymbol{H} = \boldsymbol{k}_1 - \boldsymbol{k}_0 = \frac{\boldsymbol{s}_1}{\lambda} + \frac{\boldsymbol{s}_0}{\lambda} \tag{3-22}$$

The conversion can be following steps:

(1) The measured points of the reciprocal space vectors always lie on the Ewald sphere, hence the positions on the Ewald sphere only depend on the detector angle ($\Delta 2\theta$). The new positions are resulted by an anticlockwise rotation as follows,

$$\begin{pmatrix} s_{1x\_rot} \\ s_{1y\_rot} \end{pmatrix} = \begin{pmatrix} \cos\Delta 2\theta & -\sin\Delta 2\theta \\ \sin\Delta 2\theta & \cos\Delta 2\theta \end{pmatrix} \begin{pmatrix} s_{1x} \\ s_{1y} \end{pmatrix} \tag{3-23}$$

where s_{1x_rot}, s_{1y_rot} are the new positions by detector scan, and s_{1x}, s_{1y} are the X-, Y-components in the Cartesian coordinates for the unit vector of the diffracted X-ray beam. Consequently, the new positions on the Ewald sphere depending on the $\Delta 2\theta$ are calculated by,

$$\begin{pmatrix} X_{EW} \\ Y_{EW} \end{pmatrix} = \begin{pmatrix} s_{0x} + s_{1x} \cdot \cos(\Delta 2\theta) - s_{1y} \cdot \sin(\Delta 2\theta) \\ s_{0y} + s_{1x} \cdot \sin(\Delta 2\theta) + s_{1y} \cdot \cos(\Delta 2\theta) \end{pmatrix} \tag{3-24}$$

where X_{EW}, Y_{EW} are the new positions on the Ewald sphere, s_{0x}, s_{0y} are the X-, Y-components in the Cartesian coordinates for the unit vector of the incident X-ray beam.

(2) The ω rotation allows that the new positions [H_x, H_y] in the reciprocal space are brought to the Ewald sphere. This is followed by a clockwise rotation,

$$\begin{pmatrix} H_x \\ H_y \end{pmatrix} = \begin{pmatrix} \cos\Delta\omega & \sin\Delta\omega \\ -\sin\Delta\omega & \cos\Delta\omega \end{pmatrix} \begin{pmatrix} X_{EW} \\ Y_{EW} \end{pmatrix} \tag{3-25}$$

The result ends up with two rotations transforming the obtained detector images into the reciprocal space maps. The obtained reciprocal space vectors H_x and H_y can be then written by,

$$\begin{aligned} H_x &= \frac{\cos\theta}{\lambda} \cdot (\cos(\Delta 2\theta - \Delta\omega) - \cos\Delta\omega) - \frac{\sin\theta}{\lambda} \cdot (\sin(\Delta 2\theta - \Delta\omega) - \sin\Delta\omega) \\ H_y &= \frac{\cos\theta}{\lambda} \cdot (\sin(\Delta 2\theta - \Delta\omega) + \sin\Delta\omega) + \frac{\sin\theta}{\lambda} \cdot (\cos(\Delta 2\theta - \Delta\omega) + \cos\Delta\omega) \end{aligned} \tag{3-26}$$

One example is shown in Figure 3.7(b) and (c), which measured the reciprocal space map of $Na_{0.5}Bi_{0.5}TiO_3$ single crystal. The research results using this method will be discussed in more detail in Chapter 5.

3.4. Powder diffraction for polycrystalline samples

Unlike a single crystal, a polycrystalline powder sample consists of many small grains (typically 1 ~ 10 μm) that are randomly oriented with respect to each other. Each grain has the same structure like single crystals, i.e. the same lattice, space group and fractional positions of atoms in the unit cell. Each point of the reciprocal lattice is consequently represented by a sphere instead of a single reciprocal lattice point. Therefore, the reciprocal space of a powder sample is the set of concentric spheres (see Figure 3.8).

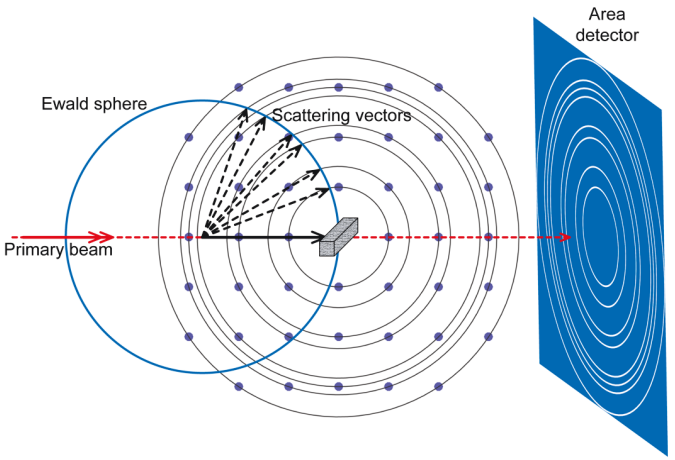

Figure 3.8 A schematic illustration of a method to observe a powder diffraction pattern. The area detector records the projection of all concentric spheres, the so-called 'Debye diffraction rings'.

Figure 3.9 shows an example of the powder diffraction patterns for the $BaTiO_3$ polycrystalline samples. Figure 3.9 (a) and (b) compare the two-dimensional powder diffraction rings between a cubic (a* = b* = c* = 1) and tetragonal (a* = b* = 1, c* = 0.98) structure. Figure 3.9(c) shows a one-dimensional powder diffraction cut profile as a function of the 2θ angle. The diffraction angle 2θ of any set of lattice planes (hkl) for the tetragonal symmetry ($a = b \neq c$, $\alpha = \beta = \gamma = 90°$) can be calculated from Bragg's law, which is described in Equation (3-27).

$$\sin^2\theta = \frac{\lambda^2}{4}\left(\frac{h^2 + k^2}{a^2} + \frac{l^2}{c^2}\right) \tag{3-27}$$

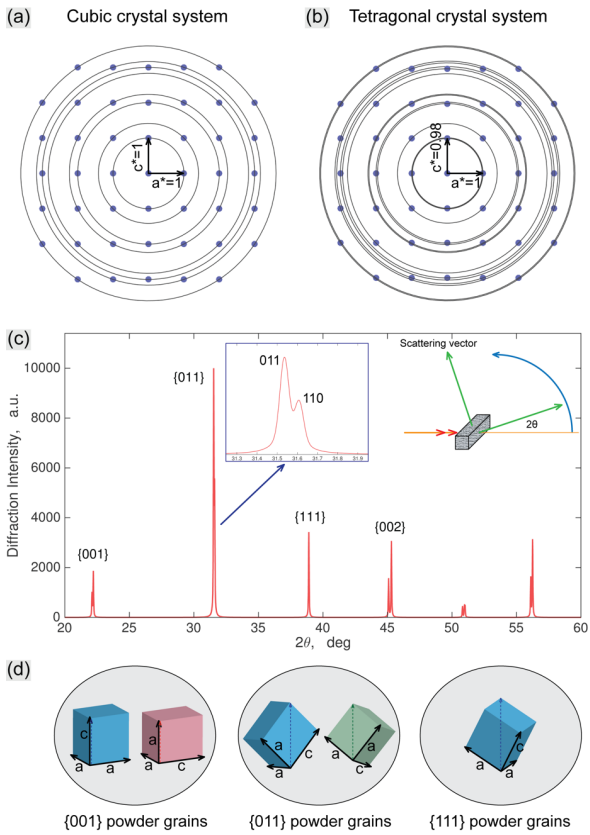

Figure 3.9 An example of the powder diffraction patterns for the $BaTiO_3$ polycrystalline samples. (a, b) Comparison of the diffraction patterns between cubic ($a = b = c$, $\alpha = \beta = \gamma = 90°$) and tetragonal ($a = b \neq c$, $\alpha = \beta = \gamma = 90°$) structure. (c) A simulated powder diffraction pattern of the tetragonal structure for the $BaTiO_3$. (d) The illustrations of possible three different {hkl} powder grains: the {001} and {011} peaks diffracted from two different oriented domains otherwise the {111} peak is from the single domain.

The sketches of possible three different {hkl} powder grains for the tetragonal structure are shown in Figure 3.9(d). Here, it notes that {hkl} denotes the 'family of the plane' (hkl). In the tetragonal symmetry ($a = b \neq c$) there are three different types: (i) two families, {100} consisting of (100), (−100), (010), and (0−10), and {001} involving (001) and (00−1), (ii) two families, {110} = {(110), (1−10)}, and {011} = {(011), (0−11), (101), (−101)}, and (iii) {111} = {(111), (−111), (−1−11), (1−11), (11−1), (−11−1), (−1−1−1), (1−1−1)} as a family (De Graef & McHenry [61], p. 93). Accordingly, the {001} and {011} powder grains involve two different families respectively, but the {111} powder grains include the same families along the scattering vector. Therefore, the tetragonal phase occurs the peak splitting on {001}, {011} peaks (see Figure 3.9(c)).

The powder diffraction is usually known as an important technique for the determination and refinement of crystal structures. The solution of a structure from powder diffraction is known as 'Rietveld refinement' [99]. It is named after Hugo Rietveld who developed the mathematical algorithms for the procedure of refinement.

Chapter 4

Stroboscopic data-acquisition for time-resolved X-ray diffraction

This chapter describes developments of the new strategies for time-resolved X-ray diffraction with custom-built data-acquisition systems. Section 1 introduces the operating principle of the multi-channel analyzer data-acquisition system. Section 2 demonstrates the new types of time-resolved X-ray diffraction methods implementing the stroboscopic data-acquisition systems.

4.1. Operating principle of stroboscopic data-acquisition system

The newly custom-built multi-channel analyzer data-acquisition system is able to achieve nanosecond time resolution [100].

In order to visualize the principle of the system, it is proposed to use a model of a stepwise rotating wheel (see Figure 4.1(a)). The wheel is divided into a given number of channels. Each channel of the rotating wheel is synchronously moved by a clock of 100 MHz, and the arriving photons are stored into those channels. One system provides 10000 channels supporting a multi-analyzer detector system, up to 12 detectors, and another system involves 100000 channels for a single-photon counter (e.g. scintillation detector, avalanche photo diode (APD) detector, etc.). The internal clock (10 ns) of the system, the so-called 'system internal clock', determines a time resolution for an experiment. The arrival time for each photon is analyzed in the model of the stepping wheel. The X-ray beam is detected by a single-photon counter. Each channel in the rotating wheel recognizes the rising edge of the arriving detector pulse(s), thus the caught photons can be stamped by the time delay (t_i) relative to the time (t_0) when the wheel began to rotate. A commercial field-programmable gate array (FPGA) board, based on the XILINX Spartan-6 platform, was used for the multi-channel analyzer unit. Functioning of the board can be designed by the VHSIC (Very High Speed Integrated Circuit) hardware description language, the so-called VHDL. The recorded data are read out by the control computer using applications written in the frame of commercial software programs: LabVIEW (National Instruments Inc., Austin, TX, USA) and MATLAB (The MathWorks Inc., Natick, MA, USA).

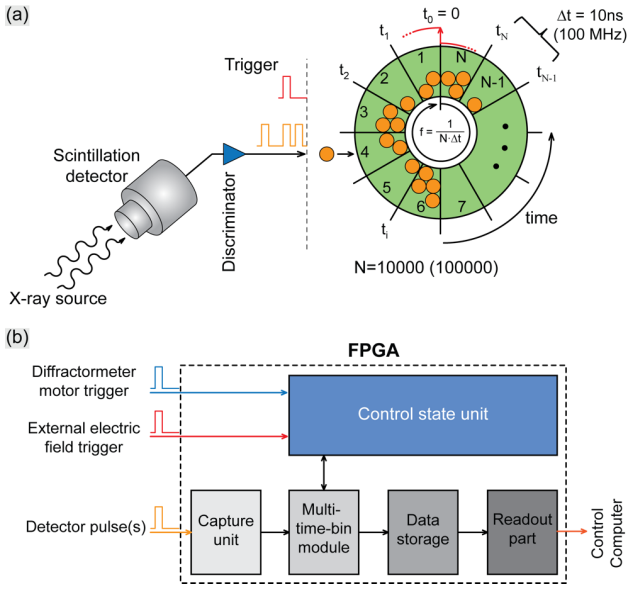

Figure 4.1 (a) Operating principle of the stroboscopic time-resolved data-acquisition system. X-ray photons are converted into electrical pulses, and the discriminated signals are analyzed by a rotating wheel with the given time-channels. The wheel is rotated stepwise by rising edges of 100 MHz internal clock. (b) A schematic diagram of the data-acquisition system architecture for time-resolved measurements. This architecture was designed in VHDL and implemented on FPGA-board.

A scheme of the data-acquisition system architecture is shown in Figure 4.1(b). There are five main functional parts: (i) Signal capture unit, (ii) Multi-time-bin module, (iii) Data storage, (iv) Control state unit, and (v) Readout part. The processing of the system is explaining more details as follows:

(1) *Signal capture unit - How to capture the arriving photons on the FGPA-board?*

If the arriving detector pulse(s) is/are short compared with the 'system internal clock' (100 MHz), then it can be utilized a method to catch the short duration pulses and synchronize them. A rising edge of the arriving detector pulse is converted to one of two logic states; either '0' or '1', the so-called 'captured detector pulse' (orange arrows in Figure 4.2(a)). The 'captured detector pulse' is synchronized by the leading edge from a next coming 'system internal clock' (red dashed line in Figure 4.2(a) and (b)), then the next falling edge of the 'system internal clock' (blue dashed line in Figure 4.2(a) and (b)) resets the 'captured detector pulse' to a logic signal '0' (blue arrows in Figure 4.2(a) and (b)).

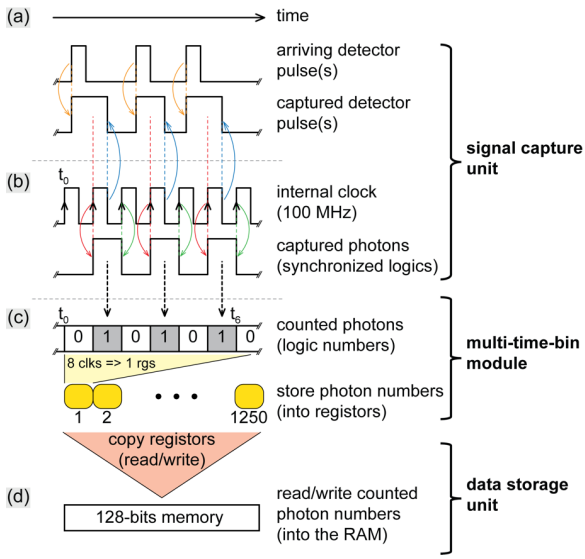

Figure 4.2 A schematic illustration for the functional design of the system architecture with 10 ns time resolution (Details are explained in the text).

Here, the specification of the detector pulse(s), its edge and amplitude, is limited by the discriminator. Detector pulses with amplitudes above 2 V and widths of at least 2.8 ns are captured and synchronized with the 'system internal clock' (100 MHz). The width of

the detector pulse over 10 ns is prevented for multiple-catching on the other channels of the rotating wheel. The synchronized logic, the so-called 'captured photon', is reset to '0' by the next coming rising edge of the 'system internal clock' (green arrows in the Figure 4.2(b)) and the system waits for the next coming 'captured detector pulse'. The arrival time of the 'captured photon(s)' is determined by the number of 10 ns channels which elapsed from the beginning of the external trigger signal (e.g. the applied electric field period).

This process is executed in the '*Signal capture unit*' on the FPGA-board.

(2) *Multi-time-bin module and Data storage unit - How to count/store the captured photons?*

Two units - '*Multi-time-bin module*' and '*Data storage unit*' - are working in parallel. The 'captured photon(s)' is/are counted and stored first into a dedicated register in the '*Multi-time-bin module*'. The register is defined as a simple chain of eight 1-bit stores corresponding to eight consecutive channels of a FPGA-memory involving eight 'system internal clocks' (see Figure 4.2(c)). A repeating process works on sliding register until the register reaches the end of the whole time-channels of the system. It is note that the process is repeating within the total channels in the FPGA-memory during each cycle of the external electric field. During this operation, the 'stored photon numbers' on each register are sent to the '*Data-storage unit*' (refer to Figure 4.2(c) and (d)). For example, the first time-channel didn't get any 'counted photons', which means the 'counted number' is zero. However, the next time-channel detected the 'counted photon' hence the 'counted number' becomes one. In doing so, in each of the time-channels a corresponding 'counted number' will be consequently stored.

In parallel, the '*Data-storage unit*' (see Figure 4.2(d)) receives a copy of all registers. This unit reads their content and adds all information to a 128-bits long portion of the system memory. The number of the 'counted photons' is finally stored in the RAM memory of the FPGA-board. This reading and writing progress requires five 'system internal clocks' (50 ns). The size of the allocated memory is 10000 channels with 16-bits words. The memory has two accessible ports. '*Port A*' with 1250 addresses is used for reading and writing operations during data gathering, and '*Port B*' is a USB-based port ('*Readout part*') for saving the data to the external control computer.

(3) *Control state unit*

This unit receives the external trigger and the diffractormeter movement signals, and it coordinates other units according to the synchronization scheme.

(4) *Re-binning operation mode*

If the external electric field provides the low repetition rates, then this mode is inevitable. It allows for an increase of the time-bin width, which becomes a multiply of 10 ns (e.g. 1 μs results from 10 ns × 100 time-channels).

4.2. New strategies for stroboscopic time-resolved X-ray diffraction

The custom-built data-acquisition systems are a standalone/portable module thus they can be easily implemented for several time-resolved diffraction experiments at different synchrotron facilities or even at the home-laboratory diffractometer system. This section introduces the developed powerful strategies to apply for stroboscopic time-resolved X-ray diffraction methods and describes how to perform them.

4.2.1. Application of stroboscopic time-resolved high-energy X-ray powder diffraction with a multi-analyzer detector system

One system supports diffraction data collection up to 12 parallel working wheels with 10000 channels. This system therefore can be combined with the multi-analyzer detector system and was utilized for stroboscopic time-resolved high-resolution X-ray powder diffraction experiments under an alternating external electric field, using high-energy (e.g. above 30 keV) synchrotron radiation. This new strategy has been recently performed at the ID22 beamline of European Synchrotron Radiation Facility (Grenoble, France) and at the P02.1 beamline of PETRA III (Hamburg, Germany) [100–102], because these beamlines provide the multi-analyzer detector system made of the single-photon counters are arranged with 1° separation [103–105]. This method could offer the opportunity to achieve sub-millidegree angular resolution and nanosecond time resolution [101,102].

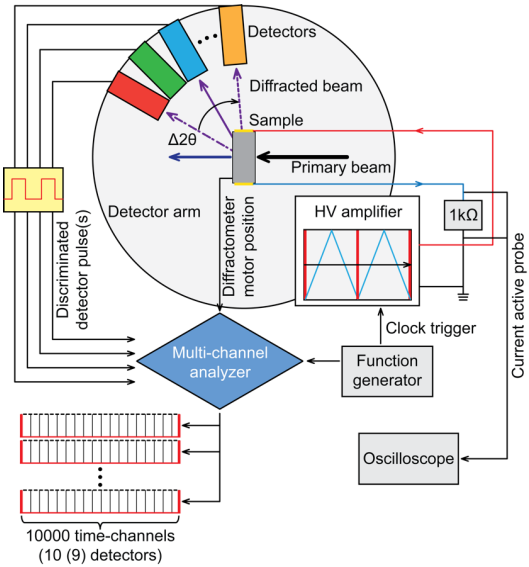

Figure 4.3 A scheme of stroboscopic time-resolved X-ray powder diffraction method with multi-channel analyzer detectors. The high-voltage generator (right) provides a cyclic electric field of adjustable amplitude and frequency. The beginning of each voltage cycle is marked by a clock trigger. The multi-channel analyzer detector (top left), consisting of ten (nine) scintillating counters equipped with analyzer crystals which collects high-resolution powder diffraction patterns. All of the discriminated detector pulses, clock triggers, and diffractometer rotation status are processed by the FPGA-based multi-channel analyzer unit.

This section describes the performance of the newly developed stroboscopic time-resolved X-ray powder diffraction method. The installation/operation manual is described in more detail in Appendix A.2. The system involves three independent components (see Figure 4.3); (i) a cyclic external electrical field, (ii) a multi-analyzer detector arm module, (iii) a programmable multi-channel analyzer data-acquisition system.

(1) The cyclic external electric field is produced by continuously supplying periodic high voltage signals (AMT-3B20, Matsusada) with external clock triggers which are provided by a commercial function generator (HMF-2550, Hameg). The trigger signals give

information on the beginning of each cycle of electric field. The functional voltage signals (e.g. amplitude, shape, frequency, etc.) can be directly controlled via the function generator.

(2) The arriving photons are detected by each scintillating counter on the detector arm, then the detected photons are initially processed to electrical rectangular pulses by the discriminator.

(3) All the discriminated detector pulses, the external clock signals and the diffractometer movement signals (or alternatively use trigger signals from exposure(s)) should be gathered into the multi-channel analyzer unit (blue diamond in Figure 4.3).

The data-acquisition is usually carried out in a step mode. In this mode, the synchronization between the data-acquisition system and the diffractometer during the measurements is achieved by getting the specially generated trigger signals with respect to the diffractometer movements. In other words, the system needs to recognize the running status of the diffractometer motor: '*moving motor*' or '*collecting data*'. This trigger signal is read by the FPGA-board to stop the data acquisition and save the new data point every time, when the status of the diffractometer motors changes from '*collecting data*' to '*moving motor*'. The acquisition for the next data point starts each time, when the status of the diffractometer changes back from '*moving motor*' to '*collecting data*'. Consequently, the system can synchronize every collecting data point at the beginning of the applying external electric field cycle. In order to collect a statistically sufficient number of photons per each time-channel, a measurement need to be repeated periodically with a large number of wheel rotations; typically, more than 1000 counts in each channel.

Figure 4.4(a) shows an experimental setup in the hutch of the ID22 beamline at the European Synchrotron Radiation Facility (Grenoble, France). This developed strategy is able to simultaneously measure the dielectric response of a material during the powder diffraction data collection. For this, a sample holder was newly designed, as shown in Figure 4.4(b). It was originally designed by John Daniel et al. [39] and improved by Tedi-Marie Usher et al. [106], but the previous things were not sufficient to record in parallel with the dielectric response. The new designed sample holder was improved for the part of the electrical connection and also consists of silicone oil bath (based on the Kapton foil), copper contact tip for applying external electric field as well. The applied voltage and electrical current signals can be recorded by the oscilloscope (HMO-3004, Hameg). The electrical current is measured by the responding voltage with 1 kΩ resistance in the series circuit (refer to Figure 6.3(a)). The Kapton foil cage is

filled up with a silicone oil (e.g. Silicone DC 200 fluid; 350 cst, Cat.No. 35136.01, SERVA Electrophoresis GmbH, Germany), because it can prevent a dielectric breakdown in air (~14 kV/cm) through the sample when the strong electric field (e.g. ~30 kV/cm) is applied. The sample holder can mount a ceramic with the thickness between 0.3 and 1 mm (the direction is along the incident X-ray beam).

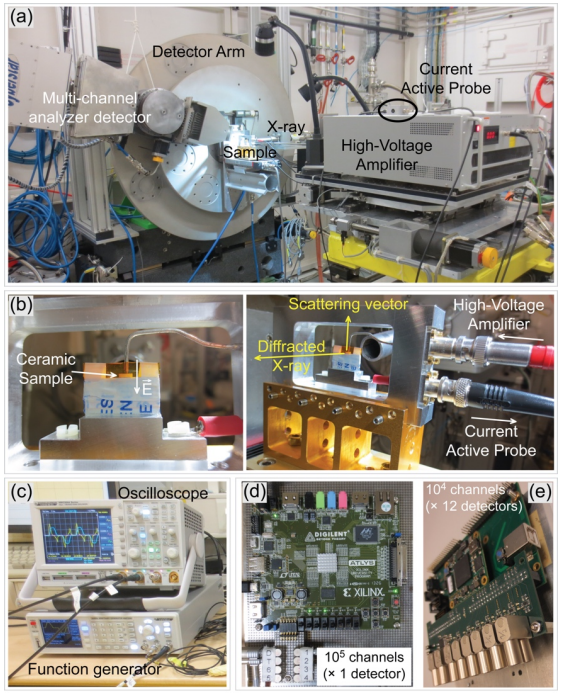

Figure 4.4 Photographs of (a) experimental setup and (b–e) the relative equipment for stroboscopic time-resolved powder X-ray diffraction at the ID22 beamline of the European Synchrotron Radiation Facility (Grenoble, France). (b) The improved sample holder for applying high voltage to the ferroelectric ceramic samples. (c) The oscilloscope can simultaneously record the data of the dielectric response during the diffraction measurements. (d, e) Types of the custom-built data-acquisition systems.

The geometry of the diffraction is a transmission mode, so that the primary beam is passing through the sample (refer to Figure 4.3). Figure 4.4(d) and (e) show the data-acquisition systems which are used in this work. One system (Figure 4.4(d)) provides 100000 time-channels for a single-photon counter. This system can cover 1 millisecond time period with 10 ns resolution. The advantage of this system is the capability to capture a fast switching phenomenon (e.g. on nanosecond time scale). Another system (Figure 4.4(e)) can simultaneously collect the diffraction profiles with up to 12 detectors. This system gives an advantage to decrease the number of electric field cycles, thereby reducing the fatigue effects under an applied electric field.

The research results will be described in more detail in Chapter 7.

4.2.2. Application for capturing a single bunch structure with 2 ns resolution

This section describes the revolutionarily developed strategy to capture a single bunch structure at a synchrotron facility with 2 ns resolution.

Most time-resolved diffraction experiments using a continuous X-ray source are achieved in 10 ns resolution, because the global operations of the used FPGA-platform are practically limited to the 100 MHz internal clock ranges. If the experiments however will need a fine temporal resolution below 10 ns, then it is essential to take an additional advantage of a serial-to-parallel converter with an ultrafast speed. The convertor is a part of the FPGA-chip and provides the ultrafast data transmission speed into the memory up to 1 Gb/s. In order to achieve 2 ns resolution, an internal clock of the convertor was configured to 500 MHz and hence the length of a converter register is set to five locations (refer to Figure 4.5). The operating principle is described as follows,

(1) The discriminated detector pulses firstly arrive into the register of the convertor and are synchronized with an internal clock of the convertor. Therefore, the 'captured detector pulses' can be stamped with 2 ns resolution.

(2) The five registers are connected in parallel with five 'multi-time-bin modules' (refer to Section 4.1) working at the speed of 100 MHz system internal clock (see Figure 4.2). Since the output of each register is latched onto five parallel running modules, every 10 ns the arriving photons are counted and stored into the system memory.

(3) Finally, every 5×10000 time-bin is re-sorted into one single data stream by off-line procedure on the control computer.

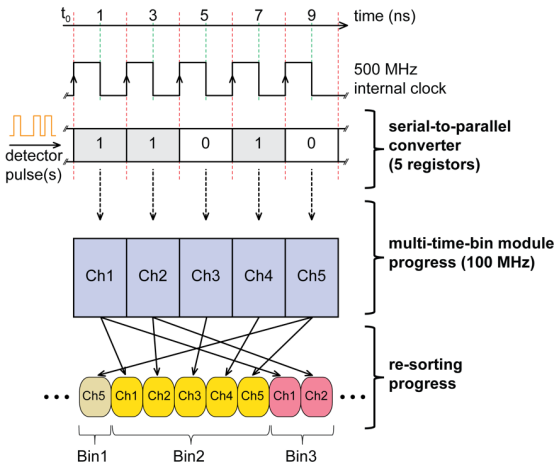

Figure 4.5 A schematic diagram of the functional design of the 2 ns resolution which makes use of 500 Mb/s serial-to-parallel converter register and five parallel running 10 ns resolution 'multi-time-bin module' in the FPGA-board.

Since modern synchrotron facilities store X-ray bunches, it is able to study ultrafast dynamics of materials during the applied external perturbation (i.e. pump-probe technique).

In order to isolate a single bunch, it is normally used the gated mode option of an area detector (e.g. Pilatus, etc.). A bunch clock is used as the master clock providing MHz ranges. However, the repetition rates for the external perturbations (e.g. femtosecond laser pulse(s) or nanosecond electric pulse(s)) are generally used with kHz ranges. Hence, it is necessary to reduce the original frequencies of the bunch clock down to the practical repetition rates (e.g. ~ kHz). This is typically implemented by a delay generator (e.g. DG645, Stanford research: see Figure 4.6(c)) to divide the frequencies. Here the original bunch clock signal is given to the delay generator, and then divided to the optimized frequency. Furthermore, the delay generator creates an additional given

pulse to be used for a gating period of the area detector. Finally, a beginning of the external perturbation pulse(s) is/are synchronized with the X-ray bunch pulse(s), and then the single bunch is isolated into the gated period of the detector.

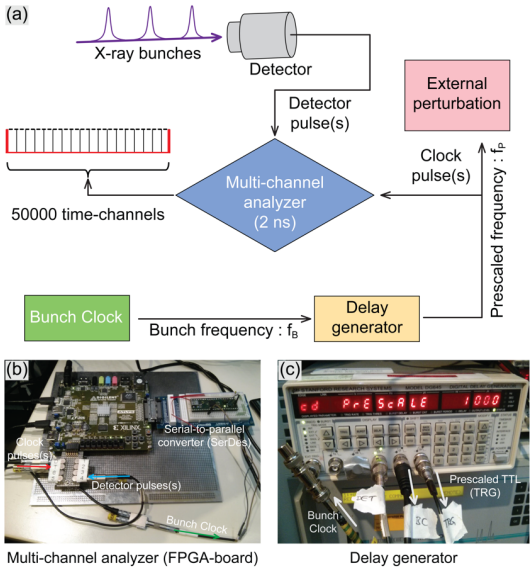

Figure 4.6 A schematic illustration (a) and photographs (b, c) of the experimental setup in order to capture the X-ray bunch structures with the multi-channel analyzer data-acquisition system. This measurement was performed at the XPP-KMC3 beamline of the BESSY II synchrotron facility (Berlin, Germany)

The newly upgraded data-acquisition system was employed to capture the bunch-structure at the XPP-KMC3 beamline of the BESSY II synchrotron facility (Berlin, Germany), shown in Figure 4.6. Each time-channel of the system works like as a gating period of the area detector. This system is able to simultaneously collect data up to 100 μs long time period with 2 ns resolution. A fast X-ray scintillation detector was exposed to the attenuated synchrotron radiation. The multi-channel analyzer unit (FPGA-board) was connected to an external phase-locked loop (PLL) circuit and synchronized with the bunch-clock (see Figure 4.6(b)).

Figure 4.7(a) shows the observed bunch structures of the X-ray beam providing the multi-bunch hybrid mode. Figure 4.7(b) shows the reference pattern from the status information of the BESSY II synchrotron [107]. The bunch structure has a period of 800 ns. It consists of a 'Camshaft bunch' in the center of 200 ns wide gap followed by the so-called 'PPRE-bunch' after 84 ns and three slicing bunches located on top of the multi-bunch train (600 ns). The results clarify that the innovatively developed strategy opens the window to perform new types of experiments, e.g. to measure ultrafast dynamics of piezoelectric/ferroelectric materials under an alternating electrical perturbation with ~ MHz frequencies.

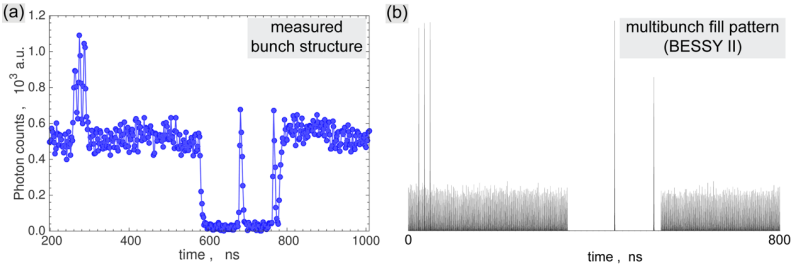

Figure 4.7 (a) The selected X-ray bunch structure from the observed data on the multi-bunch hybrid mode at the BESSY II synchrotron (Berlin, Germany). (b) Reference bunch structure from the status information of the storage ring facility [107].

4.2.3. Application of stroboscopic time-resolved reciprocal space mapping

This section describes a developed powerful strategy to observe the dynamics of multi-domain mesoscopic structure of crystals. It is a stroboscopic time-resolved high-resolution reciprocal space mapping method. As introduced in Chapter 3, the reciprocal space mapping is useful tool to investigate the mesoscopic structural properties of crystals. Combining the custom-built data-acquisition system with a single-photon counter placed behind an analyzer crystal, it can be achieved to measure the multi-domain dynamics in different regions of reciprocal space under an alternating electric field.

This newly developed strategy was successfully performed at the P08 beamline of the PETRA III storage ring (Hamburg, Germnay). Figure 4.8 shows a sketch of the experimental setup.

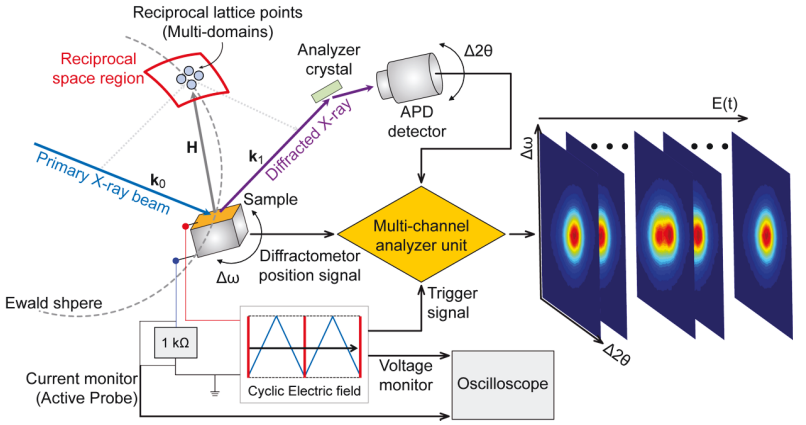

Figure 4.8 A sketch of the stroboscopic time-resolved high-resolution reciprocal space mapping process: The diffracted signal is collected using a single-photon counter (e.g. APD detector) placed behind a Si(111) analyzer crystal in (rocking) versus 2θ (scattering) scan mode. A cyclic triangular-shaped electric field with a given repetition rate is applied to the sample. Detector signals are processed using the custom-built stroboscopic data-acquisition system.

A new sample holder was specifically designed for mounting single crystals. This developed sample holder can monitor the capacitive current, polarization and hysteresis loop via serially connected 1 kΩ resistor (refer to Figure 6.3(a)). More details are available in Chapter 5 and Appendix B.1. A combination of a function generator (HMF-2550, Hameg) and a high-voltage amplifier (AMT-3B20, Matsusada) produce an AC electric field to the sample with given periodic frequencies and shapes. The diffraction intensity can be measured as a function of (rocking) and 2θ (scattering) angles around the selected Bragg reflection position of the reciprocal space. Since the step mode of the data-acquisition system is used, the experiment can be accomplished

for stroboscopic time-resolved high-resolution reciprocal space mapping. A manual to install the data-acquisition system is described in Appendix A.1.

This strategy has been successfully applied using a home-lab diffractometer system. However, it took at least 3 weeks to make only one map of a strong Bragg reflection. For this reason, synchrotron facilities are necessary to apply this innovative strategy. This strong application opens the window to investigate dynamics of multi-domains in bulk single crystals under an alternating electric field for the first time.

The research results regarding this application will be discussed in more detail in Chapter 5.

4.2.4. Application of stroboscopic time-resolved three-dimensional reciprocal space mapping using a microcontroller based data-acquisition system

This section describes another innovative strategy for stroboscopic time-resolved three-dimensional (3D) reciprocal space mapping of piezoelectric/ferroelectric single crystals under an alternating electric field using a new designed microcontroller based data-acquisition system [108].

A 3D reciprocal space mapping is a powerful tool to study a crystal structure at various length scales. The local structure and the correlated disorder due to the compositional variations of a material clearly appear in the X-ray diffuse scattering underneath the Bragg reflections. An *in situ* single crystal total - Bragg and diffuse - scattering experiment under controlled external perturbations, e.g. temperature, electric/magnetic field, can help to clarify the strong link between disorder and properties of modern functional materials. The equipment for such experiments (fast area detectors, sample environment stages, etc.) underwent a steady development in recent years.

The previous sections discussed the applications of the multi-channel analyzer data-acquisition system using the single-photon counter(s). In contrast, the new strategy to approach for a stroboscopic measurement under an alternating electric field uses a pixel area detector (e.g. Pilatus, Eiger, Maxipix, Lambda, etc.). Time resolution of this experiment is defined/limited by the frame acquisition rates of the detector's specification. According to the current state-of-the-art pixel area detectors, a few milliseconds time resolution can be achieved if the diffraction intensity is sufficient.

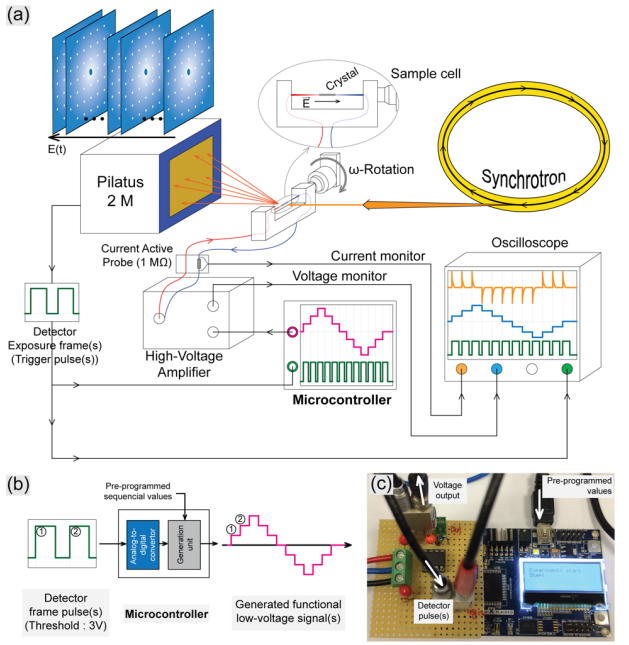

Figure 4.9 Schemes (a, b) and a photograph (c) of the presented data-acquisition system. The pixel area detector (e.g. PILATUS-2M, DECTRIS, Switzerland) generates rectangular trigger signals (green signal), which mark the beginning of a new data acquisition frame. The microcontroller acquires these signals and switches the output voltage (pink signal) every time their rising edges overshoot 3 V (b). The electric (capacitive) current flowing (yellow signal in the oscilloscope) through the crystal is measured using a serially connected 1MΩ active probe.

The main components of this new method shown in Figure 4.9 are (i) a programmable microcontroller, (ii) a high-voltage amplifier, and (iii) a pixel area detector. A manual to install/operate the systems is explained in more detail in Appendix A.3. The operating principle of this application is described as follows,

(1) The microcontroller acquires the detector pulses, where each pulse marks an individual exposure frame. The exposure time (detector pulse width) can be directly controlled by the detector software.

(2) The leading edge of each detector pulse is automatically recognized and used by the microcontroller in order to switch the output voltage between sequential values (see Figure 4.9(b)). In other words, the detector and the microcontroller operate as a master and slave mode, respectively.

(3) The generated output voltage signals from the microcontroller are sent to the high-voltage amplifier, and then the output high-voltage of the amplifier is directly connected to the sample holder. The time resolution of the experiment is entirely limited by the detector frame acquisition (exposure) time: the current model of the PILATUS-2M detector (DECTRIS, Switzerland) provides the smallest frame width of ~33 ms.

(4) Accordingly, the microcontroller system can be used as a commercial function generator with a broad frequency range, set by PILATUS-2M or any other area detectors that can serve as a master clock.

This new powerful method has been successfully applied to study a functional piezoelectric/ferroelectric single crystal of $Pb(In_{1/2}Nb_{1/2})O_3$-$Pb(Mg_{1/3}Nb_{2/3})O_3$-$PbTiO_3$ (PIN-PMN-PT) [109], and using PILATUS SNBL diffractometer [110] at the Swiss-Norwegian Beamline (SNBL) BM01 of the European Synchrotron Radiation Facility (Grenoble, France). For the experiment, a single crystal prepared with a cylindrical shape and diameter of ~0.1 mm and length of ~1 mm was mounted into the custom-built sample cell to apply an external electric field [111,112]. The electrical current through the dielectric crystal was simultaneously measured using serially connected 1 MΩ active probe. The microcontroller was programmed as 20 steps to produce triangularly modulated periodic high-voltage signal (pink triangular steps in the Figure 4.9(a) and (b)). The PILTATUS-2M detector was operated by 20 frames per second and therefore the repetition rate of the generated electric field is 1 Hz. The intensity map was obtained by a stepwise rotation mode: the crystal is rotated around the -axis with an angular step of 0.01º. At each -step, 80 sequential detector frames were acquired (i.e. applied four cycles of the electric field). The 80 measured detector frames could be binned into every 20 time-steps, using an in-house Python script.

This section introduced the newly developed strong strategy for *in situ* stroboscopic 3D reciprocal space mapping using the microcontroller based data-acquisition system. The new application opens the window to investigate dynamics of a piezoelectric/ferroelectric single crystal under an applied alternating electric field. This system is also portable and can be adapted to any beamline, which provides a pixel area detector.

4.3. Conclusion

This chapter introduced/discussed the newly developed powerful strategies for stroboscopic time-resolved X-ray diffraction using the new data-acquisition systems. These applications opened the new windows to have an insight into dynamics of piezoelectric/ferroelectric materials under an alternating electric field. The strategies have been successfully applied at several synchrotron facilities even at a home-laboratory diffractometer system.

Chapter 5

Stroboscopic time-resolved high-resolution reciprocal space mapping study of $Na_{0.5}Bi_{0.5}TiO_3$ single crystal under an alternating electric field

This chapter investigates the monoclinic distortion and the polarization rotation in $Na_{0.5}Bi_{0.5}TiO_3$ single crystal under an applied alternating electric field using synchrotron-based time-resolved high-resolution reciprocal space mapping. Moreover, a developed model explains the monoclinic distortion by polarization rotation and evaluates the intrinsic piezoelectric coefficients of the material from the observed data.

5.1. Introduction

Sodium bismuth titanate ($Na_{0.5}Bi_{0.5}TiO_3$ – NBT) has been extensively investigated over the last two decades [113–115]; especially as a lead-free piezoelectric material as a replacement for $Pb(Zr_{1-x}Ti_x)O_3$ (PZT) [116–119]. NBT is also an interesting model system in crystallography and physics because of its distorted perovskite structure. Phase transitions in NBT are realized through shifts of the **A**/**B** cations and by tilting of the oxygen TiO_6 octahedra which lowers the symmetry (see Figure 5.1). This symmetry reduction results in the formation of domains, which are spontaneously polarized, electromechanically active and switchable by an external electric field. Although the average/local structure of NBT materials are discussed in various aspects, the relationship to its physical properties is still unclear because of its complexity.

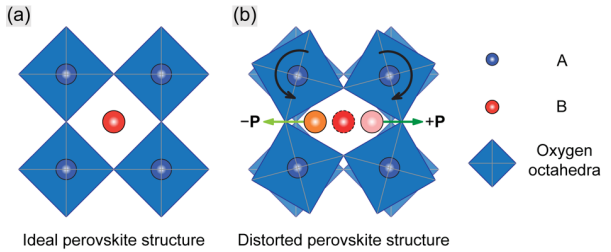

Figure 5.1 An illustration of a phase transition in the perovskite structure. (a) An ideal perovskite structure (cubic symmetry). (b) A distorted perovskite structure: displacement of **B** atom at different polarity and tilt of the oxygen octahedra (lower symmetry, e.g. tetragonal).

NBT was commonly considered to exhibit a rhombohedral structure (space group *R3c*) at room temperature [120]. However, based on high-resolution single crystal diffraction data, Gorfman & Thomas [121] have reported that the structure of multi-domain NBT single crystals at room temperature is described by the monoclinic space group *Cc*. They explored by reciprocal space mapping, a splitting of the particular Bragg reflections $\{hkl\}_{pc}$ (each component is diffracted from a similarly oriented set of ferroelastic domains) which violates the rhombohedral *R3c* symmetry. The monoclinic distortion may play an important role in the enhancement of the electromechanical properties. It can act as a bridge between the rhombohedral and tetragonal phases. While the direction of the polarization vector in a conventional ferroelectric rhombohedral phase is fixed in the [111] direction, the monoclinic symmetry allows the polarization vector to rotate in a (110) mirror plane [75] and responds by an enhanced polarization rotation and strain to an external electric perturbation [77]. For this reason, the monoclinic symmetry of NBT at room temperature has been investigated by many authors [122–126].

This chapter demonstrates the study of the monoclinic distortion in NBT under an alternating sub-coercive (< 14 kV/cm) external electric field. For this, reciprocal space maps around representative Bragg reflections [121] were collected. The observed data indicate that the monoclinic splitting is strongly sensitive to the external electric field. The field-induced shifts of the Bragg peaks amount to a piezoelectric coefficient as high as 124 pC/N.

5.2. Experiment: stroboscopic time-resolved reciprocal space mapping under an alternating electric field

Figure 5.2 shows the experimental setup and the installed electronic equipment at the P08 beamline of the PETRA III synchrotron facility (Hamburg, Germany). A 0.5 mm thick NBT single crystal plate, which has its surface parallel to the (001) Miller planes and the edges along the <110>[1] and <100> directions respectively (Figure 5.2(b)), was used. It was grown in the Shanghai Institute of Ceramics by the top-seeded solution growth method and doped with Manganese (Mn) [127]. Thin (~100 nm) gold (Au) electrodes were deposited on both of the crystal surfaces and the crystal was mounted on a custom-built sample holder (refer to Figure 5.2(c) and Figure B.1 in Appendix B) in order to apply an alternating external electric field along the [001] crystallographic direction. In this experiment, a 100 Hz periodic triangular-shaped electric field reaching a maximum field strength of ±14 kV/cm was applied to the sample. This field is significantly lower than the coercive field (~45 kV/cm), reported for Mn-doped NBT single crystal [128]. For the time-resolved high-resolution reciprocal space mapping, the custom-built stroboscopic data-acquisition system, described in more detail in Chapter 4 (Figure 4.8) and Appendix A (Figure A.1), was implemented.

Each data point of the reciprocal space mesh scans was collected for 10 seconds, which is equal to 1000 cycles of the applied electric field. The X-ray wavelength was λ = 0.827 Å, which is below the 'Bi' L2 absorption edge, making the average penetration depth for the measured reflection as $\langle t \rangle = \frac{1}{2} sin\theta$ = 5.3 µm. This value is ~2.5 times larger than the penetration depth used in the previous experiment [121]. Therefore, this experiment provides bulk information about the crystal.

[1] <*uvw*> denotes the 'family of directions' (De Graef & McHenry [61], p. 93): <110> has 12 families consisting of [110], [−110], [1−10], [−1−10], [101], [−101], [10−1], [−10−1], [011], [0−11], [01−1], and [0−1−1].

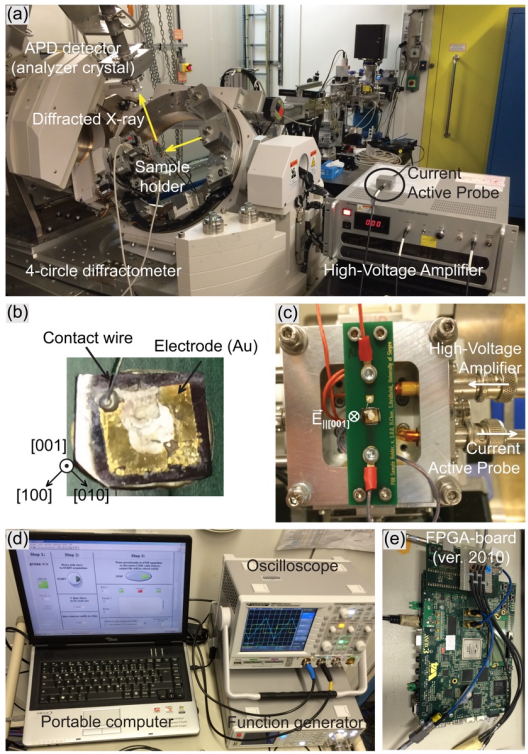

Figure 5.2 Photographs of the experimental setup at the P08 beamline of the PETRA III synchrotron facility (Hamburg, Germany). (a) Inside the hutch of the P08 beamline with the 4-circle diffractometer. (b) Crystallographic axes of NBT single crystal and (c) the sample holder for applying the electric field. (d, e) Electronic devices for data acquisition under alternating electric fields.

5.3. Results

5.3.1. Experimental data

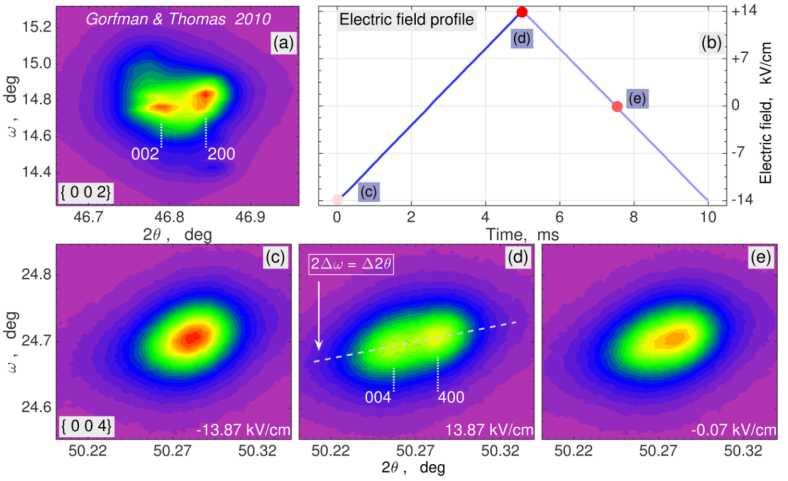

Figure 5.3 (a) ω versus 2θ reciprocal space map of {002} reflections from the measured data set of the previous experiment [121] and (b) time dependence of applied external electric field. (c–e) Stroboscopically collected ω vs 2θ reciprocal space maps of {004} reflections, corresponding to different time-channels and applied electric fields. The splitting of peaks along the 2θ axis is assumed to represent evidence for breaking of the rhombohedral (*R3c*) symmetry of the structure and is commonly recognized as the 'fingerprint' of the monoclinic distortion.

Figure 5.3(a) shows the ω versus 2θ intensity reciprocal space map around {002} reciprocal lattice points from the previous studies [121]. Figure 5.3(c–e) show the selected time-resolved reciprocal space maps on {004} reflections as a function of time and electric field with 100 Hz repetition frequency. The selected time points are marked on the electric field profile, as shown in Figure 5.3(b). All time-resolved data are shown in Video D.1 of Appendix D. Figure 5.3(d) shows that the peak is split into two peak components along the 2θ scattering angles, which correspond to different lengths of the reciprocal lattice vector, $H = 2sin\theta/\lambda$. Therefore, the peak separation reflects the

break of the rhombohedral *R3c* symmetry ($a^* = b^* = c^*$) of the domains. Gorfman & Thomas [121] demonstrates the analysis of such peak separation in other families of Bragg reflections and suggests that the average pseudo-cubic lattice should have the parameters, $a = b \neq c$ and $\alpha = \beta \neq \gamma$, with a (1−10)-oriented mirror plane. Considering the octahedral tilt system, the structure of NBT crystal at room temperature can be described by the monoclinic *Cc* space group - a subgroup of the rhombohedral *R3c*. For this reason, the separation of the observed peak along the 2θ direction provides direct access to the monoclinic distortion parameter $\Delta c/c$ and it can be shown that this monoclinic distortion is induced by the applied external electric fields.

5.3.2. Two-dimensional reciprocal space map fitting results

This section describes the fitting process to determine the two components which can explain the peak separation in the two-dimensional (2D) reciprocal space maps (refer to Appendix C). In this study, the sum of two symmetrical 2D Moffat distribution functions was considered instead of the 2D pseudo-Voigt functions. The 2D Moffat distribution function is defined by a continuous probability distribution based on the Lorentzian distribution. This function is frequently used in astrophysics because of its capability to accurately reconstruct point spread functions in 2D distributions.

The 2D Moffat distribution function is written by,

$$f(x,y) = I\,\frac{4\left(2^{\frac{1}{\beta}}-1\right)(\beta-1)}{\pi\sigma_x\sigma_y}\left[1+\left(4\left(2^{\frac{1}{\beta}}-1\right)\right)\left(\frac{(x-x_0)^2}{\sigma_x^2}+\frac{(y-y_0)^2}{\sigma_y^2}\right)\right]^{-\beta} \qquad (5\text{-}1)$$

containing six adjustable parameters: the integrated intensity I, the center of mass of peak positions (x_0, y_0), the peak widths (σ_x, σ_y), and the peak shape parameter β. The MATLAB analytical package (version R2015a; The MathWorks Inc., Natick, MA, USA), which makes use of the interior-point algorithm in the *fmincon* function [129], was used to find a minimum of the χ^2 value defined by,

$$\chi^2 = \sum_i \omega_i \left(I_i^{(\ bs)} - I_i^{(Calc)}\right)^2 \qquad (5\text{-}2)$$

where $I_i^{(\ bs)}$ and $I_i^{(Calc)}$ are the observed and calculated intensities at the i-th position respectively, and $\omega_i = \frac{1}{\sqrt{I_i^{(Ob\ )}}}$ is a weighting parameter associated with $I_i^{(\ bs)}$.

The results of the time- and field-dependent fitting parameters are available in Appendix C.2.

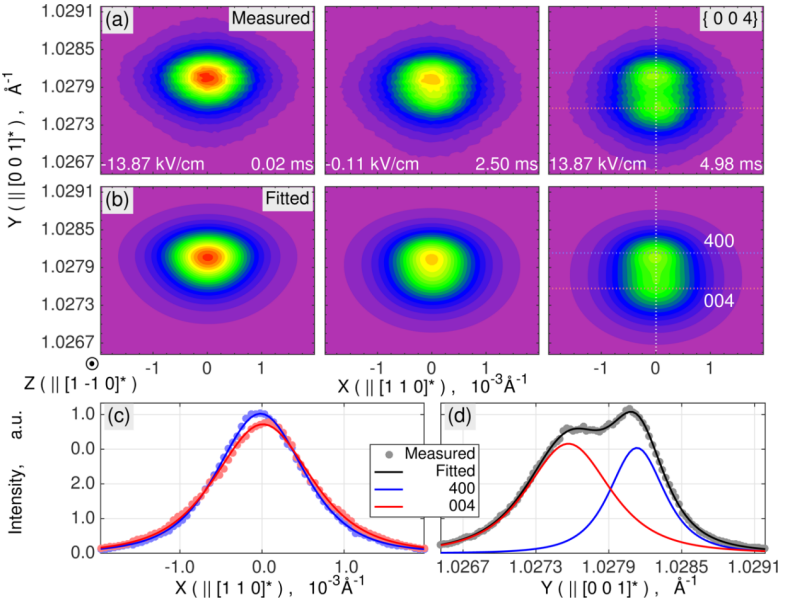

Figure 5.4 Reciprocal space maps of X-ray scattering intensity distribution around {004} reflections in the reciprocal lattice coordinates X || [110]* and Y || [001]*. (a) The observed reciprocal space maps. (b) The result of the best fit by the superposition of two 2D Moffat distribution functions. (c, d) X- and Y-intensity cut profiles of 400 (blue) and 004 (red) Bragg peak components, respectively. All time-resolved data are shown in Video D.2 of Appendix D.

Figure 5.4(a) shows the observed reciprocal space maps, selected for three different electric fields (−13.9 kV/cm, 0 kV/cm and +13.9 kV/cm). The observed reciprocal space maps are transformed into the Cartesian coordinates with the horizontal axis X || [110]* and the vertical axis Y || [001]*, i.e. the Y-axis is parallel to the scattering vector and is equal to the $\Delta(2\theta) = 2(\Delta\omega)$ direction (as shown by the dashed line in Figure 5.3(d)). Since the detector opening is perpendicular to the diffraction plane, the diffraction intensity is integrated along Z || [1−10]*. Figure 5.4(b) indicates the reconstructed 2D maps using the best fit parameters. Figure 5.4(c) and (d) show the cut profiles of reciprocal space map along [110]* and [001]*, respectively. These peaks clearly show the peak separation in two components: the '004' peak (red) is shifted towards the value of a lower scattering vector while the '400' peak (blue) stays at almost the same position.

The results of the fitting procedure enable the tracking of the positions and the width of both peaks quantitatively. Figure 5.5 shows the field dependence of the key model parameters for both contributing Bragg peaks. These are (a) peak positions and (b) peak width, along [001]* and [110]*, respectively.

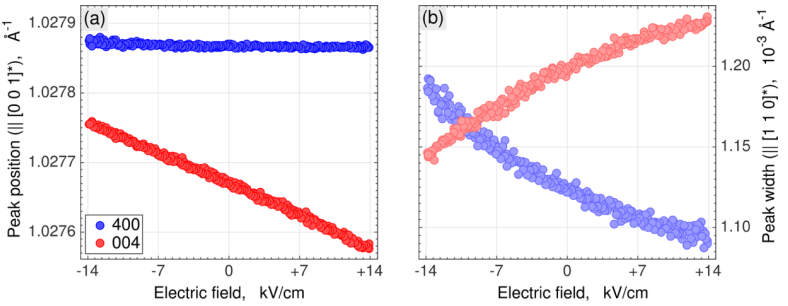

Figure 5.5 Best-fit results for both 'peak position' and 'peak width' parameters of 400 (blue) and 004 (red) reflections as a function of the applied electric field. (a) Y-component of the peak position. (b) X-component of the peak width.

5.4. Interpretation and discussion

5.4.1. Model of monoclinic distortion and polarization rotation

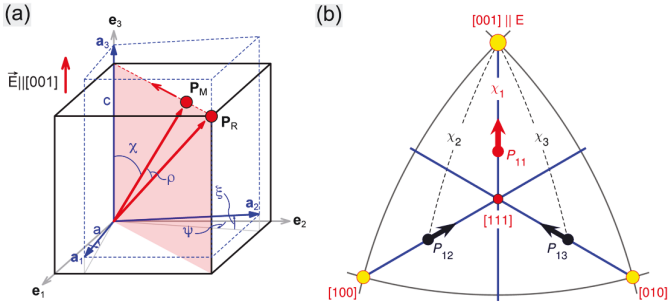

Figure 5.6 A model of the monoclinic distortion and the polarization rotation. (a) The distortion of the monoclinic unit cell is due to the rotation of the polarization vector P_M away from one of the P_R = <111> (cube body diagonal) direction in the monoclinic mirror plane by the angle ρ. The model for the distortion of the unit cell considers four ρ-dependent parameters (Δc, Δa, Δ , Δ) – Δc, Δa are the deformations along the unit cell edges in and out of the polarization rotation plane, and Δ , Δ correspond for shearing the unit cell. (b) The stereographic projection of the polarization rotation planes and directions in the representative monoclinic domains M_{11}, M_{12}, and M_{13}.

For an interpretation of the results, a crucial model with respect to the formation of the monoclinic distortion is considered. Figure 5.6 shows the distortion of the pseudo-cubic unit cell through the phase transition from the rhombohedral *R3c* ($a = b = c$, $\alpha = \beta = \gamma$) to the monoclinic *Cc* ($a = b \neq c$, $\alpha = \beta \neq \gamma$) structure. The model of the monoclinic distortion involves changes in the following parameters: Δc, Δ , Δ , and $\Delta\xi$. Here, Δc and Δ are the variation of the pseudo-cubic lattice length in the directions in and out of the polarization rotation plane (pink area in Figure 5.6(a)) respectively, and the two angles, Δ and $\Delta\xi$, are related to the unit cell shearing. These deformations are also

connected to the polarization rotation angle ρ, which is the angle between the monoclinic $\boldsymbol{P}_M$ and the rhombohedral $\boldsymbol{P}$ polarization directions. If the polarization vector rotates from [111] towards the [001] direction in the monoclinic mirror plane, then the length of the vector $\boldsymbol{c}$ increases along the [001] direction by Δc. The other vectors, $\boldsymbol{a}$ and $\boldsymbol{b}$, change their lengths by Δa and rotate by both Δ and Δ angles, simultaneously. This model is available as an animation in Video D.3 of Appendix D. The corresponding phases were previously referred to monoclinic M_A ($\rho > 0$) and M_B ($\rho < 0$) phases (refer to Figure 2.9(a)) [73,75]. The loss of the three-fold rotational symmetry during the phase transition results in the formation of three differently oriented monoclinic domains, i.e. the polarization rotates either towards the [001], [100] or [010] direction with respect to the parent rhombohedral *R3c* phase.

The domains, where the polarization can rotate towards the electric field (along one of the pseudo-cubic directions), are referred as the possible three monoclinic domains, called M_{11}, M_{12}, and M_{13}. Figure 5.6(b) shows the defined three monoclinic domains. The further monoclinic domains can be created from the rhombohedral domains with the polarization along the other <111> body diagonals involving the eight different directions: [111], [−111], [1−11], [−1−11], [11−1], [−11−1], [1−1−1], and [−1−1−1]. Although such phase transition may form 24 monoclinic domains, this study considers only four rhombohedral domains with the polarization along the [111], [−111], [1−11], [−1−11] body diagonals, resulting in 12 monoclinic domain variants only, because the applied external electric field was lower than the coercive field. These 12 monoclinic domains will be marked as M_{mn} (m=1,2,3,4 corresponds to $\boldsymbol{P}$ || [111], $\boldsymbol{P}$ || [−111], $\boldsymbol{P}$ || [1−11], $\boldsymbol{P}$ || [−1−11], and n=1,2,3 with $\boldsymbol{P}$ being parallel to $\boldsymbol{P}$ and [001], [100], and [010] respectively).

5.4.2. Features of the diffraction peaks under an applied electric field

This section describes the features of the obtained diffraction peaks appearing under the influence of the external electric field by the changes of the representative three monoclinic domains. Schematic diagrams of the three monoclinic domains are shown in Figure 5.7.

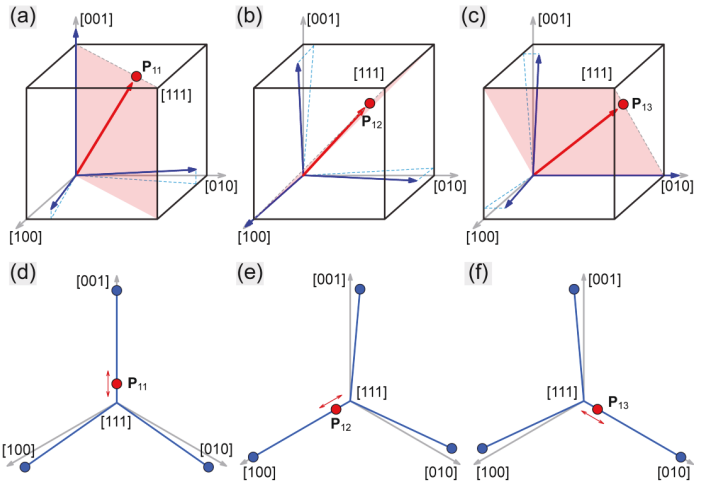

Figure 5.7 (a–c) Schematic illustrations of three representative monoclinic domains, M_{11}, M_{12}, and M_{13}, respectively. (d–f) The projection views from the [111] direction for three domains.

(1) Monoclinic domain M_{11}

Figure 5.7(a) and (d) show the case of monoclinic domain M_{11}. The calculated orientation matrix for the M_{11} monoclinic domain is

$$\left[U_A^{(11)}\right] = \begin{pmatrix} a\cos & \cos & a\cos & \sin & 0 \\ a\cos & \sin & a\cos & \cos & 0 \\ a\sin & & a\sin & & c \end{pmatrix} \tag{5-3}$$

The columns of this matrix are the coordinates of the pseudo-cubic basis vector $\boldsymbol{a}_i$ relative to the Cartesian coordinate system $\boldsymbol{e}_i$ (refer to Figure 5.6(a)).

The reciprocal orientation matrix of the domain $\left[U_B^{(mn)}\right]$ (the columns are the reciprocal basis vectors $\boldsymbol{a}_i^*$, so that $\boldsymbol{a}_i\boldsymbol{a}_j^* = \delta_{ij}$) can be constructed by,

$$[\ _B] = [\ ^T_A]^{-1} \tag{5-4}$$

Hence, the reciprocal orientation matrix of the domain M_{11} is written by,

$$\left[U_B^{(11)}\right] = \begin{pmatrix} \dfrac{\cos}{a\ \cos\quad \cos 2} & \dfrac{-\sin}{a\ \cos\quad \cos 2} & \dfrac{-\quad \mathrm{n}}{\sqrt{2}c\ \sin\left(\frac{\pi}{4}+\ \right)} \\ \dfrac{-\sin}{a\ \cos\quad \cos 2} & \dfrac{\cos}{a\ \cos\quad \cos 2} & \dfrac{-\quad \mathrm{n}}{\sqrt{2}c\ \sin\left(\frac{\pi}{4}+\ \right)} \\ 0 & 0 & \dfrac{1}{c} \end{pmatrix} \tag{5-5}$$

The reciprocal lattice vectors, $\boldsymbol{a}^*$, $\boldsymbol{b}^*$, and $\boldsymbol{c}^*$, of the domain M_{11} are accordingly,

$$\boldsymbol{a}^*{}_{(11)} = \left\{\frac{\cos}{a\cos\quad\cos 2},\ \frac{-\sin}{a\cos\quad\cos 2},\ 0\right\}$$

$$\boldsymbol{b}^*{}_{(11)} = \left\{\frac{-\sin}{a\cos\quad\cos 2},\ \frac{\cos}{a\cos\quad\cos 2},\ 0\right\} \tag{5-6}$$

$$\boldsymbol{c}^*{}_{(11)} = \left\{\frac{-\sin}{\sqrt{2}c\cos\quad\sin\left(\frac{\pi}{4}+\ \right)},\ \frac{-\sin}{\sqrt{2}c\cos\quad\sin\left(\frac{\pi}{4}+\ \right)},\ \frac{1}{c}\right\}$$

(2) Monoclinic domain M_{12}

Figure 5.7(b) and (e) show the monoclinic domain M_{12}. The polarization vector rotates in the (011) mirror plane. Thus, $\boldsymbol{a}$ is relative to changes of the length Δc and the vectors, $\boldsymbol{b}$ and $\boldsymbol{c}$, rotate by angles $\Delta\quad(\Delta\ )$, respectively. According to this model, the orientation matrix of the direct lattice vectors with respect to the domain M_{12} can be calculated by,

$$\left[U_A^{(12)}\right] = \begin{pmatrix} c & a\ \sin & a\ \sin \\ 0 & a\ \cos\quad\cos & a\ \cos\quad\sin \\ 0 & a\ \cos\quad\sin & a\ \cos\quad\cos \end{pmatrix} \tag{5-7}$$

The reciprocal lattice vectors of the domain M_{12} are consequently,

$$\boldsymbol{a}^*_{(12)} = \left\{\frac{1}{c},\ \frac{-\sin}{\sqrt{2}c\cos\ \sin\left(\frac{\pi}{4}+\ \right)},\ \frac{-\sin}{\sqrt{2}c\cos\ \sin\left(\frac{\pi}{4}+\ \right)}\right\}$$

$$\boldsymbol{b}^*_{(12)} = \left\{0,\ \frac{\cos}{a\cos\ \cos 2},\ \frac{-\sin}{a\cos\ \cos 2}\right\} \tag{5-8}$$

$$\boldsymbol{c}^*_{(12)} = \left\{0,\ \frac{-\sin}{a\cos\ \cos 2},\ \frac{\cos}{a\cos\ \cos 2}\right\}$$

(3) Monoclinic domain M_{13}

A model of the monoclinic domain M_{13} is shown in Figure 5.7(c) and (f). In this case, the polarization rotates in the (010) mirror plane, i.e. the vectors, $\boldsymbol{a}$ and $\boldsymbol{c}$, rotate by angles Δ (Δ) and the $\boldsymbol{b}$ is changed by the length Δc. In the same manner as the domains M_{11} and M_{12}, the orientation matrix of the direct lattice vectors with respect to the domain M_{13} is calculated as,

$$\left[U_A^{(13)}\right] = \begin{pmatrix} a\ \cos\ & \cos\ & 0 & a\ \cos\ & \sin\ \\ a\ \sin\ & & c & a\ \sin\ & \\ a\ \cos\ & \sin\ & 0 & a\ \cos\ & \cos\ \end{pmatrix} \tag{5-9}$$

Their reciprocal lattice vectors are accordingly obtained by,

$$\boldsymbol{a}^*_{(13)} = \left\{\frac{\cos}{a\cos\ \cos 2},\ 0,\ \frac{-\sin}{a\cos\ \cos 2}\right\}$$

$$\boldsymbol{b}^*_{(13)} = \left\{\frac{-\sin}{\sqrt{2}c\cos\ \sin\left(\frac{\pi}{4}+\ \right)},\ \frac{1}{c},\ \frac{-\sin}{\sqrt{2}c\cos\ \sin\left(\frac{\pi}{4}+\ \right)}\right\} \tag{5-10}$$

$$\boldsymbol{c}^*_{(13)} = \left\{\frac{-\sin}{a\cos\ \cos 2},\ 0,\ \frac{\cos}{a\cos\ \cos 2}\right\}$$

The measured reciprocal space maps on {004} reflection involve only $\boldsymbol{c}^*$ with respect to the monoclinic domains, M_{11}, M_{12}, and M_{13}. Therefore, the reciprocal space vectors around the $= [004]^*$ position for the three domains can be written by the following coordinates,

$$\begin{matrix}(11)\\004\end{matrix} = 4\left\{\frac{-\tan\ _1}{\sqrt{2}c_1\ \sin\left(\frac{\pi}{4}+\ _1\right)},\ \frac{-\tan\ _1}{\sqrt{2}c_1\ \sin\left(\frac{\pi}{4}+\ _1\right)},\ \frac{1}{c_1}\right\} \quad (5\text{-}11)$$

$$\begin{matrix}(12)\\040\end{matrix} = 4\left\{0,\ \frac{-\sin\ _2}{a_2\cos\ _2\cos 2\ _2},\ \frac{\cos\ _2}{a_2\cos\ _2\cos 2\ _2}\right\} \quad (5\text{-}12)$$

$$\begin{matrix}(13)\\400\end{matrix} = 4\left\{\frac{-\sin\ _2}{a\cos\ _2\cos 2\ _2},\ 0,\ \frac{\cos\ _2}{a\cos\ _2\cos 2\ _2}\right\} \quad (5\text{-}13)$$

Since the observed maps (refer to Figure 5.4(a)) were transformed into the coordinate system XY, where the X-axis is parallel to ($\boldsymbol{a}^*$+$\boldsymbol{b}^*$) and the Y-axis is parallel to $\boldsymbol{c}^*$, the coordinates of the reciprocal space vectors are calculated as follows,

$$\begin{matrix}(11)\\004\end{matrix} = 4\left\{\frac{-\tan\ _1}{c_1\ \sin\left(\frac{\pi}{4}+\ _1\right)},\ \frac{1}{c_1},\ 0\right\}_{XYZ} \quad (5\text{-}14)$$

$$\begin{matrix}(12)\\040\end{matrix} = 4\left\{\frac{-\sin\ _2}{\sqrt{2}a_2\cos\ _2\cos 2\ _2},\ \frac{\cos\ _2}{a_2\cos\ _2\cos 2\ _2},\ \frac{-\sin\ _2}{\sqrt{2}a_2\cos\ _2\cos 2\ _2}\right\}_{XYZ} \quad (5\text{-}15)$$

$$\begin{matrix}(13)\\400\end{matrix} = 4\left\{\frac{-\sin\ _2}{\sqrt{2}a_2\cos\ _2\cos 2\ _2},\ \frac{\cos\ _2}{a_2\cos\ _2\cos 2\ _2},\ \frac{-\sin\ _2}{\sqrt{2}a_2\cos\ _2\cos 2\ _2}\right\}_{XYZ} \quad (5\text{-}16)$$

The coordinates of the reciprocal space vectors for the other 9 monoclinic domains, which originate from the rhombohedral domains R_2, R_3, and R_4, can be derived similarly. Figure 5.8 accordingly shows a schematic diagram corresponding to the positions of the Bragg peaks from all possible 12 monoclinic domains (refer to an animation in Video D.4 of Appendix D), where the notations are introduced as follows,

$$X_1 = \frac{4\tan\ _1}{c_1\ \sin\left(\frac{\pi}{4}+\ _1\right)},\quad Y_1 = \frac{4}{c_1} \quad (5\text{-}17)$$

$$X_2 = \frac{4\sin\ _2}{\sqrt{2}a_2\cos\ _2\cos 2\ _2},\quad Y_2 = \frac{4\cos\ _2}{a_2\cos\ _2\cos 2\ _2} \quad (5\text{-}18)$$

All of the derived 12 monoclinic domains are finally calculated and are listed in the following table.

R_n-domain, polarization direction	M_{mn}-domain, polarization rotation	Bragg peak position XY
R_1, [111]	M_{11}, [111] → [001]	$\{-X_1, Y_1\}$
	M_{12}, [111] ← [100]	$\{-X_2, Y_2\}$
	M_{13}, [111] ← [010]	$\{-X_2, Y_2\}$
R_2, [−111]	M_{21}, [−111] → [001]	$\{0, Y_1\}$
	M_{22}, [−111] ← [−100]	$\{-X_2, Y_2\}$
	M_{23}, [−111] ← [010]	$\{X_2, Y_2\}$
R_3, [−1−11]	M_{31}, [−1−11] → [001]	$\{X_1, Y_1\}$
	M_{32}, [−1−11] ← [−100]	$\{X_2, Y_2\}$
	M_{33}, [−1−11] ← [0−10]	$\{X_2, Y_2\}$
R_4, [1−11]	M_{41}, [1−11] → [001]	$\{0, Y_1\}$
	M_{42}, [1−11] ← [100]	$\{-X_2, Y_2\}$
	M_{43}, [1−11] ← [0−10]	$\{X_2, Y_2\}$

The peak separation along the X-axis direction under the applied electric field appears to be significantly smaller than the contribution from the crystal mosaicity, i.e. the separation can be regarded as the field dependence of the corresponding peak broadening. Using the peak positions in Figure 5.8, the peak width can be evaluated with respect to the monoclinic distortion parameters. This peak width is directly derived from the experimental data.

The width of both 004 and 400 peak components are accordingly obtained by,

$$W_{004} = \frac{4\ tan\ _1}{c_1\ sin\left(\frac{\pi}{4} +\ _1\right)} + W_{004}^{(0)}, \quad W_{400} = \frac{4\sqrt{2}\ sin\ _2}{a_2\ cos\ _2\ cos\ 2\ _2} + W_{400}^{(0)} \tag{5-19}$$

where $W_{004}^{(0)}$ and $W_{400}^{(0)}$ are field-independent mosaicity parameters.

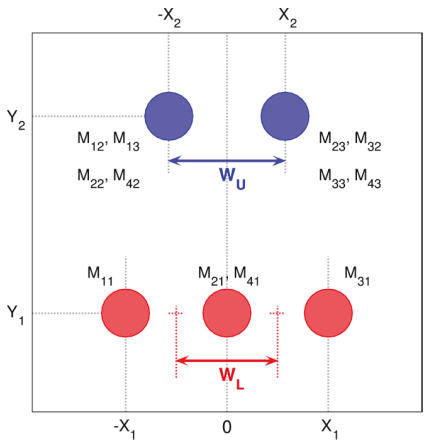

Figure 5.8 A sketch of the peak positions in the {004} group reflections regarding the 12 monoclinic domains. The positions of all possible peaks are described by four independent parameters X_1, Y_1, X_2, and Y_2. They are directly connected to the monoclinic distortion parameters, Δc_1, $\Delta\ _1$, Δa_2, $\Delta\ _2$ described by Equations (5-17) and (5-18) in the text.

If the monoclinic distortion angles are sufficiently small, all the trigonometric functions can be replaced by the corresponding first-order Taylor expansion. Thus, the peak shape parameters are,

$$\Delta P_{004} = -\frac{4}{c_1}\frac{\Delta c_1}{c_1}, \quad \Delta P_{400} = -\frac{4}{a_2}\frac{\Delta a_2}{a_2} \tag{5-20}$$

$$\Delta W_{004} = \frac{4\sqrt{2}}{c_1}\Delta_{\ 1}, \quad \Delta W_{400} = \frac{4\sqrt{2}}{a_2}\Delta_{\ 2} \tag{5-21}$$

These equations can be used to extract the monoclinic distortions Δc_1 and $\Delta_{\ 1}$ for the domains M_{n1} and monoclinic distortion parameters Δa_2 and $\Delta_{\ 2}$ in the domains M_{n2} and M_{n3}.

5.4.3. Calculation of piezoelectric coefficients

This section evaluates the intrinsic piezoelectric coefficients by the following equation:

$$\boldsymbol{d}_{kij} = \frac{\partial \boldsymbol{x}_{ij}}{\partial \boldsymbol{E}_k}(\boldsymbol{E} = 0) \tag{5-22}$$

Here, $\boldsymbol{x}_{ij}$ and $\boldsymbol{E}_k$ are the components of the strain tensor and the electric field vector relative to the crystal physical Cartesian coordinate system [57]. The strain tensor can be described by the difference between the parent pseudo-cubic and the distorted monoclinic phases. The axes of the Cartesian coordinate system are aligned with respect to the basis vectors of the parent cubic phase (refer to Figure 5.6(a)). In this coordinate system, the strain tensor for the monoclinic distortion is given by,

$$\boldsymbol{x}_{ij} = \begin{pmatrix} \frac{\Delta a}{a} & \Delta & \frac{\Delta}{2} \\ \Delta & \frac{\Delta a}{a} & \frac{\Delta}{2} \\ \frac{\Delta}{2} & \frac{\Delta}{2} & \frac{\Delta c}{c} \end{pmatrix} \tag{5-23}$$

The piezoelectric coefficients $\boldsymbol{d}_{3jk}$ describe the strain in response to the applied electric field along the crystallographic *c*-axis, meaning that the orientation of electric field is realized in the domains M_{n1}. Therefore, the field dependence of the monoclinic

distortion parameters Δc_1 and $\Delta\ _1$ in the domains M_{n1} provides access to the piezoelectric coefficients d_{333} and d_{323}. Similarly, the piezoelectric coefficients $\boldsymbol{d}_{1jk} = \boldsymbol{d}_{2jk}$ represent the strain in response to the applied electric field along the *a*- or *b*-axis. These orientations are realized in the domains M_{n2} and M_{n3} respectively. Thus, the field dependence of the monoclinic distortion parameters $\Delta\ _2$ and Δa_2 in the domains M_{n2} and M_{n3} provides access to the piezoelectric coefficients d_{112} and d_{111} respectively. Thus, the intrinsic piezoelectric coefficients can be calculated by the following equations.

$$d_{333} = \frac{1}{c_1}\frac{\partial \Delta c_1}{\partial E}, \quad d_{323} = \frac{1}{2}\frac{\partial \Delta\ _1}{\partial E}, \quad d_{112} = \frac{\partial \Delta\ _2}{\partial E}, \quad d_{111} = \frac{1}{a_2}\frac{\partial \Delta a_2}{\partial E} \tag{5-24}$$

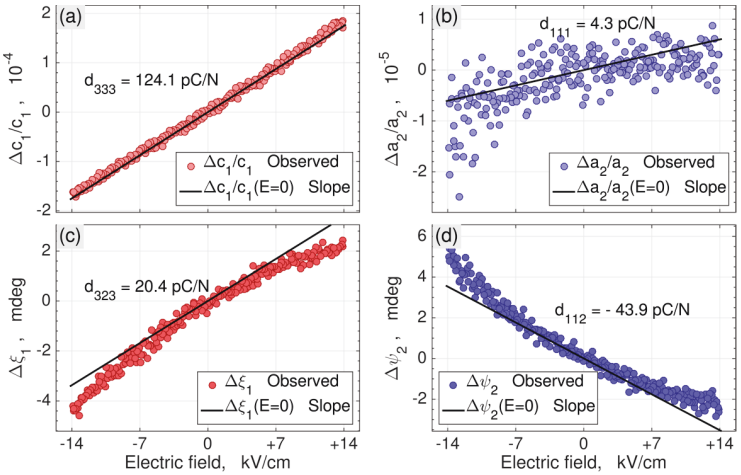

Figure 5.9 Electric field dependence of the lattice parameters and the intrinsic piezoelectric coefficients, d_{333}, d_{111}, d_{323}, and d_{112}, respectively. The coefficients are evaluated by Equation (5-22) at an electric field $\boldsymbol{E} = 0$.

Figure 5.9 shows the results of the monoclinic distortion parameters in domains M_{n1}, M_{n2} and M_{n3}, and indicates the obtained numerical values of the corresponding piezoelectric coefficients, which are d_{333} = 124.1 pC/N; d_{323} = 20.4 pC/N; d_{112} = −43.9 pC/N; d_{111} = 4.3 pC/N.

5.4.4. Polarization rotation and non-linear response under an electric field

According to Equations (5-20) and (5-21), the monoclinic distortion parameters Δ_1, Δ_2 and Δa_2 have the same field dependences as the peak-shape parameters W_{004}, W_{400} and P_{400}. Considering the observed peak-shape parameters (see Figure 5.5), the monoclinic distortion is essentially non-linear with respect to the applied electric field strengths. Here, it is interesting to note that whether this non-linearity may be affected by the polarization rotation. One can be proposed that the monoclinic strains are linear with respect to the polarization rotation angle ρ, rather than to the magnitude of the electric field E, so that $\Delta_1 = F_\xi \Delta\rho_1$, $\Delta_2 = F_\psi \Delta\rho_2$, and $\Delta a_2 = F_a \Delta\rho_2$. To derive the $\rho(E)$ dependence, one can be assumed that the free energy ΔG [59] has a quadratic dependence on ρ with the minimum at $\rho = 0$, so that:

$$\Delta G = G_0 \rho^2 - EP\cos\chi \tag{5-25}$$

where G_0 is the energy expansion coefficient, P is the length of the polarization vector and χ is the angle between polarization and electric field directions, as shown in Figure 5.6(a). Hereby, the χ angle with respect to the domains can be written by the polarization rotation angle as follows,

$$\cos\chi_1 = \cos(\rho - \rho_{\ }) \tag{5-26}$$

$$\cos\chi_2 = \cos\chi_2 = \frac{1}{\sqrt{2}}\sin(\rho_{\ } - \rho) \tag{5-27}$$

where $\rho_{\ } = \cos^{-1}\frac{1}{\sqrt{3}} \approx 54.57°$ is the angle between the cube edges and the body diagonal.

When Equations (5-26) and (5-27) are substituted into Equation (5-25) and the global minimum is found by $\frac{\partial \Delta G}{\partial} = 0$, the polarization rotation angles $\Delta\rho$ in the domains M_{n1} and M_{n2}/M_{n3} are obtained by,

$$\Delta\rho_1 = -WE\sin(\Delta\rho_1 - \rho\ ) \tag{5-28}$$

$$\Delta\rho_2 = -\frac{WE}{\sqrt{2}}\cos(\rho\ - \Delta\rho_1) \tag{5-29}$$

with $W = \frac{G_0}{2P}$. Suggested that the change of the monoclinic distortion parameters is linear with respect to the polarization rotation, Equations (5-28) and (5-29) can be rewritten by,

$$\Delta_{\ 1} = -WEF_\xi \sin\left(\frac{\Delta_{\ 1}}{F_\xi} - \rho\ \right) \tag{5-30}$$

$$\Delta_{\ 2} = -\frac{WEF_\psi}{\sqrt{2}}\cos\left(\rho\ - \frac{\Delta_{\ 2}}{F_\psi}\right) \tag{5-31}$$

$$\Delta a_2 = -\frac{WEF_a}{\sqrt{2}}\cos\left(\rho\ - \frac{\Delta a_2}{F_a}\right) \tag{5-32}$$

Equations (5-30) – (5-32) can be solved numerically as a function of the applied electric field E, so that the unknown model parameters W, F_ξ, F_ψ, and F_a can be found as the best fit values. The results are shown in Figures 5.10(a–c), where both observed and simulated (according to Equations (5-30) – (5-32)) monoclinic distortion parameters: $\Delta_{\ 1}$, $\Delta_{\ 2}$, and Δa_2 are displayed. These figures show that the simplified model is surprisingly efficient in accounting for the non-linear dependence of all three non-linear monoclinic distortion parameters. Figure 5.10(d), however, represents the $\Delta\rho_1 = \frac{1}{F_\xi}\Delta_{\ 1}$, $\Delta\rho_2 = \frac{1}{F_\psi}\Delta_{\ 2}$ polarization rotations angles, showing that this non-linearity implies that the polarization rotation angle is larger than 35°.

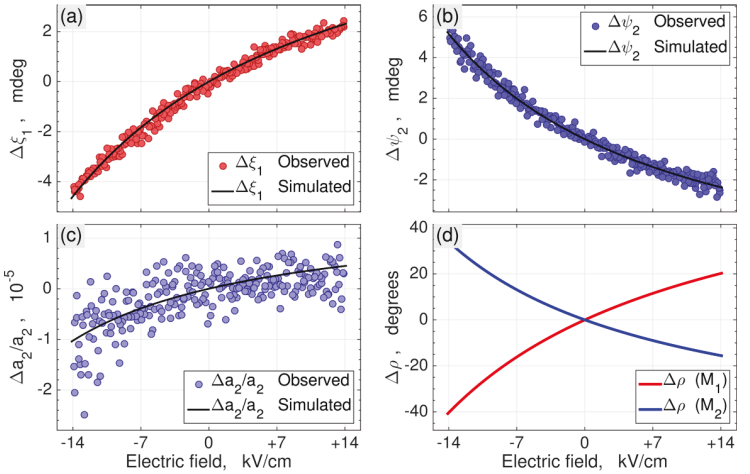

Figure 5.10 Electric field dependence of the strain parameters and polarization rotation angle. (a–c) Comparison between the observed change of Δ_1, Δ_2, and Δa_2 monoclinic strain parameters (circles) and the calculated change (lines) according to Equations (5-20) and (5-21). (d) Polarization rotation angle ρ as a function of external electric field in the domains M_{n1} and M_{n2}/M_{n3}.

This good agreement between observed and simulated monoclinic distortion parameters clearly supports the suggestion concerning the close connection between electric field-induced polarization rotation and lattice strain. In addition, this study demonstrates that the corresponding piezoelectric effects are clearly of intrinsic, rather than extrinsic, origin.

5.5. Conclusion

The macroscopic piezoelectric coefficients of NBT ceramics and single crystals are known to range between 20 ~ 100 pC/N [128,130–132]. Thus, the results of this study suggest that the electromechanical coupling in NBT is mainly an intrinsic origin. The intrinsic nature of the electromechanical coupling can be seen in the shifts of the angular positions for the {004} reflection families, as discussed in this study.

Furthermore, the results can be interpreted such that the enhanced electromechanical coupling is caused by polarization rotation. The field-induced non-linear response of the lattice parameters (as shown in Figures 5.9 and 5.10) can explain the appearance of the polarization rotation. However, it was assumed that the big changes of the polarization rotation angle represent 'soft-mode' structural changes, i.e. it shows large changes even for sub-coercive electric fields. Accordingly, this indicates the field-induced non-linear response of the lattice parameters.

Such preliminary knowledge about polarization rotation in ferroelectric perovskites supports the possibility of the following structural changes.

(1) The polarization rotation can be directly related to the displacement of **A** and **B** cations from the centers of the corresponding oxygen cages ($\mathbf{AO}_{12}$ and $\mathbf{BO}_6$). These could be measured from the 'integrated intensity' of the peaks and by implementing the structure factor formalism (see e.g. [20,24,102]). Indeed, the relative changes of the observed integrated intensity for both 400 and 004 Bragg peaks indicate ~10 % (see Figure C.2 in Appendix C). However, these changes can also be caused by the volume exchange between the M_{n1} and M_{n2}/M_{n3} domains. Measurements of addition Bragg reflections are necessary to account for the large number of free parameters in the *Cc* monoclinic structure and to understand them from the parameters of the microstructure.

(2) The large amount of polarization rotation may stem from the changes of the parameters in the local structure and short-range order. The structural disorder in NBT has been previously studied using diffuse X-ray scattering [133–135] or total neutron scattering [136]. The reverse Monte-Carlo simulation of the atomic pair-distribution function in NBT [136] demonstrated that the position of bismuth (Bi) atoms in the monoclinic {110} planes may differ from one unit cell to another and involve two co-existing directions of bismuth atom displacements. Here, this study may extend the ability of the bismuth atom to adopt two different polarization directions, and one can be assumed that the external electric field may easily switch the number of atoms populating one of the two states, thus such a switch can easily change the average direction of the polarization vector.

(3) The large amount of polarization rotation in NBT is very similar to that of the $Pb(Zr_{1-x}Ti_x)O_3$ (PZT) at the morphotropic phase boundary. Zhang et al. [73] reports that even a minor change of the ratio 'x' near the morphotropic phase boundary leads to the rotation of the average direction of Pb atom displacement by a large angle of over 35°. The easy polarization rotation is commonly considered to be one of the origins of enhanced piezo-activity.

These three types of the assumptions can also be considered as the origins of the enhanced electromechanical coupling in NBT even on application of the sub-coercive electric fields.

Finally, the demonstrated time-resolved reciprocal space mapping approach can be applied to other materials, and this innovative strategy has a high potential for exploring the origins of electromechanical coupling.

Chapter 6

Time-resolved X-ray diffraction study of a uniaxial $Sr_{0.5}Ba_{0.5}Nb_2O_6$ ferroelectric single crystal under an alternating electric field

This chapter studies a new mechanism of the piezoelectric activity appearing in a uniaxial ferroelectric single crystal in the form of correlation between lattice parameter and domain size using stroboscopic time-resolved X-ray diffraction on $Sr_{0.5}Ba_{0.5}Nb_2O_6$ single crystals under an alternating electric field.

6.1. Introduction

Strontium barium niobate ($Sr_xBa_{1-x}Nb_2O_6$ – SBN) is a very attractive material for technological applications and basic research, because of their electro-optic, photorefractive, pyroelectric, and piezoelectric properties. Thus, this material has been implemented in the fields of data storage systems and sensors [137–142]. SBN belongs to a tetragonal tungsten bronze structure, and its properties can be modified by a variation of the strontium/barium (Sr/Ba) ratio or by doping. On increasing the Sr/Ba ratio, SBN transforms from the conventional ferroelectrics to the relaxor ferroelectrics [143]. The single crystals SBN usually exists in composition the range $0.25 < x < 0.75$ [144]. It is known that SBN undergoes a phase transition (refer to Figure 2.8(b)) from a paraelectric phase with a *4mm* point group (space group *P4/mbm*) into a ferroelectric phase with a point group *4/mmm* (space group *P4bm*) through the *Curie temperature* (T_C) [145–147].

Figure 6.1 shows the crystal structure of SBN. The structure is based on the framework of NbO_6 octahedra. These are linked together and form three kinds of channels - tetragonal (**A1** site), pentagonal (**A2** site), and trigonal (**C** site). The **C** sites remain empty because they are too small to contain either Sr or Ba atoms. The intermediate **A1** sites are only occupied by Sr cations, but the largest **A2** sites can be filled by either Sr or Ba cations. The Nb atoms are located in the center of oxygen octahedra. Since one-sixth of all the **A** sites (**A1**+**A2** sites) are empty, SBN can be described as a natural defective material [148].

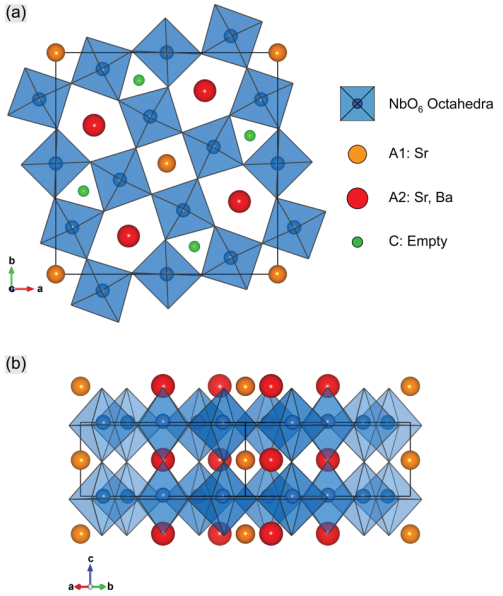

Figure 6.1 A schematic illustration of the tetragonal tungsten bronze structure, drawn using the VESTA package [89]. (a) The projection on the (001) plane of the strontium barium niobate unit cell in the crystallographic c-axis direction. The largest **A2** sites are occupied by Ba or Sr atoms, while the **A1** sites are occupied by Sr atoms. The smallest **C** cites are empty. (b) The projection on the (110) plane of the strontium barium niobate unit cell.

As discussed in Chapter 2, ferroelectrics macroscopically deform under an applied external electric field due to *converse piezoelectricity*. This functionality is one of the most important physical properties in ferroelectrics and may be caused by two possible driving mechanisms. One is an intrinsic piezoelectricity which evolves from atomic displacement and change of the bond lengths. The other arises from domain wall motion or other mesoscopic phenomena. A proper understanding of the enhanced electromechanical coupling can give significant keys for the development of new materials.

Many experiments have been devoted to observe all of the processes involving both the intrinsic and extrinsic mechanisms, but *in situ* experiments have been mostly focused on ceramics or powder samples. Besides, many research interests have been concentrated on the functionalities of the perovskite-based ferroelectrics, such as $Pb(Zr,Ti)O_3$ (PZT), where domains share both ferroelastic and ferroelectric features.

On the other hand, the piezoelectricity in uniaxial ferroelectrics is not yet understood fully. SBN is an interesting model system for the uniaxial ferroelectrics, which involves spontaneous polarization along the crystallographic c-axis only. The symmetry relationship between paraelectric (*4mm*) and ferroelectric (*4/mmm*) phases allows for only 180° ferroelectric domains, therefore the formation of ferroelastic domains (non-180° domains) is forbidden (refer to Figure 2.8).

For this reason, one of such conventional ferroelectrics in SBN, e.g. $Sr_{0.5}Ba_{0.5}Nb_2O_6$ (SBN50) single crystal was selected to study the nature of the relationship between ferroelectricity and piezoelectricity in uniaxial ferroelectrics under an alternating electric field. To do this, the stroboscopic time-resolved X-ray diffraction techniques were implemented.

6.2. Experiment: Time-resolved rocking curves under an alternating electric field

Measurements were performed at the P09 beamline of the PETRA III synchrotron facility (Hamburg, Germany) using a six-circle single crystal diffractometer and an avalanche photo diode (APD) detector. Figure 6.2 shows the experimental setup and the electronic systems used in this study. The X-ray wavelength was tuned to be λ = 0.86 Å to maximize the penetration depth depending the measured reflections geometry as $\langle t \rangle = \frac{1}{2} sin\theta$ = 10.3 ~ 23.3 μm. The investigated SBN50 single crystals were grown by the Czochralski technique [143]. The [001] oriented crystal plate was cut to 0.5 mm thickness and both surfaces of the plate were polished to optical quality. Gold thin electrodes (~100 nm) were deposited on both polished faces, and the prepared crystal was mounted on the sample holder with contacting copper wires (see Figure 6.2(d) and (e)).

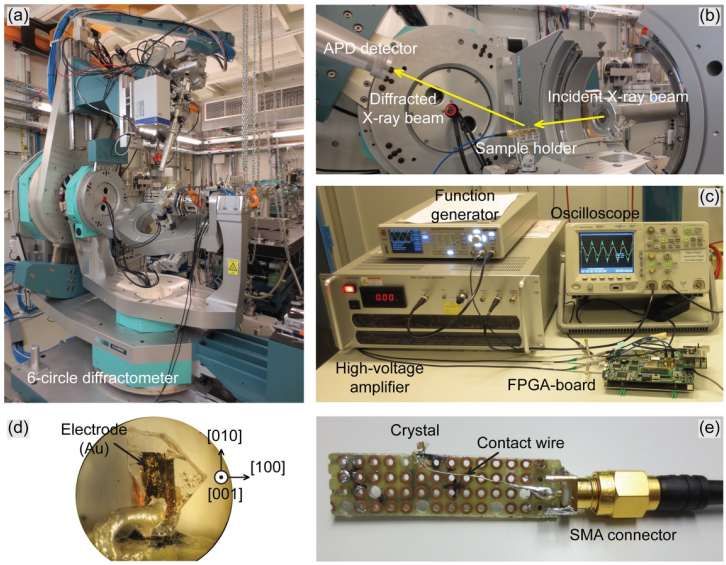

Figure 6.2 Photographs of the experimental setup at the P09 beamline of the PETRA III synchrotron facility. (a) Inside the hutch of the beamline with the 6-circle diffractometer. (b) The experimental geometry with a sample. (c) The electronic devices for applying the electric field and the data-acquisition system. (d) SBN50 single crystal with crystallographic axes. (e) The crystal is mounted on the sample holder and connected with the electrical wires for the application of electric fields.

An alternating electric field is applied to the sample using a combination of a function generator (HMF-2550, Hameg) and a high-voltage amplifier (AMT-3B20, Matsusada). The combined electronic system produced a 20 Hz periodic triangular shaped high-voltage signal with two different amplitudes: (1) ± 150 V [sub-coercive field of ± 3 kV/cm] and (2) ± 975 V [over-coercive field of ± 19.5 kV/cm], and the electrical output signals were measured using an oscilloscope (HMO-3004, Hameg). The electrical currents can be simultaneously measured during the diffraction experiment using the series circuit with the 1 kΩ resistor (see Figure 6.3(a)).

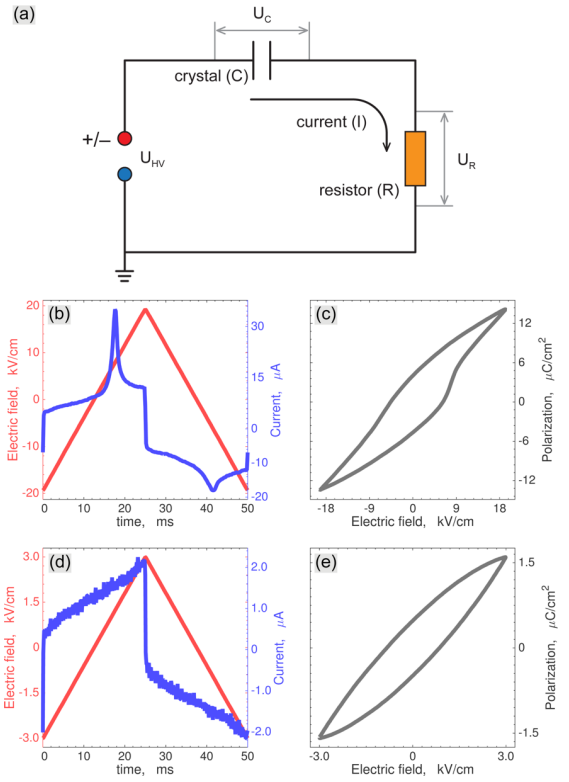

Figure 6.3 Dielectric responses of SBN50 crystal. (a) A schematic diagram of the series circuit which was used in the experiment in order to measure the dielectric responses. The resistance for the current active probe is 1 kΩ. (b, d) Time dependence of the electric field (red) and current (blue) for the case of over- and sub-coercive fields. (c, e) Polarization–Electric field loops for both cases, respectively.

The dielectric polarization $P(t)$ can be extracted from the measured electric current response $I(t)$. The integral of the current over the time duration T_1 to T_2 corresponding to a period of the applied electric field, yields the total amount of charge as a function of time,

$$Q(t) = \int_{T_1}^{T} I(t)\, dt \tag{6-1}$$

and the charge divided by the electrode area A, yields the polarization as a function of time,

$$P(t) = Q(t)/A \tag{6-2}$$

The Polarization is then plotted against the applied electric field $E(t)$ obtaining a hysteresis loop, as shown in Figure 6.3(c) and (e).

In order to study the structural dynamics of the SBN50 crystal, the rocking curves are stroboscopically collected during electric field cycling. As discussed in Chapter 3 (Section 3.3), the rocking curve is collected by rotating (rocking) a crystal within a small angular range (~0.1°) about the Bragg angle, while the intensity is measured using an open point detector (scintillating counter). The open detector means the intensity is integrated along the scattering angle within the range of 1°. The obtained rocking curve profiles are analyzed that the angular positions of the rocking curves depend on the lattice parameters and the crystal orientation, while the shapes account for their distribution throughout the sample. The change of the center of mass position of the rocking curve $\Delta\omega$, associated with the electric field-induced deformation and rotation of the crystal, can be described by the displacement of a reciprocal lattice vector from the Ewald sphere, as shown in Figure 6.4(a) (Graafsma [149], Gorfman et al. [21] and Schmidt et al. [150]). The $\Delta\omega$ is given by,

$$\Delta\omega \;=\; -tan\theta_B \cdot x_{ij} h_i h_j \; - x_{ij} h_i y_j + r_{ij} h_i y_j \tag{6-3}$$

where $\boldsymbol{x}$ is the strain tensor [57], θ_B is the Bragg angle. Here, $\boldsymbol{h}$ and $\boldsymbol{y} = [\boldsymbol{h},\ \ \boldsymbol{\omega}]$ are unit vectors, so that the $\boldsymbol{h}$ points towards the corresponding reciprocal lattice node and the $\boldsymbol{\omega}$ is along the diffractometer rotation axis. All the vectors and tensor components refer to the crystal physical Cartesian coordinate system.

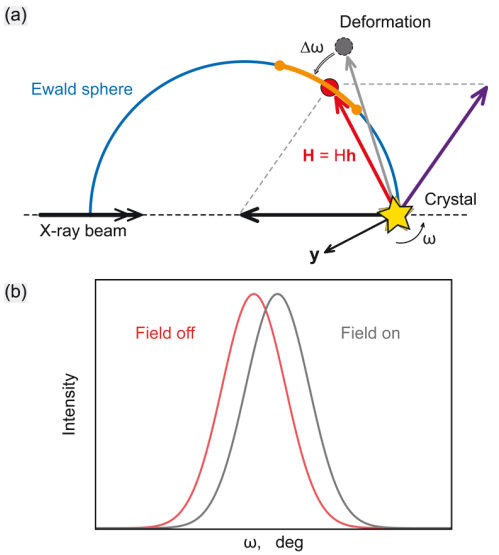

Figure 6.4 (a) A sketch for the reciprocal space reconstruction of a rocking curve displacement caused by a macroscopic deformation. A crystal is exactly oriented at the Bragg angle to a primary X-ray beam so that the corresponding reciprocal lattice vector intersects the Ewald sphere. (b) The displacement of the reciprocal lattice vector from the Ewald sphere is visible as an angular shift of the rocking curve.

The components of the strain $\boldsymbol{x}$ and rotation $\boldsymbol{r}$ tensors depend on the local deformation field $\boldsymbol{u}(\boldsymbol{r}, t)$ as follows,

$$x_{ij} = \frac{1}{2}\left(\frac{\partial u_i}{\partial r_j} + \frac{\partial u_j}{\partial r_i}\right), \qquad r_{ij} = \frac{1}{2}\left(\frac{\partial u_i}{\partial r_j} - \frac{\partial u_j}{\partial r_i}\right) \tag{6-4}$$

The second and the third terms of Equation (6-3) depend on the diffractometer angles and the orientation matrix of the crystal because of the y_j component. If the series of harmonic reflections (e.g. 00L) however are measured, the terms of the product $h_i y_j$ become constant [21,149,151,152], thus Equation (6-3) can be simplified by,

$$\Delta\omega = A \cdot tan\theta + B \tag{6-5}$$

where $A = -x_{ij}h_ih_j$ and B are constant. Therefore, the observed rocking curves for the series of 00L reflections can be used to calculate and evaluate the strain component $x_{33} = -A = -d_{33} \cdot E$, which involves the piezoelectric coefficients d_{33}.

6.3. A New mechanism of an enhanced piezoelectricity in uniaxial ferroelectrics under an applied over-coercive field

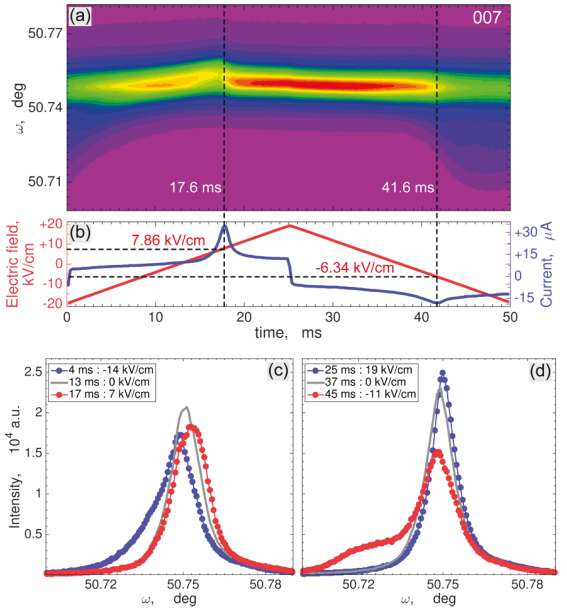

Figure 6.5 Dynamics of 007 rocking curves under over-coercive external electric fields. (a) Time-dependent X-ray diffraction intensity maps of the rocking curve for 007 Bragg reflections; the dashed lines show the switching times indicating the changes of peak position. (b) Time dependence of the applied electric fields (red) and the observed current signals (blue). (c, d) The selected six 007 rocking curves from the time-channels.

This section studies the dynamics of 007 rocking curve under an applied over-coercive field cycling. Figure 6.5(a) and (b) compare the time-dependent rocking curve profiles with the applied electric field and the measured current response. The figures indicate that the ferroelectric switching occurs at +7.86 kV/cm and −6.34 kV/cm for the rising and falling electric field, respectively. The switching current (blue line) and the P–E loop (refer to Figure 6.3(c)) show asymmetry, which is clearly indicated that these two polarization reversals may be driven by different mechanisms. Figure 6.5(c) and (d) show the selected six rocking curve profiles at different times/electric fields. The observed rocking curves also show asymmetry; Figure 6.5(c) shows the case of a rising electric field and Figure 6.5(d) is for a falling field. The rocking curve profiles clearly show that the peak is separated into two components; one is sharp and the other is broad. In general, the peak width can be contributed to by changes of the domain size or mosaicity. On the other hand, one can be considered that the broad components are based on the volume of smaller domains and the sharp components related to the large domains, because the mosaicity does not depend on the electric field.

The observed rocking curve profiles are analyzed to perform a fitting process using a sum of two symmetrical pseudo-Voigt functions. The pseudo-Voigt function is defined by,

$$f(x) = \eta \cdot f_L(x) + (1-\eta) \cdot f_G(x) \tag{6-6}$$

where $f_L(x)$ is the Lorentz-like and $f_G(x)$ is the Gauss-like function. Each function, $f_L(x)$ and $f_G(x)$, is defined as,

$$f_L(x) = \frac{2\sigma}{\pi} \cdot \frac{I}{4(x-x_0)^2 + \sigma^2} \tag{6-7}$$

$$f_G(x) = 2 \cdot \sqrt{\frac{ln2}{\pi}} \cdot \frac{I}{\sigma} \cdot exp\left\{-4 \cdot \left(\frac{x-x_0}{\sigma}\right)^2 \cdot ln2\right\} \tag{6-8}$$

where x_0 is the center of mass of the pseudo-Voigt function, σ is the full width at half maximum and I is the integrated intensity of the profile. The parameter η can be used to control the peak shape.

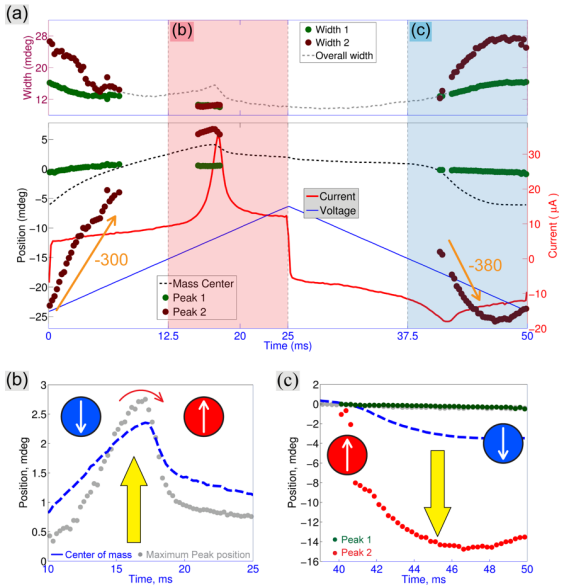

Figure 6.6 (a) The dynamics of peak position and width for both two peak components from the 007 rocking curves: Brown (Green) dots correspond to the weaker (dominating) components; it is also shown the center of mass of peak positions (P_{CM}) and the applied voltage and electrical current signal for reference. (b, c) Two different routes of the polarity switching for the positive reversal interval (red box) and for the negative reversal interval (blue box).

The fitting results regarding the dynamics of the center of mass position and width of the rocking curves as a function of time are shown in Figure 6.6(a). The representative rocking curves and all time-resolved data with the fitted parameters are available in Appendix E. The part for which it was not possible to separate by fitting is filled with the overall calculated values regarding the center of mass (black dashed line) and peak width (grey dashed line) from the observed rocking curves. It is interesting to note that the sharp peak component (green dots) is confined during all the time period but the broad peak component (brown/red dots) rapidly moves towards lower angles during one of the reversal intervals (for the negative electric field case). This indicates a strong mechanical strain, which means the broad peak component (brown/red dots) has very high piezoelectric coefficients. Two time intervals (marked by the orange arrows) in

Figure 6.6(a) show the largest shift of the broad peak (Peak 2). Thus, the corresponding piezoelectric coefficient $|d_{33}|$ of the 'Peak 2' component can be estimated/evaluated by Equation (6-5) during a linear response. The values are equal to (300 ± 100) pC/N (left arrow) and (380 ± 20) pC/N (right arrow). This feature was also observed in other reflections [98]. This strong piezoelectric activity is comparable with that of the $Pb(Zr,Ti)O_3$ (PZT) material.

According to the asymmetric feature of the switching current, marked as blue and read boxes in Figure 6.6(a), the results interpret as two different polarization reversal switching processes as shown in Figure 6.6(b) and (c) respectively.

(1) *Route 1*: In Figure 6.5(c) and Figure 6.6(b), the 'Peak 2' position has a kink during a positive switching (~17.6 ms). This peak must represent the volumes of two components which undergo switching, while the rest are frozen. The peak widths of both peak components remain constant during this switching, which means that the polarization reverts without nucleation of small domains such as from $\boldsymbol{P} \uparrow\downarrow \boldsymbol{c}$ (blue) to $\boldsymbol{P} \uparrow\uparrow \boldsymbol{c}$ (red). Besides, almost a single domain state is generated at the highest positive field because the rocking curve becomes the sharpest. Through the considerations, this scenario is consistent with the electrostriction law: $x_{33}(E) = Q_d P_d^2(E)$, where Q_d and P_d is the electrostriction coefficient and the single domain polarization, respectively.

(2) *Route 2*: Figure 6.6(c) shows the features of the 'nucleation of small inversion domains'. The broad peak component rapidly moves towards lower Bragg angles, and the peak width for both sharp and broad peaks is increased. This means that the averaged c-lattice parameter for the smaller domain volumes is elongated over the maximum strain value. In this case, the switching is not completed because the single domain state of the negative polarization (as with the positive case) is not reached, e.g. from $\boldsymbol{P} \uparrow\uparrow \boldsymbol{c}$ to $\boldsymbol{P} \uparrow\downarrow \boldsymbol{c}$. This second route exhibits a dramatic enhancement of the piezoelectric activity caused by the correlation between the domain sizes and their lattice parameters.

These two switching processes show different strain-field phenomena. The color maps in Figure 6.7 indicate regions of different polarization: $\boldsymbol{P} \uparrow\uparrow \boldsymbol{c}$ (red) and $\boldsymbol{P} \uparrow\downarrow \boldsymbol{c}$ (blue), the white is for P = 0. The 'Route 1' indicates that the switching passing over the 'neck', i.e. the strain is following the minimum, follows under a rising electric field duration and the 'Route 2' case illustrates the switching due to the formation of small domains passing over the maximum of the strain value.

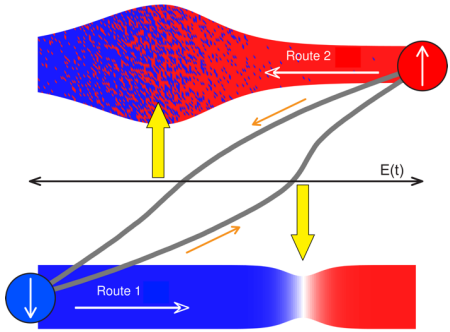

Figure 6.7 A schematic diagram of two polarization reversal routes. Each own color (red/blue) indicates the single domain states. The yellow arrows mark the switching intervals. (1) ROUTE 1 – Polarization reversal which indicates the strain follows the minimum, (2) ROUTE 2 – Nucleation and growth of small inversion domains, so that the strain has the maximum.

In fact, the enhanced piezoelectricity in the perovskite-based materials (e.g. PZT) is usually related to other mechanisms, so that the paraelectric-to-ferroelectric phase transition may occur in strain and polarization domains or due to the polarization rotation effects. These mechanisms are not allowed in SBN50 uniaxial ferroelectrics because both phases have the tetragonal symmetry. For this reason, this study can conclude that the enhanced piezoelectric activity of the uniaxial ferroelectrics is connected to the dynamics of the nucleated small domains.

6.4. Nonlinear response of uniaxial ferroelectrics under sub-coercive fields

This section discusses the dynamics of 007 rocking curves under applied sub-coercive electric fields. Many researches have attributed the measured nonlinearity of the piezoelectric response with respect to the non-180° domain walls, but this study describes how the observed nonlinear piezoelectric response can also be contributed to by the dynamics of 180° domains.

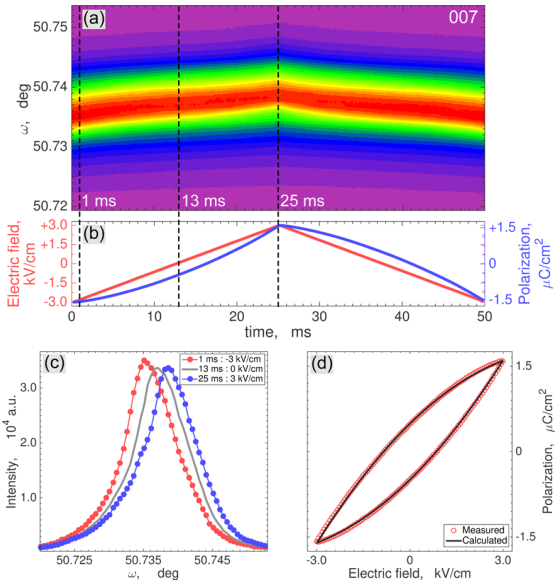

Figure 6.8 Time-resolved X-ray diffraction rocking curves of SBN50 under an alternating weak electric field (below coercive-field). (a) Intensity maps of 007 rocking curves as a function of time and electric field. (b) The applied electric field and the measured polarization profiles as a function of time. (c) The three selected rocking curve profiles. (d) The measured and calculated P–E loop under the applied sub-coercive electric field.

Figure 6.8 indicates the dynamics of 007 rocking curves under weak electric field cycling. Figure 6.8(a) plots the intensity maps as a function of time and the applied electric field. The observed rocking curves show asymmetry and change systematically (see Figure 6.8(c)). The systematic change of peak positions can be related to the field-induced macroscopic strain response in the crystal. It is interesting to note that the strain-field dependence shows non-linearity. Where does this non-linearity come from then?

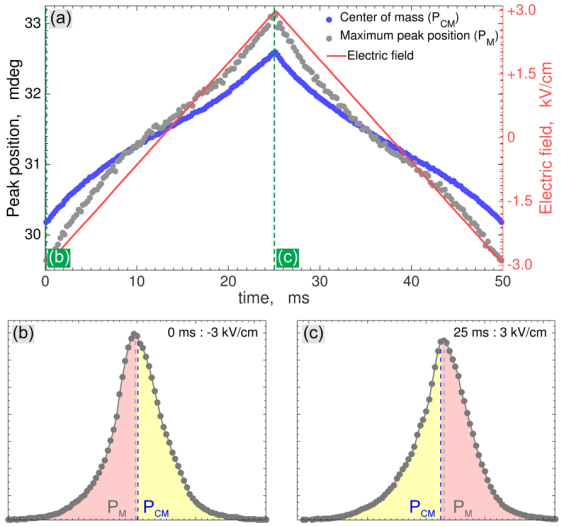

Figure 6.9 (a) Comparison between the center of mass (blue dots) and the maximum peak position (gray dots) of the 007 rocking curves under sub-coercive electric fields. (b, c) Two selected rocking curve profiles: the systematic change of asymmetry can be related to two components moving against each other.

The question can be answered by starting to compare between the averaged peak position (center of mass) and the maximum peak position from the measured rocking curves (Figure 6.9(a)). Since the mean value is the first moment, the center of mass positon of the rocking curve can be calculated by,

$$\mu = \frac{\int f(\omega) \cdot \omega \, d\omega}{\int \omega \, d\omega} \tag{6-9}$$

The maximum peak positions are evaluated using a parabolic fit for the selected seven top points of the rocking curves.

The averaged peak positions are shifted to the low (high) angular positions with respect to the maximum peak positions at the positive (negative) electric field, respectively (refer to Figure 6.9(a–c)). Since the rocking curves change asymmetrically, it can be assumed that the rocking curve is the sum of two symmetrical components which can be considered as inversion domains. However, it is difficult to fully separate the rocking curve profiles into two peak components as a function of time/electric field because the rocking curves are too close to each other.

The asymmetric feature can be alternatively considered through a 3rd moment of the rocking curve such as a skewness coefficient; the m-th moment of a curve f(ω) is described by,

$$S^{(m)} = \int_{-\infty}^{\infty} f(\omega) \cdot (\omega - \mu)^m \, d\omega \tag{6-10}$$

where μ is the center of mass of the rocking curve.

Assumed that the rocking curve is the sum of two components which are moving in the opposite direction (see Figure 6.10(a)), the skewness of the peak can be approximated as follows,

$$S^{(3)} \approx 3 \cdot I_1 \cdot \left(S_1^{(2)}(\mu_1 - \mu) - S_2^{(2)}(\mu_2 - \mu) \right) \tag{6-11}$$

where μ_1 and μ_2 is the center of mass of each peak, respectively.

According to Equation (6-11) the skewness $S^{(3)}$ can plot as a function of the center of mass position. The center of mass position μ with respect to the applied electric field is non-linear (Figure 6.10(b)), but the skewness on the μ indicates linearity (Figure 6.10(c)). Therefore, both μ_1 and μ_2 have the linear functions with respect to the μ as follows,

$$\mu_1 = A_1 \cdot \mu + B_1 \quad , \quad \mu_2 = A_2 \cdot \mu + B_2 \tag{6-12}$$

where A_1, B_1, A_2, and B_2 are constants.

The results thus answer that the strain-field dependence in each for the individual 180° domains also show the non-linearity. Therefore, this study can conclude that the non-linearity of the field-induced strain at weak electric field stems from the dynamics of the inversion domains.

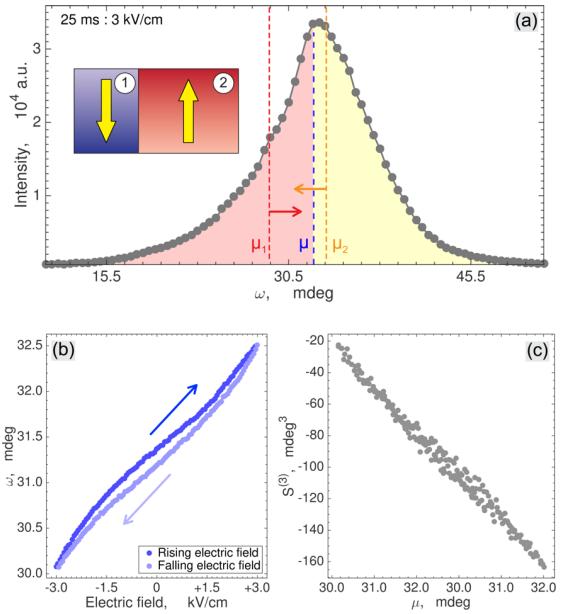

Figure 6.10 Asymmetry of 007 rocking curves on SBN50 crystal at weak electric fields. (a) A Schematic drawing for the dynamics of inversion domains moving in the opposite direction. (b) The center of mass position of the rocking curves as a function of the applied electric field: It is shown the non-linearity and clockwise strain–field hysteresis. (c) Skewness $S^{(3)}$ as a function of the center of mass position μ of the rocking curve: It is clearly shown the linearity.

Through the interpretation regarding the dynamics of 007 rocking curves, the observed P–E loop under the applied weak field (see Figure 6.8(b) and (d)) can be considered as the Rayleigh effect (*irreversible domain wall motion*). The Rayleigh law can be used to quantify the field dependence of the hysteretic and nonlinear phenomena with respect to the dielectric and piezoelectric coefficients. The polarization versus electric field hysteresis curve can be expressed as follows [153,154],

$$P(E) = (\varepsilon_{init} + \alpha_\varepsilon E_0) \cdot E \pm \frac{\alpha_\varepsilon}{2} \cdot (E_0^2 - E^2) \quad (6\text{-}13)$$

where E_0 is the amplitude of the driving field E, P is the polarization, ε_r $(= \varepsilon_{init} + \alpha_\varepsilon E_0)$ is the relative dielectric permittivity, ε_{init} is the reversible dielectric Rayleigh coefficient and α_ε is the irreversible Rayleigh coefficients for the dielectric properties. The plus sign (+) stands for a falling electric field and the minus sign (−) is for a rising field. The ε_{init} corresponds to the intrinsic lattice and reversible domain wall contributions to the permittivity and the term $\alpha_\varepsilon E_0$ is related to the irreversible displacement of the domain walls from one potential well to another [155]. Consequently, the contribution of the irreversible domain wall motion to the total dielectric permittivity can be obtained by the ratio of $\alpha_\varepsilon E_0/(\varepsilon_{init} + \alpha_\varepsilon E_0)$.

Figure 6.8(d) shows the polarization hysteresis loop where the E_0 = 3 kV/cm and frequency = 20 Hz. The red circles are the experimental data and the black line is the polarization calculated by Equation (6-13), which can be estimated the parameters; the reversible Rayleigh coefficient $\varepsilon_{init} \approx 20.5\ nF/m$ and the irreversible coefficient $\alpha_\varepsilon \approx 0.11\ nF/V$, respectively. It is inferred that ~38 % of the total measured permittivity is due to the irreversible domain wall motion at the E_0 = 3 kV/cm. Through it, the observed nonlinear polarization curve can be considered by the Rayleigh law at a weak electric field, which has a coefficient corresponding to the irreversible domain wall motion.

6.5. Conclusion

This chapter described a new insight into the relationship between the piezoelectricity and the polarization reversal in uniaxial ferroelectrics. Since the custom-built data-acquisition system has the advantage of the ability to track lattice parameters under an alternating electric field, it was able to evaluate the polarization reversal process via two different routes passing over the minimum or the maximum of the strain. The first route is dominated by the bulk polarization reversal process. The second route involves

the nucleation of small inversion domains and exhibits a dramatic enhanced piezoelectric activity originating from the correlation between the domain size and the lattice parameters. This study was also able to observe the dynamics of the inversion domains at weak electric fields, which clearly show the non-linearity of the field-induced strain.

These results show that the enhanced electromechanical couplings may arise from the mechanism which does not require any other ferroic ordering than the ferroelectric one. Thus, the possibility of activating this mechanism in other materials, and even under a weak electric field, will open a new way to design high performance piezoelectric materials.

Chapter 7

Time-resolved X-ray powder diffraction study of $BaTiO_3$-based ferroelectric ceramics: Polarization reversal and strain response under an alternating electric field

This chapter investigates the polarization-strain coupling properties in a $BaTiO_3$-based polycrystalline ferroelectric ceramic under an alternating electric field. The stroboscopic time-resolved high-energy X-ray powder diffraction technique (refer to Chapter 4) could help to obtain highly precise measurements of the lattice strain and the electric field-induced polarization reversal as measured the changes of the intensity with respect to Friedel pair due to the resonant scattering.

7.1. Introduction

It is well known that the enhanced electromechanical coupling and dielectric properties of ferroelectrics arise from the spontaneous polarization of their non-centrosymmetric crystal structures and the ability of switching between two or more polarization states under applied electric fields.

The relationship of the structure property with the polarization switching is known as more complex because of the several combined processes which involve several length and time scales. Such processes can be from both intrinsic and extrinsic mechanisms, the polarization rotation effects and the interaction with other neighbor-grains. Understanding of those effective factors can be the key points to develop new materials with the enhanced physical properties. However, existing experimental methods for investigating the dynamics of the polycrystalline ferroelectric ceramics lack the capability to simultaneously measure the multiple processes in a broad range of length and time scales.

An electric field-induced structural inversion in ferroelectrics can occur via different mechanisms. One can be a motion of domain wall separating 180° domains with an antiparallel spontaneous polarization each other. Moving 180° domain wall under an applied electric field can cause changes of volumetric ratios of oppositely polarized domains. The second one may follow intermediate steps such as 90° domain's

switching or/and ferroelastic phase transitions [45,156,157]. Moreover, there is additional mechanism, related to the transformation between ordered and disordered states in relaxor ferroelectrics [158–161]. These complex mechanisms may be suppressed in a favor of an entirely homogeneous switching, if a strong and rapidly changing electric field is applied [162].

Understanding these four mechanisms of the polarization reversal through experiments still remains challenging, and the lack of knowledge regarding the accurate polarization reversal processes can restrict a new design of preferential ferroelectrics. For this reason, it is essential to simultaneously explore both the polarization and lattice response of the bulk ferroelectrics during domain switching because the bulk material can provide an advantage to study the structure-property relationship regarding the complex electromechanical coupling mechanisms in a broad range. Since the high-energy X-ray beam can penetrate from μm to mm into the bulk material and can provide detailed bulk structural information, it can help to investigate their mechanisms. For example, both 90° domain wall motion and lattice strain can be quantified *in situ* from the intensity ratio and angular position changes of Bragg reflections [37,38,40,45,156,163,164]. Moreover, the displacements of atoms within the unit cell can be observed through the intensity variations of Bragg reflections, which can be analyzed by the structure factor from single crystals under applied electric fields [20,23,24,165].

A powerful X-ray diffraction, which is not fully verified yet, is its sensitivity to the structural inversion arising from the resonant (anomalous) scattering. Friedel's law states that the intensities of the hkl and $-h-k-l$ reflections, which are called a Friedel pair [166], are equivalent: [167]

$$|F_{\ kl}|^2 = |F_{-\ -k-l}|^2 \tag{7-1}$$

where $F_{\ kl}$ and $F_{-\ -k-l}$ are the structure factor. The diffracted intensity is proportional to the square of the structure factor.

This is true either if the crystal structure is centrosymmetric or if no resonant scattering is present (Figure 7.1(a)). However, Fridel's law is broken in the case of resonant scattering (Figure 7.1(b) and (c)). Anomalous dispersion cannot be neglected and cause a phase difference, which is related to the f'' term of the atomic scattering factors. Accordingly, the intensities of Friedel pair reflections become different. Therefore, the resonant X-ray scattering method can be used to study the structural

inversion in ferroelectrics because the structural inversion with respect to the polarization reversal can be observed from the intensity variations.

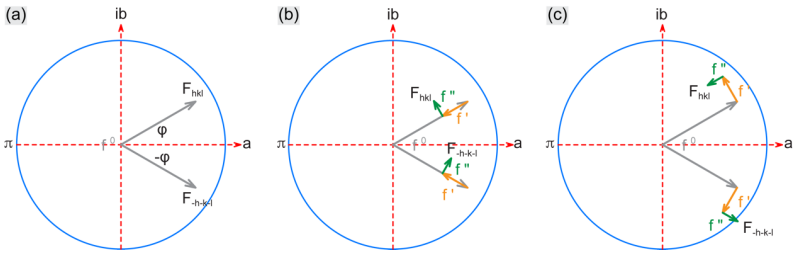

Figure 7.1 A schematic illustration of breaking Friedel's law. (a) Friedel's law [167] is fulfilled in the absence of the anomalous dispersion. (b, c) If the atoms are scattered anomalously, the phase relationship or/and the amplitude are broken.

The experimental observation of the Freidel pair contrast is however a bit challenging and requires precise measurement of the reflection intensities, because the Friedel pair contrast is small. For this reason, the method has been applied so far at single crystals [168] and epitaxial thin films [169,170]. Although the measurement of the Friedel pair in single crystals give some benefits, there are many factors (i.e. absorption, extinction and multiple scattering factors) which can restrict the precision for successful measurements [168–171].

On the other hand, both extinction and multiple scattering effects are absent in the case of the powder diffraction because typical powder grain sizes are below the critical length of dynamical scattering. However, measurement of such Friedel pair contrast using powder diffraction has never been considered, in spite of the fact that the crystallographic structure of their powder grains can be actively inverted by an application of external electric field in the same manner as single crystals.

$BaTiO_3$-based ferroelectric ceramics are one of interesting systems, so that a separation of multiple mechanisms for the polarization reversal process is a particular challenge [172]. For this reason, the tetragonal $0.94BaTiO_3$-$0.06BiZn_{0.5}Ti_{0.5}O_3$ (BT-BZT) perovskite-based ferroelectric ceramics are selected. Since the bulk information can be an important key for studying the multi-scale phenomena, a high-energy X-ray beam

(30 keV) was used for this experiment, which enables significant penetration depths into the bulk ceramic material. The data were simultaneously observed the polarization-field hysteresis loops and the {111} powder Bragg reflection. Therefore, the observing results can give crucial evidences for the polarization reversal phenomena. Moreover, based on the measured data a model corresponding displacement of atoms in the unit cell is suggested.

7.2. Experiments

The ceramic samples of composition $0.94BaTiO_3$-$0.06BiZn_{0.5}Ti_{0.5}O_3$ (BT-BZT) were prepared using a conventional solid states reaction method [172]. The dimension of the sample is 1.10 mm (between the electrodes) × 1.23 mm (along the incident X-ray beam) × 8.60 mm (length; perpendicular to the beam). On both surfaces the electrodes were painted using silver paste.

The measurements were performed at the ID22 beamline of the European Synchrotron Radiation Facility (Grenoble, France) with the energy 30 keV (λ = 0.3998 Å) [103]. The scattering angle of the (111) Bragg reflection was 2θ = 9.9°. The ID22 beamline provides a multi-analyzer crystal detector system, thus the strain can be measured because of the high angular resolution of 0.003°. An avalanche photo diode (APD) detector was used, which possesses the sensitivity and dynamic range necessary to measure the small intensity changes.

The sample was mounted on the specially designed sample holder (see Figure B.2 in Appendix B) in which the electric field was applied perpendicular to the incident X-ray beam. The experimental setup was shown in more detail in Figure 4.4 (Chapter 4). Figure 7.2(a) shows a schematic view of the mounted sample and represents the angle (θ = 4.95°) between the applied electric field direction and the scattering vector. Since the the linear attenuation coefficient of the used wavelength is 40 cm^{-1}, about 0.73 % of the beam is transmitted through the sample. In this experiment, the diffraction profiles regarding the individual {111} grains are measured, so that the scattering vector is almost parallel to the direction of the applied electric field (Figure 7.2(a)). If the elastic interactions from neighbor grains are absent, only 180° domain wall motion can be expected in these grains (refer to Figure 7.2(b)).

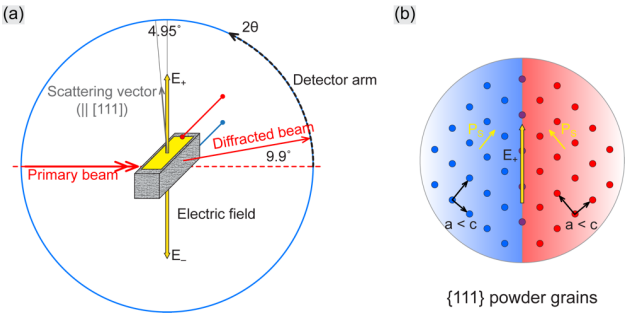

Figure 7.2 (a) A sketch of experimental geometry: the diffraction from {111} oriented powder grains. Here, the electric field is applied vertically and aligned at the θ = 4.95° to the [111] direction of the scattering vector. (b) Two-dimensional schematic drawing of the {111} powder grains; the spontaneous polarization (P_S) is align along the crystallographic c-axis.

The cyclic bipolar electric fields with 50 Hz repetition rates are applied to the sample using both a function generator (HMF-2550, Hameg) and a high voltage amplifier (AMT-3B20, Matsusada). Each cycle of the applied electric fields is generated as PUND (positive-up negative-down) type, which has a pair of positive and negative pulses (each pulse is 2 ms long) with the maximum amplitude of ±27 kV/cm. Such double-pulse waveforms provide that the first pulse can probe the ferroelectric switching and the second pulse probes the purely dielectric response. The time-resolved X-ray diffraction data were acquired using a custom-built stroboscopic multi-channel analyzer data-acquisition system down to the nanosecond time scale, which is described in more detail in Chapter 4. In this experiment, the implemented system provides 10000 time-channels with 2 μs resolution. In order to improve the counting statistics at a temporal resolution (i.e. time-bin size) of 40 μs, each 20 neighboring channels were binned finally. The diffraction profiles were measured in a step mode, which involves 0.0005°/step and 10 second exposure per step. The scans were repeated 19 times, which satisfied the requirement for a good counting statistics. The entire data were collected for approximately 18 hours.

7.3. Experimental results

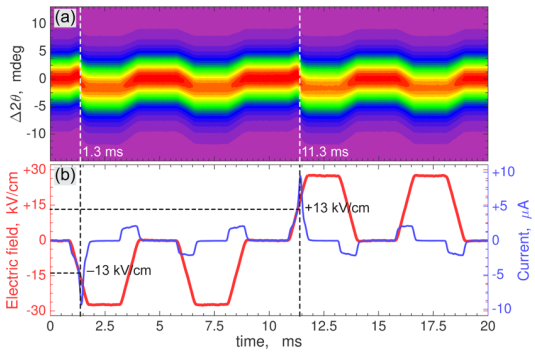

Figure 7.3 Time-resolved X-ray powder diffraction of BT-BZT under applied electric fields. (a) The {111} diffraction intensity as a function of time and diffraction angles; the dashed lines show the switching times indicating the maximum of peak position (minimum of the lattice spacing). (b) The time dependence of the applied electric fields (±27 kV/cm) and the obtained electrical currents.

Figure 7.3 shows the observed time-resolved {111} powder diffraction profiles of the BT-BZT sample under an alternating electric field. The applied electric double-pulses profiles are shown in Figure 7.3(b) as red line. The first pulse induces the ferroelectric switching but the second pulse cause the pure dielectric response only (see the blue line of the Figure 7.3(b)). Thus, the response of the material can be measured as the ferroelectric and piezoelectric feature, respectively. The observed diffraction profiles $f(2\theta, t)$ are analyzed to integrated intensities and extract the center of mass peak positions according to,

$$I(t) = \int f(x,t)\,dx \quad , \quad \langle 2\theta \rangle(t) = \frac{1}{I(t)} \cdot \int x \cdot f(x,t)\,dx \tag{7-2}$$

All data analysis performs using MATLAB (The MathWorks Inc., Natick, MA, USA) software. Figure 7.4(a) shows the extracted averaged peak positions and intensity variations as a function of time.

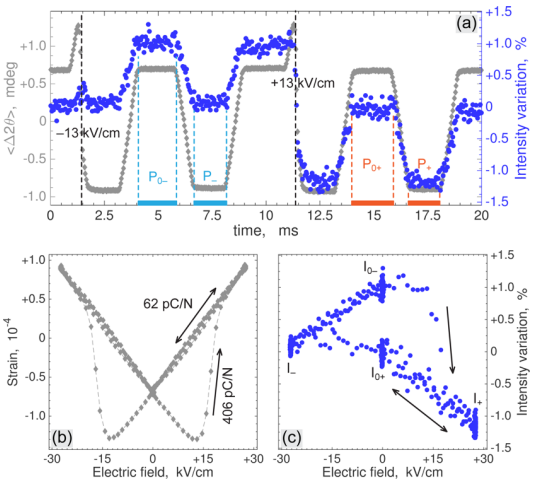

Figure 7.4 (a) The time dependence of the observed averaged peak positions and intensity variations. (b) The field-induced strain curve (changes of a_{111} lattice spacing) shows a typical butterfly hysteresis loop, involving two different piezoelectric coefficients. (c) The field dependence of the integrated intensity changes.

Figure 7.4(b) shows the strain as a function of the applied electric fields. The strain values can be calculated by,

$$\frac{\Delta a_{111}}{a_{111}} = -\frac{1}{2 \tan\theta}\langle \Delta 2\theta \rangle \tag{7-3}$$

Here, the averaged peak position $\langle \Delta 2\theta \rangle$ can be defined by the single {111} lattice spacing $a_{111} = \frac{\lambda}{2 \sin\theta}$ where λ is the X-ray wavelength.

In Figure 7.4(b), the coercive field for polarization reversal considering the response of the lattice strain can be directly found, which is defined by the minimum of the $a_{111}(E)$ so that the E_C = 13 kV/cm. Through this result, the piezoelectric constant can be calculated during the linear strain–field curves (the arrows in Figure 7.4(b)),

$$d_{111} = \frac{1}{a_{111}}\frac{\partial a_{111}}{\partial E} \tag{7-4}$$

The piezoelectric response shows a 6.5 times higher value during the polarization switching time intervals compared to the value measured elsewhere. The polarization response can be analyzed using the observed integrated intensity variations of the diffraction profiles (Figures 7.4(a) and (c)) through the change of the structure factors in the unit cell. Particularly, the field-induced integrated intensity changes after the first switching pulses can be an evidence for the polarization reversal and the breaking of Friedel's law due to the resonant scattering. Thus, two different types of polarization states can be considered from the resonant intensity changes (as marked in Figure 7.4(a)), which are $P_+ = -P_-$ and $P_{0+} = -P_{0-}$. These two states indicate the mutually reversed polarization states on the field-applied and zero-field (remnant) states respectively. The ~1 % intensity difference between positive and negative states significantly exceeds the 0.2 % uncertainty estimated from the Poisson statistics. The results of the integrated intensity changes as a function of the applied electric field are shown in Figure 7.4(c).

The results, which can simultaneously measure the lattice strain and the polarization reversal phenomena using the stroboscopic data-acquisition technique, could open a new insight into the investigation of the dynamics of the ferroelectric ceramics under the rapidly applied electric field. Figure 7.5 shows a detailed information in terms of the structural responses during the negative (a, c) and positive (b, d) switching fields.

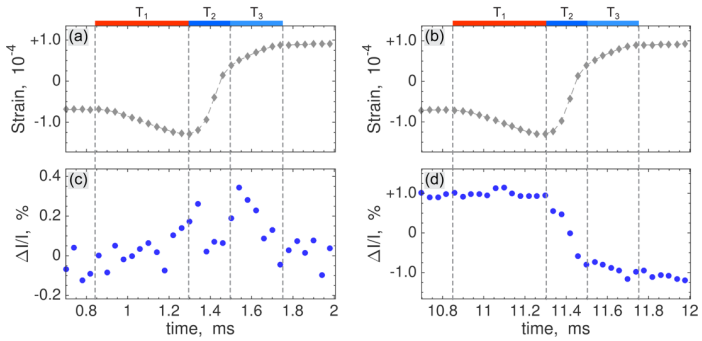

Figure 7.5 Time dependence of the strain (a, b) and the integrated intensity (c, d) during two intervals, which are the negative (a, c) and the positive (b, d) switching pulses. Three time regions (**T1**, **T2**, **T3**) are showing the switching procedure.

The polarization reversal process can be distinguished in three time intervals (marked in Figure 7.5) as follows:

(1) **T1** (red) - where the weak electric field opposes the initial polarization direction,

(2) **T2** (dark-blue) - where the applied electric field exceeds the coercive field and switching is evidenced by the fast change to the piezoelectric response,

(3) **T3** (bright-blue) - where the switching progress has completed and the electric field is parallel to the polarization direction.

Figure 7.6 show the field-dependent lattice response during the switching progress, that can be inferred for the dynamics of the structural inversion process on the polarization reversal. The interesting thing is that the lattice strain (grey diamonds) linearly changed under the applied electric field, but the polarization response (blue dots) shows a different way; i) the atomic displacements are larger when the electric field is parallel to the polarization direction while ii) they have smaller when the field direction is opposite to the polarization. Through this important key in terms of the polarization reversal process, a possible structural model for the polarization reversal process can be considered.

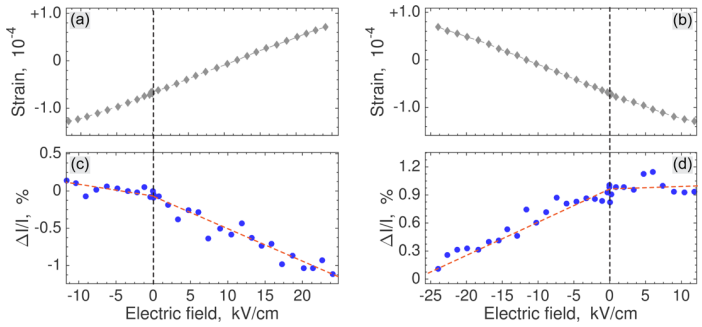

Figure 7.6 A detailed information of the strain (a, b) and intensity (c, d) response as a function of two intervals, which involve the negative (a, c) and the positive (b, d) switching pulses.

7.4. Interpretation and discussion

7.4.1. Model of the structural inversion

The atomic displacements can be analyzed using the observed intensity variations, because the integrated intensity of the diffraction profile for a single domain grain is proportional to the squared structure factor, $I_{kl}(t) \propto |F_{kl}|^2$, and the structure factor can be calculated by,

$$F_{kl} = \sum \left[f + f'(\lambda) + if''(\lambda)\right] \cdot T \cdot exp\{2\pi i(hx + ky + lz)\} \quad (7\text{-}5)$$

where f is the atomic form factor, T is the Debye-Waller factor, x , y , z are the fractional positions of the μ's atom in the unit cell, and $f'(\lambda) + if''(\lambda)$ is a term for the resonant scattering corrections as a function of the incident beam wavelength.

If the factor f'' is non-zero in Equation (7-5), the squared structure factor $|F_{kl}|^2$ can be sensitive to structural inversion due to the violation of the Friedel's law. For the BT-BZT sample and at the wavelength of λ = 0.3998 Å, the f'' values for these atoms are 0.82 (Ba), 4.19 (Bi), 0.50 (Zr) and 0.14 (Ti) [173].

Figure 7.7(a) shows the unit cell of the **ABO**$_3$ tetragonal perovskite-based structure with the **A** sites, occupied by Ba^{2+}/Bi^{3+}, and the **B** sites, occupied by Zn^{2+}/Ti^{4+} ions. Figure 7.7(c) and (d) show the model, which is the structural inversion to the over-coercive electric field with a fixed oxygen framework and shifting the cations, **A** (μ = 1) and **B** (μ = 2), along the polar axis relative to their ideal perovskite [0, 0, 0] and [1/2, 1/2, 1/2] positions, respectively. Furthermore, assuming these shifts $\Delta z\ (E)$, they are scaled by an electric field dependent normalized polarization factor $p(E)$, so that $\Delta z\ (E) = g \cdot p(E)$ where g are the model parameters describing spontaneous polarization due to the atomic displacements. The normalized polarization $p(E)$ can be defined by $p(0) = \pm 1$ and $p(\pm E_{max}) = \pm p_{max}$.

It is directly connected with the net macroscopic polarization of a single domain according to:

$$P(E) = \frac{p(E)}{V} \sum Q \cdot q_e \cdot g \quad (7\text{-}6)$$

where V is the volume of the unit cell and $Q \cdot q_e$ are atomic charges of the μ's atom, $q_e = 1.6 \cdot 10^{-19}\ C$ is an elementary charge. Since the atomic charges are time independent, the dynamics of the net polarization, $P(E)$, must be identical to the dynamics of the normalized polarization $p(E)$.

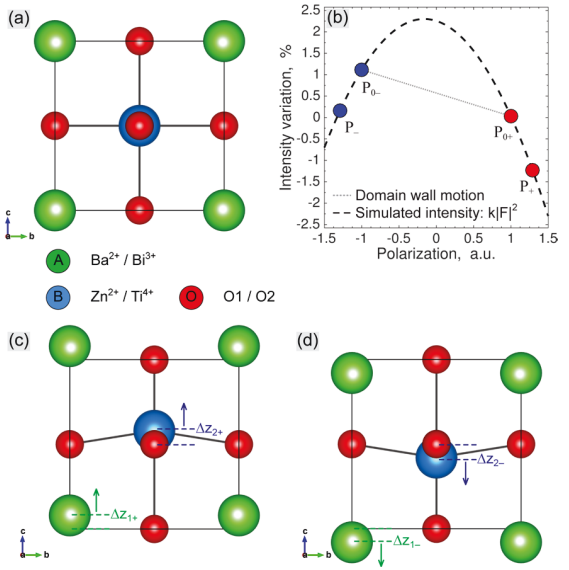

Figure 7.7 Illustrations for the tetragonal perovskite unit cell (*P4mm* space group), drawn using VESTA package [89], and the simulated 111 intensity variation. (a) The perfect perovskite unit cell. (c, d) The tetragonal perovskite unit cell, described by the atomic displacements. The polarization dynamics is considered by the off-centered **A**-positions' atoms (Δz_1) and **B**-positions' atoms (Δz_2). The oxygen octahedra cages were fixed for this model.

The observed diffraction intensities (I_{0+}, I_{0-}, I_+, I_-) are firstly analyzed during the four intervals (P_{0+}, P_{0-}, P_+, P_-), as marked in Figure 7.4(a). Therefore, the displacements of the **A** and **B** cations during these four intervals can be represented by three parameters g (μ = 1, 2) and p_{max}, obtained by $\Delta z = g$, $-g$, $p_{max} \cdot g$, $-p_{max} \cdot g$, respectively. From Equation (7-5), the values of these parameters can be found to be g_A=0.0521(1),

g_B=0.0590(1), p_{max}=1.236 minimizing the difference between the observed intensities (I_{0+}, I_{0-}, I_+, I_-) and their corresponding squared structure factors ($k|F|^2{}_{0+}$, $k|F|^2{}_{0-}$, $k|F|^2{}_+$, $k|F|^2{}_-$), where k is the scale factor. This corresponds to the zero-field off-center displacements of **A** and **B** sub-lattices by ~0.2 Å and their further enlargement by 23.6 % as the electric field amplitude increases from 0 to 27 kV/cm. It is emphasized that these out-of-center displacements could not be determined unless the resonant scattering were present and the squared structure amplitudes during positive and negative polarization were different.

Understanding the relationship between the polarization reversal and the observed intensity changes due to the structural inversion responses can reveal fundamental insight into the nature of the switching process. The dashed line in Figure 7.7(b) shows the expected change in the intensity $k|F|^2$ with variation to the normalized polarization $p(E)$ resulting from the cation displacements $\Delta z\ (E)$. The filled circles (red/blue) mark the experimentally measured polarization states, P_{0+}, P_{0-}, P_+, P_- respectively. In the case of homogenous switching (i.e., passing of the atomic displacements $\Delta z\ (E)$ through zero) between P_{0-} and P_{0+}, the intensity response would follow the dashed parabolic arc. However, a polarization reversal through 180° domain wall motion (i.e. changes to the volumetric ratio of the P_{0-} and P_{0+} domains) may follow the straight dot line. Therefore, it is possible to determine the switching mechanism by measuring the intensity during the switching process.

7.4.2. Dynamics of the intrinsic polarization

This section discusses in more detail with respect to the dynamics of the intrinsic polarization p considering the time dependence of Friedel pair intensities. Here, the dynamic response can be described by four regimes. First two stages are marked as A_+ and A_-, in which the polarization is parallel to the field (i.e. purely dielectric response without switching) and other two intervals are shown as B_+ and B_-, where the intrinsic polarization is antiparallel to the field (and below coercive field, < E_C).

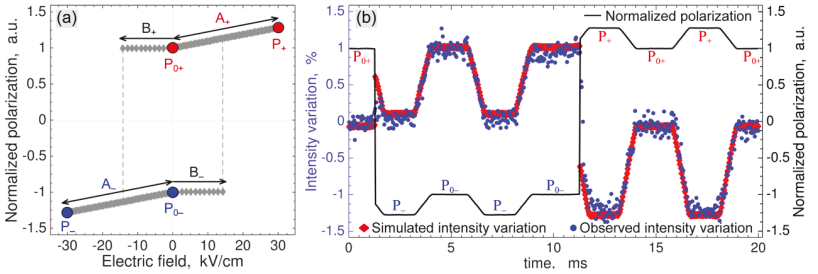

Figure 7.8 (a) Model hysteresis loops; field dependence of the normalized polarization, inferred from the observed intensity variations. (b) The comparison between the simulated and the observed intensity variations. The black curve indicates the time dependence of the normalized polarization corresponding to the atomic displacements.

Figure 7.8(a) shows the four regimes, which are illustrated on the normalized polarization hysteresis loop $p(U,t)$. The change of atomic positions during the applied electric field cycle is represented between the reference polarization positions, P_{0+}, P_{0-}, P_+, P_- (marked by red/blue circles in Figure 7.8(a)). In the four stages, each local dielectric susceptibility (marked by the arrows) can be evaluated by $p_{A\pm}(E) = \chi_A \cdot E \pm 1$, and $p_{B\pm}(E) = \chi_B \cdot E \pm 1$, where $\chi_A = (p_{max} - 1)/E_{max}$. Here, χ_B is much smaller than χ_A (for this simulation, the ratio $\chi_B/\chi_A = 0.045$). The structural inversion process under the polarization reversal can be modelled by the assumption that the polarization is immediately switching from $p_{B\pm}(E)$ to $p_{A\mp}(E)$. Figure 7.8(b) compares the observed (blue dots) and simulated (red diamonds) intensity changes corresponding to the time and electric field dependence of the intrinsic polarization feature. The plot shows the remarkable agreement between the model and the observed intensity data. The main deviation between the simulated and the observed intensity occurs during the switching time ranges (i.e. immediately following $B_{+/-}$ marked on Figure 7.8(a)). However, this can be a strong evidence of the switching process.

As shown in Figure 7.7(b), the homogeneous structural switching route follows in ~2.5 % intensity increase, but it was not observed in this experiment. There are two reasons that the considered model makes such an overestimation as follows,

(1) Either the polarization reversal must occur at time scales less than the 2 μs time, which is the resolution of this experiment, or

(2) The structural inversion does not occur homogeneously and the normalized polarization p never passes through zero state in the sampled grains.

Because prior works have not given abundant evidence of homogeneous switching and reported switching processes occurring on the μs time scale, this study can conclude that the polarization reversal is likely to follow a 180° domain wall motion mechanism, upon which the volumetric ratios of the states P_{0+} and P_{0-} are modified under the applied electric fields.

7.5. Conclusion

This experiment combined the techniques between the resonant X-ray diffraction and the developed stroboscopic data-acquisition system. The combination allowed to measure the dynamics of the structural responses regarding to the intrinsic strain, the spontaneous polarization and the dielectric response in BT-BZT ferroelectric ceramics. For the first time, the results have shown that it is possible to measure Friedel pair contrast using high-energy X-ray powder diffraction. Because the hkl and $-h-k-l$ powder rings exactly overlap with one another, the conditions at which the violation of Friedel's law can be observed using a powder diffraction are very rare. However, the conditions can only be realized if,

(1) A structure of individual powder grains can be actively inverted during the measurement and

(2) The intensity of powder diffraction patterns is high enough to detect the small difference. With the current study, the method has become accessible for investigation of ferroelectric powders under alternating electric field and at high energy of the X-rays.

In summary, this study showed that a homogeneous spontaneous polarization of BT-BZT sample can be considered by the averaged displacement of **A** and **B** cations by ~ 0.2 Å along the polar axis relative to the oxygen octahedra. In doing so, this experiment provided the evidence that the polarization reversal must be completed during a time

interval that is either shorter than 2 μs (time resolution of the experiment) or, if not, likely to occur through 180° domain wall motion. The used method in this experiment opens a new strategy for determining structural inversion mechanisms in ferroelectrics.

Chapter 8

Summary

This thesis described the investigation of the field-induced strain and domains dynamics in single crystal and ceramic ferroelectrics under an alternating electric field using a combination of synchrotron X-ray diffraction and the custom-built stroboscopic data-acquisition systems. This approach was applied to two different material systems: ferroelectric single crystals ($Na_{0.5}Bi_{0.5}TiO_3$ and $Sr_{0.5}Ba_{0.5}Nb_2O_6$) and $BaTiO_3$-based polycrystalline ceramics.

Chapter 4 introduced the new data-acquisition systems allowing for various successful experimental strategies. The developed systems are mainly distinguished by the pros and cons with respect to the state-of-the-art detector types: single-photon counter (e.g. scintillation counter, avalanche photo diode (APD) detector, etc.) and pixel area detector (e.g. Pilatus, Eiger etc.). One system using the single-photon counter has the advantage of providing a high-angular resolution (sub-millidegree) and fast-time resolution (nanosecond), whereas the other system using the pixel area detector can define its time resolution via the frame acquisition rates (e.g. a few milliseconds) defined by the detector specification. The latter is able to measure a large area in reciprocal space. The design of the systems, as well as the LabVIEW- (National Instruments Inc., Austin, TX, USA) and MATLAB-based (The MathWorks Inc., Natick, MA, USA) control software programs, is suitable for further development. The following chapters represented the successful research results using the innovative experimental strategies.

Chapter 5 investigated the monoclinic lattice distortion in the $Na_{0.5}Bi_{0.5}TiO_3$ single crystal under an applied alternating electric field using a synchrotron-based high-resolution time-resolved single crystal X-ray diffraction method. The results showed the characteristic diffraction features of the monoclinic distortion − splitting of specific Bragg reflections − and their changes under the applied external electric fields. In order to analyze this feature, a crucial model, which is a direct coupling between the monoclinic strain and the polarization rotation, was considered. The good agreement between the observed and simulated monoclinic distortion parameters could imply that the piezoelectric effects, corresponding to the relationship between the field-induced lattice strain and polarization rotation, are intrinsic, rather than extrinsic, origin. This chapter

concluded that the observed polarization rotation contributed to the intrinsic piezoelectric effect up to ~50 pC/N.

Chapter 6 studied the enhanced electromechanical coupling of a uniaxial $Sr_{0.5}Ba_{0.5}Nb_2O_6$ ferroelectric single crystal under an alternating electric field using time-resolved single crystal X-ray diffraction. The structural origin of the enhanced piezoelectric activity in ferroelectrics remains poorly understood because of the lack of appropriate experimental techniques and the mixing of different mechanisms related to ferroelectricity and ferroelasticity. The uniaxial ferroelectrics only form 180° domains with the opposite polarization direction because the appearance of ferroelastic strains is restricted by symmetry. Therefore, the interrelation between piezoelectricity and ferroelectricity can be clearly investigated in a well-defined manner. In this study, a hidden mechanism in the bulk system was observed: it suggests that the highest piezoelectric activity is realized in the volumes where nucleation of small ferroelectric domains takes place. This newly suggested mechanism can create a new roadmap for designing novel functional materials with enhanced piezoelectric properties.

Chapter 7 investigated the multi-scale structural origin of electric field-induced strain and polarization switching in the perovskites $BaTiO_3$-$BiZn_{0.5}Ti_{0.5}O_3$ (BT-BZT) polycrystalline ferroelectrics. This material is a prototypical of a lead-free piezoelectric with a complex switching mechanism, since electromechanical couplings in ferroelectrics extend over several length scales and a broad range of time domains: from the atomic scale to the macroscopic device. In order to investigate the relationship between the field-induced strain and polarization reversal phenomena, this study implemented a resonant X-ray scattering where the diffraction peaks between Friedel pairs were observed with small differences of the integrated intensity. The combination of synchrotron high-energy X-ray powder diffraction and the custom-built new stroboscopic data-acquisition system could lead to direct and simultaneous measurement of both lattice strain and polarization reversal under an alternating electric field. This strategy gives the benefit of combining spectroscopic and diffraction-based measurements into a single and robust technique with a time resolution of down to the nanosecond scale, thus it opens a new window into *in situ* structure-property characterization that probes the full extent of ferroelectric phenomena.

Finally, this thesis demonstrated that the combination of the stroboscopic multi-channel analyzer data-acquisition system and X-ray diffraction is a very powerful tool to investigate the field-induced strain and domain dynamics in ferroelectrics under an alternating electric field. This type of study can give deep insights into the origins of

electromechanical coupling in piezoelectric/ferroelectric materials with a view to designing new functional materials with enhanced physical properties.

Appendix A. Installation/Operation of the data-acquisition systems

This appendix describes how to install and operate the data-acquisition systems for the experiments. The systems were mainly constructed by Stefan Heidbrink, Marco Vogt, Jens Winter, and Michael Ziolkowski (Electronics Laboratory, Department of Physics, University of Siegen, Germany).

A.1. Installation/Operation for the first data-acquisition system (FPGA-board, version 2010)

The installation of the first data-acquisition system is described as follows (see Figure A.1):

(a) The external trigger clock signal is connected between the function generator 'TRIG OUTPUT' and the FPGA-board 'BLACK WIRE ((1) in Figure A.1(a))', using the LEMO cable and adapter. The amplitude should be within 3.0 ~ 3.3 V.

(b) The detector pulse from the discriminator 'TTL NIM OUTPUT' is connected to the FPGA-board 'BLUE WIRE ((2) in Figure A.1(b))' using the LEMO cable and adapter. The amplitude should be within 3.0 ~ 3.3 V.

(c) The diffractometer movement trigger signal from the specified MOTOR TRIGGER signal, which provided at the beamlines, is connected to the FPGA-board 'BLUE WIRE ((3) in Figure A.1(c))' using the LEMO cable and adapter. The amplitude should be within 3.0 ~ 3.3 V.

(d) The 'SIGNAL OUTPUT' of the function generator is connected to the high-voltage amplifier 'Vcon-in'. This output signal should be set to high-impedance, not 50 Ω termination. The output factor of the high-voltage amplifier is 300 times (e.g. ±10 V → ±3 kV).

(e) The applied high-voltage signal on the sample can be monitored using the oscilloscope system. The 'Vmoni' of the high-voltage amplifier is connected to any channel of the oscilloscope. The data can be recorded as the '.CSV' format.

(6) Finally, the USB port (GREY WIRE) is connected into the portable computer to start the control program (LabVIEW-based program).

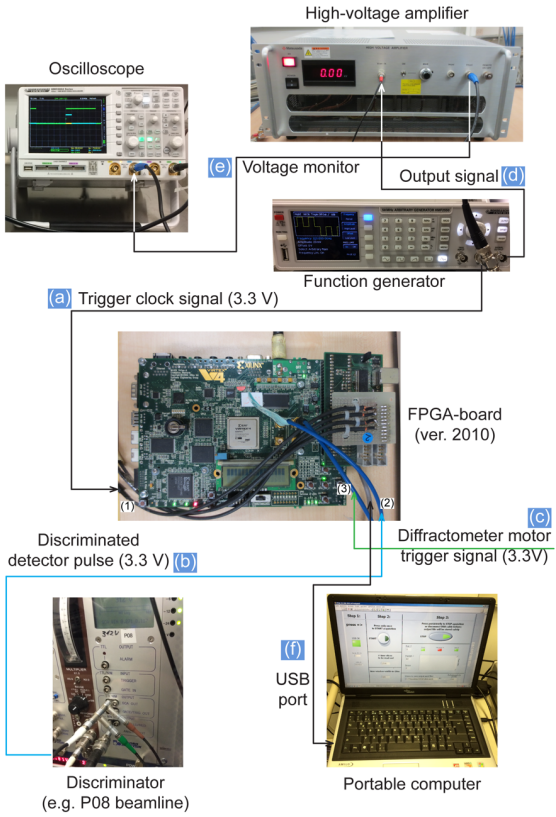

Figure A.1 A schematic diagram of the installation for the first data-acquisition system, which involves a function generator (HMF-2550, Hameg), a high voltage amplifier (AMT-3B20, Matsusada), an oscilloscope (HMO-3004, Hameg), and a FPGA-board (version 2010).

After all connections are complete and the power of the devices has been checked, then the LabVIEW-based control program can be opened. Figure A.2 shows a screen shot of the control program panels. After opening the program, the parameters for the measurement are input as follows:

(a) '# time-slices to be read-out': This corresponded to the number of channels to be read out for the data. This system allows for a maximum of 10000 channels. The program is set to one quarter of the total number of channels. Examples are given in Table A.1.

(b) 'time-window-width-in-10ns': This parameter defines the time resolution. The width of a channel cannot be smaller than 100 ns for this FPGA-board (version 2010). Here, the number '10' means 100 ns resolution for each channel. Thus, it should be kept its number for the minimum time resolution. The available numbers are shown in the examples in Table A.1.

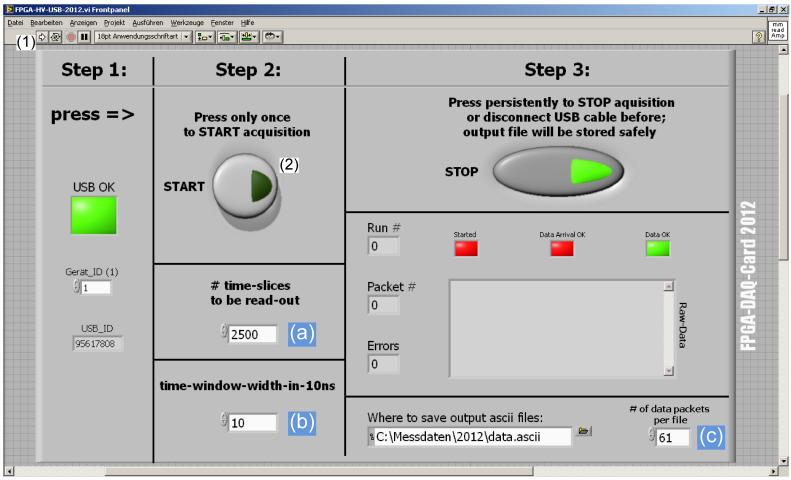

Figure A.2 A screen shot of the parameters in the LabVIEW-based control program: (a) time-slices to be read-out, (b) time-window-width-in-10ns and (c) the number of data points in a scan.

(c) '# of data packets per file': This is related to the angular step numbers. For example, if the diffraction peak is measured with 61 steps, then this number should be input into this panel.

After all of these parameters into the program panels are input, then the stroboscopic time-resolved diffraction measurements can be started by clicking the two buttons shown in the Figure A.2. The clicking number '(1)' button tells the system: 'we are ready to measure!'. After this, simultaneously press the 'START' button (the number '(2)') with the X-ray diffraction control software (e.g. SPEC program).

Frequency (Hz)	2000	1000	500	100	50	20	10
# time-slice	1250	2500	2500	2500	2500	2500	2500
time-window	10	10	20	100	200	500	1000

Table A.1 Examples of the input parameters for the stroboscopic measurements with the different repetition rates (i.e. the external electric fields).

A.2. Installation/Operation for the second data-acquisition system (FPGA-board, version 2016)

This section describes the operation of the new developed data-acquisition system and the control program.

Firstly, connect all the signals from (1) the discriminated detector pulses, (2) the external clock trigger and the diffractometer movement into the FPGA-board using the LEMO cable and adapter (see Figure A.3(a)). The amplitude of all signals should be within the 3.0 ~ 3.3 V ranges.

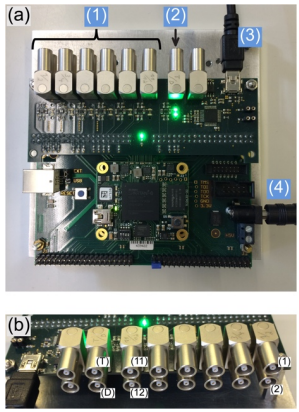

Figure A.3 Photographs of the new data-acquisition system (FPGA-board, version 2016). (a) Top view of the system: (1) connectors for 12 detectors, (2) input for the external trigger signal '(T)' and the diffractometer movement signal '(D)', (3) USB port for connecting to the control computer, (4) power supply. (b) The part of the LEMO connectors in the system: the numbers from '(1)' to '(12)' are connected from the discriminated detector pulse(s).

After the USB port ((3) in Figure A.3(a)) is connected to the control computer, the stroboscopic diffraction measurements can be started using the LabVIEW-based control program (see Figure A.4) as follows:

(i) The measurement parameters are input on the 'Setup' panel (red box '(1)' in Figure A.4).

1) 'Com Port': It needs to find the connected USB port and hence needs to select the 'refresh' on this panel. This will find the current connected port.

2) 'HV Period': This parameter corresponds to the cyclic external electric field period. The unit is set to microseconds. Since this system has the maximum 10000 channels with 10 ns resolution for each channel, the default value is set to 100 μs. For example, if the measurement performs with 1 kHz periodic electric field, then it needs to input 1000 μs in this parameter. Accordingly, the system automatically re-bins to 100 ns time resolution.

3) 'Angle Steps': This related to the angular step numbers for each diffraction scan.

4) 'Repetitions': This parameter corresponds to the repeat numbers: how many times the measurements need to make scans for the diffraction peak (e.g. rocking curves).

(ii) After input all of the experimental parameters, the measurement can be started to press the arrow button (number '(2)'). An advantage of this system is to wait the next incoming diffractometer movement trigger. Consequently, all trigger signals are synchronized when the diffraction measurement is started on the SPEC program.

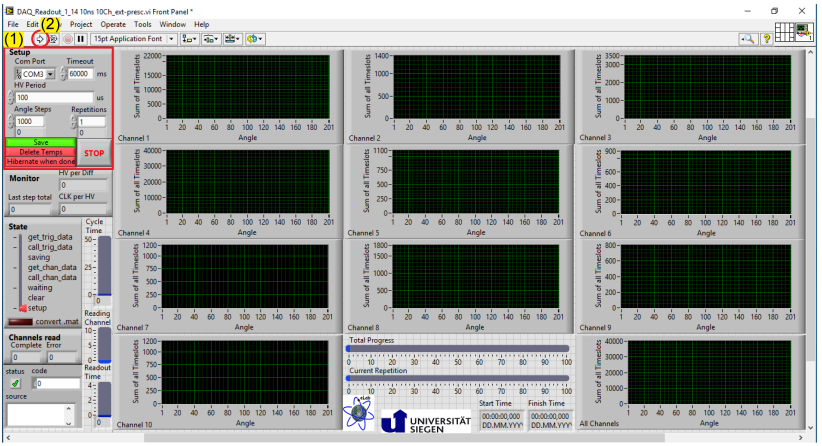

Figure A.4 A screenshot of the LabVIEW-based control program for the new system.

A.3. Installation/Operation for the microcontroller-based third data-acquisition system

This section demonstrates how to install/operate the microcontroller-based data-acquisition system. The microcontroller can synchronize with the 2D area detector (e.g. Pilatus, Eiger, etc.) triggering rectangular pulses (exposure time of the acquisition frames) and generate the step-like output voltage signals the same as a function generator. Figure A.5 shows an illustration of an installation of this data-acquisition system.

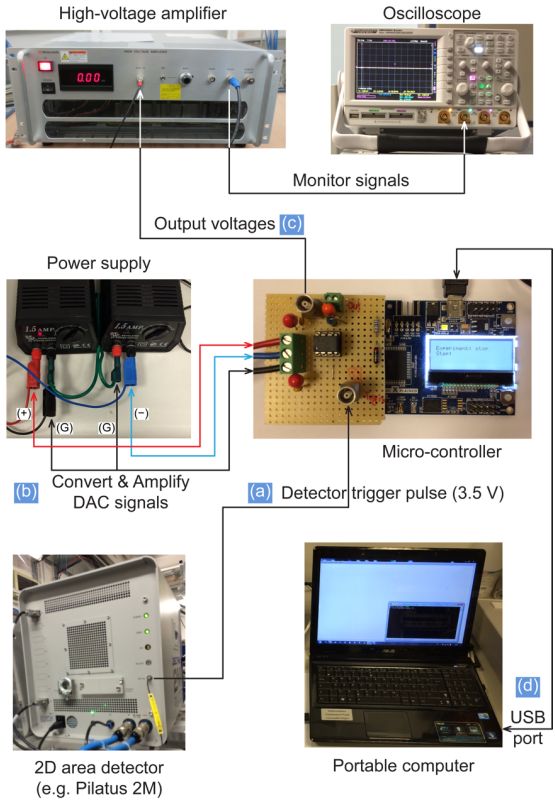

Figure A.5 A schematic drawing for the installation of the microcontroller-based data-acquisition system (details are explained in the text).

The procedure for system setup is described as follows:

(a) 'Detector trigger pulse(s) input unit': The acquisition frame (exposure time) is set to the width of a rectangular pulse, which is directly controlled by the detector software. The amplitude of the pulse should be between 3.0 ~ 3.5 V.

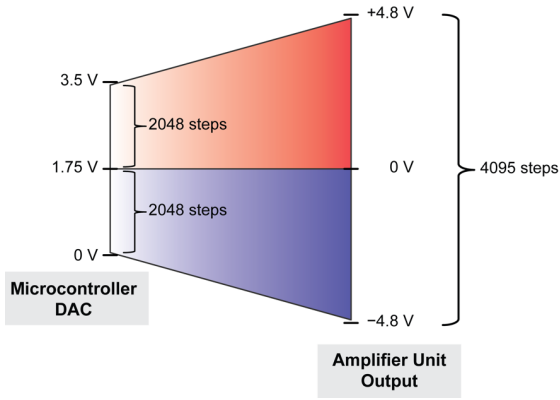

Figure A.6 A schematic illustration for the process of the convertor and amplifier unit: refer to the part '(b)' in Figure A.5.

(b) 'Convertor and Amplifier for DAC (Digital-Analog-Convertor) signals unit': This is one of the important units for this data-acquisition system. The microcontroller actually involves the DAC itself, which provides logic signals (0 V → 3.5 V). However, it needs to generate a bipolar voltage output signal. For this reason, it should be added an additional amplifier unit (home-built orange PCB-circuit and power supply). Two power supplies are used to provide over DC ±4.8 V, respectively. In this setup, both power supplies are set to 9 V. The power supplies were supported by the Swiss-Norwegian Beamline (SNBL) BM01 of the European Synchrotron Radiation Facility (ESRF). Figure A.6 shows a schematic diagram for this amplifier unit.

(c) 'Voltage signal(s) output unit': After the amplification from unit corresponding to the '(b)' step, the microcontroller accordingly generates the step-like bipolar output voltage signals up to ±4.8 V with 4095 steps (see Figure A.6).

(d) 'Control program unit': The microcontroller is a programmable system, which is operating the contents of a '.CFG' file. The file can be transferred from the PC to the microcontroller by the 'Microsoft Visual C# program'. Figure A.7 shows one example of the format of the contents, which involve the desired output voltages with the given steps. These files can be generated by the MATLAB program.

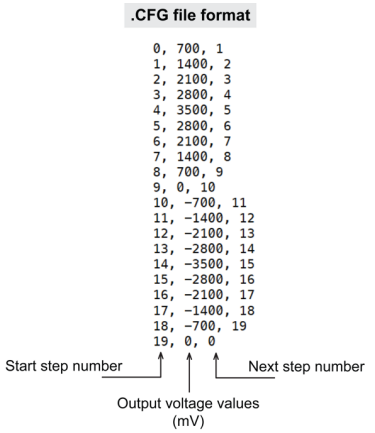

Figure A.7 An example of the description for generating a desired output voltages with given steps. The first column is the starting step number. The second column is the desired output voltage values in mV. The last column is the next step number. Here, the important thing is that the last step number '0' of the third column should be same as the number '0' of the first step in the first column. Therefore, the output voltages are generated as a periodic.

The control program can be run on the Console Host in Microsoft Windows 7 (or later versions). The operating procedure is as follows:

(1) Open the command terminal window on the Console Windows Host.

(2) Go/Run to '[Path]\ control.exe FILENAME.CFG [COM]'. Here, the 'COM' means a serial interface in Windows environments.

After these commands, the system is now ready to start taking measurements: press the key 'S' to 'START' the measurement and press the key 'E' to 'STOP' the measurement, respectively.

Appendix B. Drawings of the designed sample holders

B.1. Sample holder I (for single crystals)

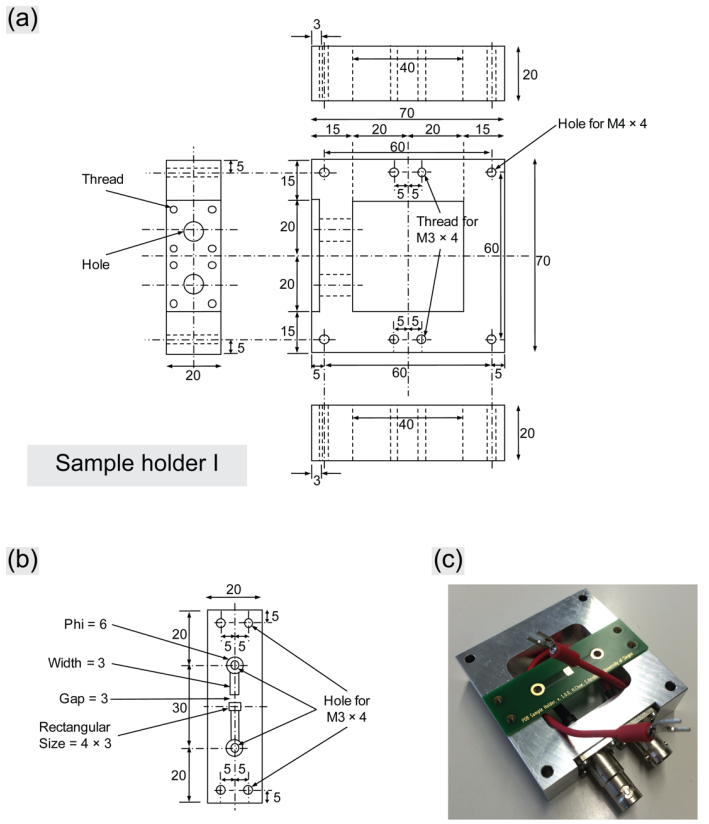

Figure B.1 A sketch of the sample holder I for mounting single crystals. (a) Drawing the Aluminum plate. (b) PCB-board design for mounting crystal. The dimension is millimeter. (c) Photograph of the assembled sample holder I.

B.2. Sample holder II (for polycrystalline samples)

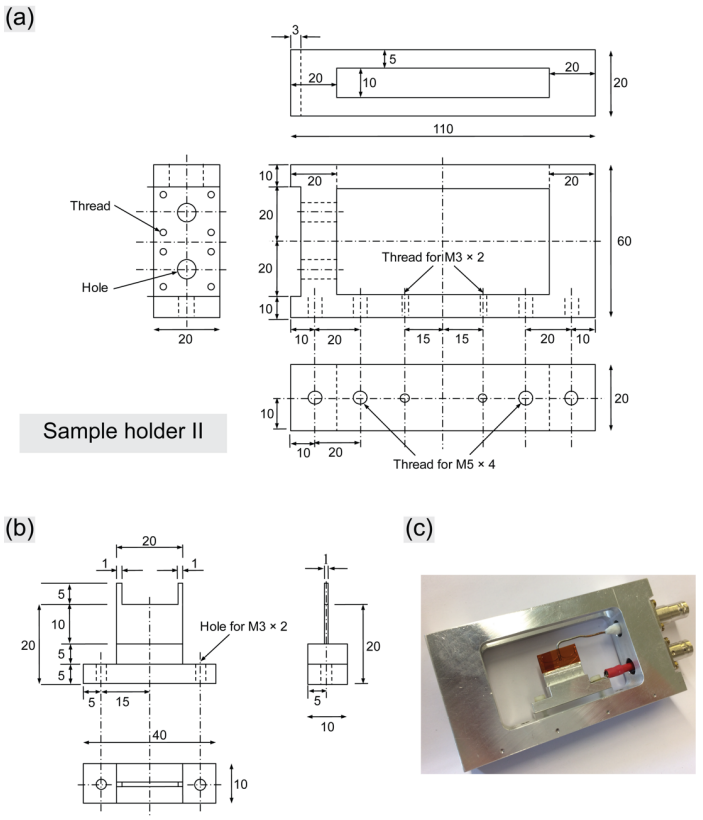

Figure B.2 A sketch of the sample holder II for mounting polycrystalline samples. This holder has designed for the powder diffraction experiments. (a-b) Drawing the aluminum plates. The dimension is millimeter. (c) Photograph of the assembled sample holder II.

Appendix C. Fitting procedure for two-dimensional reciprocal space maps

C.1. Two-dimensional fitting process

Firstly, it needs to convert the observed ω versus 2θ reciprocal space maps into the coordinate system XY, where the X-axis is parallel to [110]* and the Y-axis is parallel to [001]*. This transformation was explained in more detail in Chapter 3 and shown in Figure 3.8. For an accurate two-dimensional fitting procedure, the following steps are performed (see Figure C.1):

(1) First step, a one-dimensional cut profile selects along the Y-axis at the X || [110]* = 0 position. (Figure C.1 (a) → (b))

(2) Second, the overall values are calculated, which are the integrated intensity, the averaged peak position (center of mass), the peak width (FWHM), and the skewness of the selected peak profile. (Figure C.1 (b) → (c))

(3) Third, it can be estimated the location of two peak components according to the skewness value. If the skewness is S < 0 (S > 0), then one peak component is located on the left (right) side of the overall averaged peak position with another peak component on the right (left) side. On the other hand, both peaks may overlap on the overall averaged peak position if the skewness is S = 0. (Figure C.1 (c) → (d))

(4) In this step, a fitting process can be started for the selected one-dimensional cut profile with a one-dimensional Pearson VII function as defined by,

$$f(x) = \frac{I}{\sigma_x}\left(2\sqrt{2^{\frac{1}{m}}-1}\right)\frac{\Gamma(m)}{\sqrt{\pi}\,\Gamma\left(m-\frac{1}{2}\right)}\left[1+4\left(2^{\frac{1}{m}}-1\right)\left(\frac{x-x_0}{\sigma_x}\right)^2\right]^{-m} \qquad \text{(C-1)}$$

where I is integrated intensity, x_0 is the averaged peak position, σ_x is the peak width, and m is the peak shape parameter. (see Figure C.1(d))

(5) Now, two peak cut profiles can be selected along the X-axis from the two-dimensional map. Each peak position (red/blue) on the Y-axis can be estimated from the results of Step (4). (Figure C.1 (d) → (e))

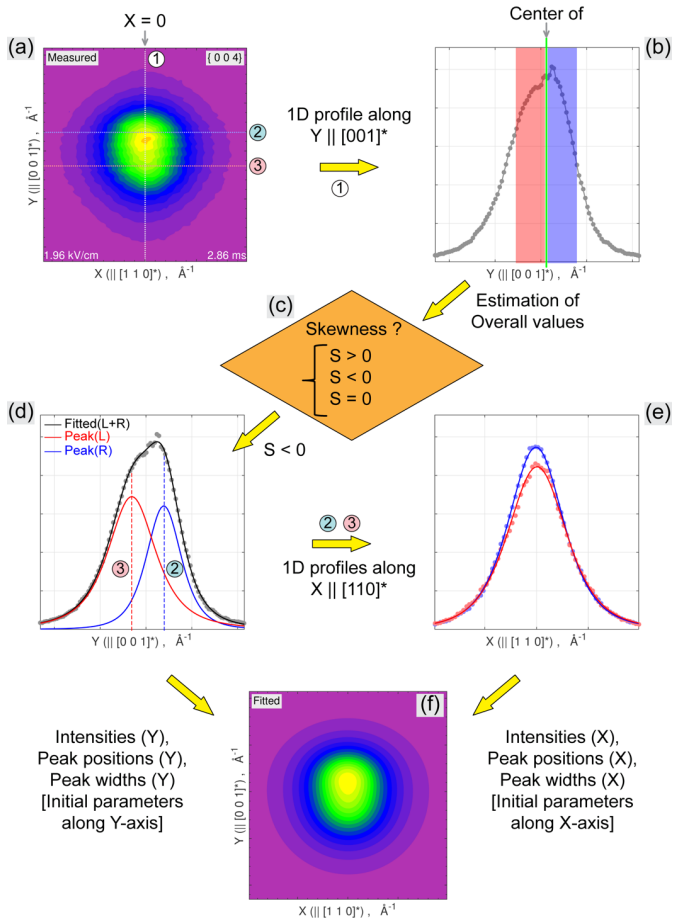

Figure C.1 A schematic diagram of the fitting process for the observed two-dimensional reciprocal space maps (details are explained in the text).

(6) From Step (5), the overall values (integrated intensities, peak positions, peak widths) for both peaks can be calculated. Accordingly, all initial parameters are ready to fit the two-dimensional maps with two components. (see Figure C.1(e))

(7) Finally, the observed data are doing the fitting procedure using the 2D Moffat distribution functions (refer to Equation (5-1)) as a function of time and electric field.

The initial parameters for each time step can be set from Steps (2) – (6). (see Figure C.1(f))

C.2. The fitting results for all parameters

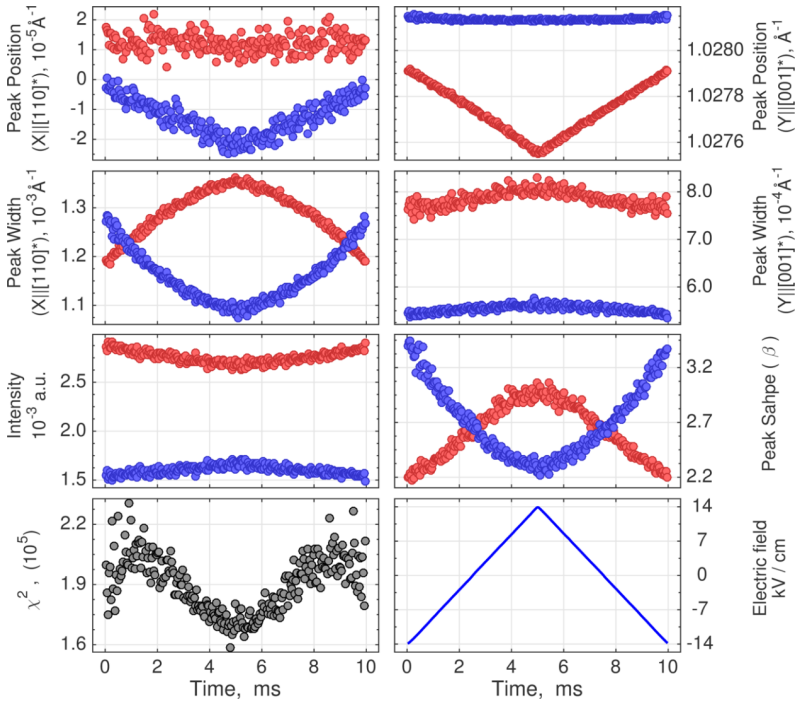

Figure C.2 The fitting results for all parameters: Averaged peak positions and Peak widths (for the X-, Y-component); Integrated intensities and Peak shapes.

Appendix D. Animations of the time-resolved two-dimensional reciprocal space maps and a model of the monoclinic distortion

The animations in this appendix are supplementary materials for the results in Chapter 5. Each animation is in 'mp4' video codec format. All video files are able to download in online.

Video D.1 All time-resolved ω versus 2θ intensity reciprocal space map around {004} reflections as a function of time and electric field with 100 Hz repetition frequency. (VideoD_1.mp4; https://www.dropbox.com/s/iho2imlsrew96fs/VideoD_1.mp4?dl=0)

Video D.2 All time-resolved reciprocal space maps: (left) the measured data; (right) the results of the best fit by the superposition of two 2D Moffat distribution function. (VideoD_2.mp4; https://www.dropbox.com/s/dc9023121emt31b/VideoD_2.mp4?dl=0)

Video D.3 An animation of a model for the monoclinic distortion and the polarization rotation, as shown in Figure 5.6(a). (VideoD_3.mp4; https://www.dropbox.com/s/8wk7utf5qo1zruk/VideoD_3.mp4?dl=0)

Video D.4 Comparison between (left) schematic dynamics of 12 monoclinic domains (Table in Section 5.4.2) and (right) the observed reciprocal space maps. (VideoD_4.mp4; https://www.dropbox.com/s/hes7rjqi5u2dqki/VideoD_4.mp4?dl=0)

Appendix E. Time-resolved rocking curves of $Sr_{0.5}Ba_{0.5}NbO_6$ under an alternating electric field

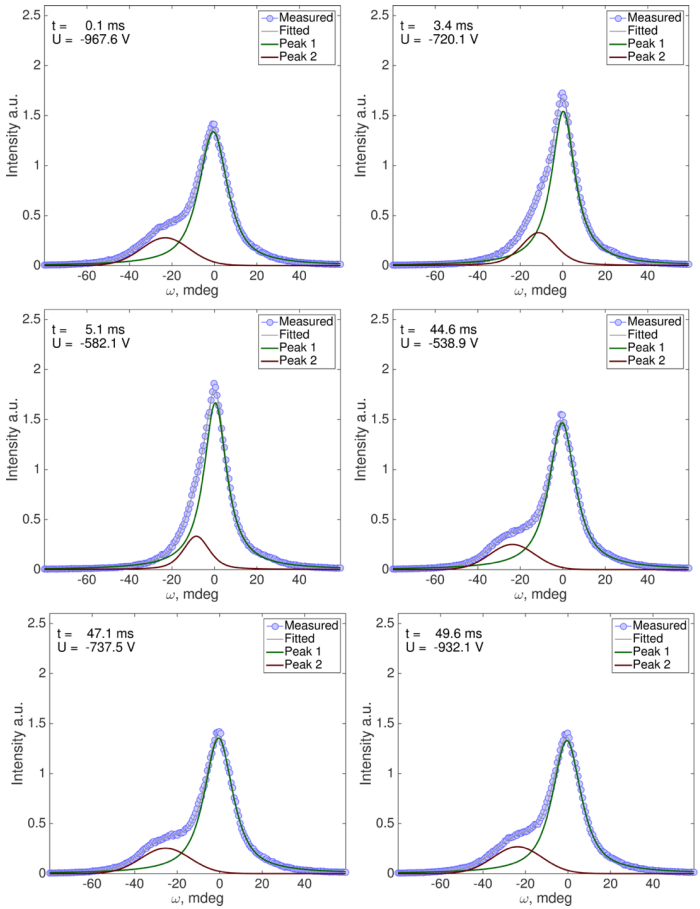

Figure E.1 Selected rocking curve profiles which are able to separate with two peak components, and hence the study of domain dynamics could be possible using the peak separation under two different time intervals. All time-resolved data are shown on Video E.1 (VideoE_1.mp4; https://www.dropbox.com/s/31n116fasfi8w2n/VideoE_1.mp4?dl=0).

References

[1] Valasek, J., 1921, “Piezo-Electric and Allied Phenomena in Rochelle Salt,” Phys. Rev., **17**, p. 475.

[2] Puget, R., and Godefroy, L., 1975, “Contribution À l’Etude de l’Ionicité Des Liaisons Dans Le Rutile,” J. Appl. Crystallogr., **8**, pp. 297–303.

[3] Lissalde, F., and Peuzin, J. C., 1976, “X-Ray Determination of Piezoelectric Coefficient in Lithium Niobate,” Ferroelectrics, **14**, pp. 579–582.

[4] Fujimoto, I., 1978, “Direct Detection of Electric-Field-Induced Microscopic Structural Changes in $LiNbO_3$ by Modulation X-Ray Diffraction,” Phys. Rev. Lett., **40**(14), pp. 941–944.

[5] Fujimoto, I., 1980, “Chemical Bond of GaAs Revealed by Modulation X-Ray Diffraction,” Jpn. J. Appl. Phys., **19**(7), pp. L345–L348.

[6] Fujimoto, I., 1982, “Electric-Field-Induced Ionic Displacement and Redistribution of Bonding Electrons in $LiNbO_3$ and $LiTaO_3$ Revealed by Modulation X-Ray Diffraction,” Acta Crystallogr. Sect. A, **38**, pp. 337–345.

[7] Pietsch, U., and Unger, K., 1987, “An Experimental Proof of the Valence Electron Density Variation in Silicon under High Electric Field,” Phys. Status Solidi, **143**, pp. K95–K97.

[8] Paturle, A., Graafsma, H., Boviatsis, J., Legrand, A., Restori, R., Coppens, P., Kvick, Å., and Wing, R. M., 1989, “The Influence of an External Electric Field on the X-Ray Scattering of 2-Methyl-4-Nitroaniline, an Organic Crystal with Nonlinear Optical Properties,” Acta Crystallogr. Sect. A, **45**, p. FC25-FC28.

[9] Ståhl, K., Kvick, Å., and Abrahams, S. C., 1990, “A Synchrotron X-Ray Study of the Surface Layer in Stoichiometric $LiNbO_3$ on Modulation by an Applied Electric Field,” Acta Crystallogr. Sect. A, **46**, pp. 478–485.

[10] Paturle, A., Graafsma, H., Sheu, H.-S., Coppens, P., and Becker, P., 1991, “Measurement of the Piezoelectric Tensor of an Organic Crystal by the X-Ray Method: The Nonlinear Optical Crystal 2-Methyl 4-Nitroaniline,” Phys. Rev. B, **43**, p. 14683.

[11] Graafsma, H., Paturle, A., Wu, L., Sheu, H. -S., Majewski, J., Poorthuis, G., and

Coppens, P., 1992, “Molecular Reorientation in an Electric Field as Studied by Single-Crystal X-Ray Diffraction,” Acta Crystallogr. Sect. A, **48**, pp. 113–120.

[12] Graafsma, H., Thorander, P., Heunen, G. W. J. C., and Morse, J., 1996, “Wide Dynamic Range Germanium Detector for Perturbation Crystallography,” J. Synchrotron Radiat., **3**, pp. 156–159.

[13] Graafsma, H., Heunen, G. W. J. C., and Schulze, C., 1998, “A New Synchrotron-Based Diffraction Technique for Perturbation Crystallography,” J. Appl. Crystallogr., **31**, pp. 414–422.

[14] Tucoulou, R., Roshchupkin, D. V., Mathon, O., Schelokov, I. A., Brunel, M., Ziegler, E., and Morawe, C., 1998, “High-Frequency X-Ray Beam Chopper Based on Diffraction by Surface Acoustic Waves,” J. Synchrotron Radiat., **5**, pp. 1357–1362.

[15] Guillot, R., Allé, P., Fertey, P., Hansen, N. K., and Elkaïm, E., 2002, “Diffraction Measurements from Crystals under Electric Fields: Instrumentation,” J. Appl. Crystallogr., **35**, pp. 360–363.

[16] van Reeuwijk, S. J., Puig-Molina, A., and Graafsma, H., 2000, “Electric-Field-Induced Structural Changes in Deuterated Potassium Dihydrogen Phosphate,” Phys. Rev. B, **62**, p. 6192.

[17] van Reeuwijk, S. J., Puig-Molina, A., Mathon, O., Tucoulou, R., and Graafsma, H., 2003, “Time-Resolved X-Ray Diffraction Study of the Relaxation Process of Electric-Field-Induced Strain in KD_2PO_4,” J. Appl. Phys., **94**, p. 6708.

[18] Larsson, J., Sondhauss, P., Synnergren, O., Harbst, M., Heimann, P. A., Lindenberg, A. M., and Wark, J. S., 2004, “Time-Resolved X-Ray Diffraction Study of the Ferroelectric Phase-Transition in DKDP,” Chem. Phys., **299**, pp. 157–161.

[19] Hansen, N. K., Fertey, P., and Guillot, R., 2004, “Studies of Electric Field Induced Structural and Electron-Density Modifications by X-Ray Diffraction,” Acta Crystallogr. Sect. A, **60**, pp. 465–471.

[20] Gorfman, S., Tsirelson, V., Pucher, A., Morgenroth, W., and Pietsch, U., 2006, “X-Ray Diffraction by a Crystal in a Permanent External Electric Field: Electric-Field-Induced Structural Response in α - $GaPO_4$,” Acta Crystallogr. Sect. A, **62**,

pp. 1–10.

[21] Gorfman, S., Schmidt, O., Pietsch, U., Becker, P., and Bohatý, L., 2007, “X-Ray Diffraction Study of the Piezoelectric Properties of BiB_3O_6 Single Crystals,” Zeitschrift Für Krist., **222**, pp. 396–401.

[22] Gorfman, S., Schmidt, O., Ziolkowski, M., Von Kozierowski, M., and Pietsch, U., 2010, “Time-Resolved X-Ray Diffraction Study of the Piezoelectric Crystal Response to a Fast Change of an Applied Electric Field,” J. Appl. Phys., **108**, p. 64911.

[23] Schmidt, O., Gorfman, S., Bohatý, L., Neumann, E., Engelen, B., and Pietsch, U., 2009, “Investigations of the Bond-Selective Response in a Piezoelectric $Li_2SO_4{\cdot}H_2O$ Crystal to an Applied External Electric Field,” Acta Crystallogr. Sect. A, **65**, pp. 267–275.

[24] Gorfman, S., Schmidt, O., Tsirelson, V. G., Ziolkowski, M., and Pietsch, U., 2013, “Crystallography under External Electric Field,” Zeitschrift Für Anorg. Und Allg. Chemie, **639**(11), pp. 1953–1962.

[25] Gorfman, S., 2014, “Sub-Microsecond X-Ray Crystallography: Techniques, Challenges and Applications for Materials Science,” Crystallogr. Rev., **20**(3), pp. 210–232.

[26] Ejdrup, T., Lemke, H. T., Haldrup, K., Nielsen, T. N., Arms, D. A., Walko, D. A., Miceli, A., Landahl, E. C., Dufresne, E. M., and Nielsen, M. M., 2009, “Picosecond Time-Resolved Laser pump/X-Ray Probe Experiments Using a Gated Single-Photon-Counting Area Detector,” J. Synchrotron Radiat., **16**, pp. 387–390.

[27] Navirian, H. A., Herzog, M., Goldshteyn, J., Leitenberger, W., Vrejoiu, I., Khakhulin, D., Wulff, M., Shayduk, R., Gaal, P., and Bargheer, M., 2011, “Shortening X-Ray Pulses for Pump-Probe Experiments at Synchrotrons,” J. Appl. Phys., **109**, p. 126104.

[28] Reusch, T., Osterhoff, M., Agricola, J., and Salditt, T., 2014, “Pulse-Resolved Multi-Photon X-Ray Detection at 31 MHz Based on a Quadrant Avalanche Photodiode,” J. Synchrotron Radiat., **21**, pp. 708–715.

[29] Zolotoyabko, E., Quintana, J. P., Hoerman, B. H., and Wessels, B. W., 2002,

"Fast Time-Resolved X-Ray Diffraction in $BaTiO_3$ Films Subjected to a Strong High-Frequency Electric Field," Appl. Phys. Lett., **80**, p. 3159.

[30] Grigoriev, A., Do, D.-H., Kim, D. M., Eom, C.-B., Evans, P. G., Adams, B., and Dufresne, E. M., 2006, "Subnanosecond Piezoelectric X-Ray Switch," Appl. Phys. Lett., **89**, p. 21109.

[31] Sakata, O., Yasui, S., Yamada, T., Yabashi, M., Kimura, S., and Funakubo, H., 2010, "In-Situ Lattice-Strain Analysis of a Ferroelectric Thin Film under an Applied Pulse Electric Field," AIP Conf. Proc., **1234**, p. 151.

[32] Nakashima, S., Fujisawa, H., Shimizu, M., Sakata, O., Yamada, T., Funakubo, H., Park, J. M., Kanashima, T., and Okuyama, M., 2011, "X-Ray Diffraction Study of Electric-Field-Induced Strains in Polycrystalline $BiFeO_3$ Thin Films at Low Temperatures by Using Synchrotron Radiation," J. Korean Phys. Soc., **59**(3), pp. 2556–2559.

[33] Jo, J. Y., Chen, P., Sichel, R. J., Callori, S. J., Sinsheimer, J., Dufresne, E. M., Dawber, M., and Evans, P. G., 2011, "Nanosecond Dynamics of Ferroelectric/Dielectric Superlattices," Phys. Rev. Lett., **107**, p. 55501.

[34] Chen, P., Jo, J. Y., Lee, H. N., Dufresne, E. M., Nakhmanson, S. M., and Evans, P. G., 2012, "Domain- and Symmetry-Transition Origins of Reduced Nanosecond Piezoelectricity in Ferroelectric/dielectric Superlattices," New J. Phys., **14**, p. 13034.

[35] Fujisawa, T., Ehara, Y., Yasui, S., Kamo, T., Yamada, T., Sakata, O., and Funakubo, H., 2014, "Direct Observation of Intrinsic Piezoelectricity of $Pb(Zr,Ti)O_3$ by Time-Resolved X-Ray Diffraction Measurement Using Single-Crystalline Films," Appl. Phys. Lett., **105**, p. 12905.

[36] Cosgriff, M. P., Chen, P., Lee, S. S., Lee, H. J., Kuna, L., Pitike, K. C., Louis, L., Parker, W. D., Tajiri, H., Nakhmanson, S. M., Jo, J. Y., Chen, Z., Chen, L., and Evans, P. G., 2016, "Nanosecond Phase Transition Dynamics in Compressively Strained Epitaxial $BiFeO_3$," Adv. Electron. Mater., **2**, p. 1500204.

[37] Jones, J. L., Hoffman, M., Daniels, J. E., and Studer, A. J., 2006, "Direct Measurement of the Domain Switching Contribution to the Dynamic Piezoelectric Response in Ferroelectric Ceramics," Appl. Phys. Lett., **89**, p. 92901.

[38] Daniels, J. E., Finlayson, T. R., Studer, A. J., Hoffman, M., and Jones, J. L., 2007, “Time-Resolved Diffraction Measurements of Electric-Field-Induced Strain in Tetragonal Lead Zirconate Titanate,” J. Appl. Phys., **101**, p. 94104.

[39] Daniels, J. E., Pramanick, A., and Jones, J. L., 2009, “Time-Resolved Characterization of Ferroelectrics Using High-Energy X-Ray Diffraction,” IEEE Trans. Ultrason. Ferroelectr. Freq. Control, **56**(8), pp. 1539–1545.

[40] Pramanick, A., Daniels, J. E., and Jones, J. L., 2009, “Subcoercive Cyclic Electrical Loading of Lead Zirconate Titanate Ceramics II: Time-Resolved X-Ray Diffraction,” J. Am. Ceram. Soc., **92**(10), pp. 2300–2310.

[41] Pramanick, A., Prewitt, A. D., Cottrell, M. A., Lee, W., Studer, A. J., An, K., Hubbard, C. R., and Jones, J. L., 2010, “In Situ Neutron Diffraction Studies of a Commercial, Soft Lead Zirconate Titanate Ceramic: Response to Electric Fields and Mechanical Stress,” Appl. Phys. A, **99**, pp. 557–564.

[42] Jones, J. L., Aksel, E., Tutuncu, G., Usher, T.-M., Chen, J., Xing, X., and Studer, A. J., 2012, “Domain Wall and Interphase Boundary Motion in a Two-Phase Morphotropic Phase Boundary Ferroelectric: Frequency Dispersion and Contribution to Piezoelectric and Dielectric Properties,” Phys. Rev. B, **86**, p. 24104.

[43] Tutuncu, G., Damjanovic, D., Chen, J., and Jones, J. L., 2012, “Deaging and Asymmetric Energy Landscapes in Electrically Biased Ferroelectrics,” Phys. Rev. Lett., **108**, p. 177601.

[44] Seshadri, S. B., Prewitt, A. D., Studer, A. J., Damjanovic, D., and Jones, J. L., 2013, “An in-Situ Diffraction Study of Domain Wall Motion Contributions to the Frequency Dispersion of the Piezoelectric Coefficient in Lead Zirconate Titanate,” Appl. Phys. Lett., **102**, p. 42911.

[45] Daniels, J. E., Cozzan, C., Ukritnukun, S., Tutuncu, G., Andrieux, J., Glaum, J., Dosch, C., Jo, W., and Jones, J. L., 2014, “Two-Step Polarization Reversal in Biased Ferroelectrics,” J. Appl. Phys., **115**, p. 224104.

[46] Esteves, G., Fancher, C. M., and Jones, J. L., 2015, “In Situ Characterization of Polycrystalline Ferroelectrics Using X-Ray and Neutron Diffraction,” J. Mater. Res., **30**(3), pp. 340–356.

[47] Tutuncu, G., Fan, L., Chen, J., Xing, X., and Jones, J. L., 2014, "Extensive Domain Wall Motion and Deaging Resistance in Morphotropic $0.55Bi(Ni_{1/2}Ti_{1/2})O_3$-$0.45PbTiO_3$ Polycrystalline Ferroelectrics," Appl. Phys. Lett., **104**, p. 132907.

[48] Harrison, R. J., Redfern, S. A. T., Buckley, A., and Salje, E. K. H., 2004, "Application of Real-Time, Stroboscopic X-Ray Diffraction with Dynamical Mechanical Analysis to Characterize the Motion of Ferroelastic Domain Walls," J. Appl. Phys., **95**, p. 1706.

[49] Navirian, H., Enquist, H., Nüske, R., Jurgilaitis, A., Von Korff Schmising, C., Sondhauss, P., and Larsson, J., 2010, "Acoustically Driven Ferroelastic Domain Switching Observed by Time-Resolved X-Ray Diffraction," Phys. Rev. B, **81**, p. 24113.

[50] Moriyoshi, C., Hiramoto, S., Ohkubo, H., Kuroiwa, Y., Osawa, H., Sugimoto, K., Kimura, S., Takata, M., Kitanaka, Y., Noguchi, Y., and Miyayama, M., 2011, "Synchrotron Radiation Study on Time-Resolved Tetragonal Lattice Strain of $BaTiO_3$ under Electric Field," Jpn. J. Appl. Phys., **50**, p. 09NE05.

[51] Wooldridge, J., Ryding, S., Brown, S., Burnett, T. L., Cain, M. G., Cernik, R., Hino, R., Stewart, M., and Thompson, P., 2012, "Simultaneous Measurement of X-Ray Diffraction and Ferroelectric Polarization Data as a Function of Applied Electric Field and Frequency," J. Synchrotron Radiat., **19**, pp. 710–716.

[52] Vecchini, C., Thompson, P., Stewart, M., Muñiz-Piniella, A., McMitchell, S. R. C., Wooldridge, J., Lepadatu, S., Bouchenoire, L., Brown, S., Wermeille, D., Bikondoa, O., Lucas, C. A., Hase, T. P. A., Lesourd, M., Dontsov, D., and Cain, M. G., 2015, "Simultaneous Dynamic Electrical and Structural Measurements of Functional Materials," Rev. Sci. Instrum., **86**, p. 103901.

[53] Griffiths, D. J., 1999, *Introduction to Electrodynamics*, Prentice Hall, New Jersey.

[54] Heywang, W., Lubitz, K., and Wersing, W., 2008, *Piezoelectricity: Evolution and Future of a Technology*, Springer, Berlin.

[55] Jona, F., and Shirane, G., 1962, *Ferroelectric Crystals*, Pergamon Press, Oxford.

[56] Newnham, R. E., 2005, *Properties of Materials: Anisotropy, Symmetry, Structure*, Oxford University Press, Oxford.

[57] Nye, F., 1985, *Physical Properties of Crystals: Their Representation by Tensors and Matrices*, Oxford University Press, Oxford.

[58] Rabe, K. M., Ahn, C. H., and Triscone, J.-M., 2007, *Physics of Ferroelectrics: A Modern Perspective*, Springer, Berlin.

[59] Devonshire, A. F., 1954, “Theory of Ferroelectrics,” Adv. Phys., **3**(10), pp. 85–130.

[60] Curie, J., and Curie, P., 1880, “Développement, Par Pression, de L’électricité Polaire Dans Les Cristaux Hémièdres À Faces Inclines,” Comptes rendus (in French), **91**, pp. 294–295.

[61] De Graef, M., and McHenry, M. E., 2012, *Structure of Materials: An Introduction to Crystallography, Diffraction, and Symmetry*, Cambridge University Press, Cambridge.

[62] Khanbabaee, B., Mehner, E., Richter, E., Hanzig, J., Zschornak, M., Pietsch, U., Stöcker, H., Leisegang, T., Meyer, D. C., and Gorfman, S., 2016, “Large Piezoelectricity in Electric-Field Modified Single Crystals of $SrTiO_3$,” Appl. Phys. Lett., **109**, p. 222901.

[63] Lines, M. E., and Glass, A. M., 2000, *Principles and Applications of Ferroelectrics and Related Materials*, Oxford University Press, Oxford.

[64] Xu, Y., 1991, *Ferroelectric Materials and Their Applications*, North-Holland, Amsterdam.

[65] Jin, L., Li, F., and Zhang, S., 2014, “Decoding the Fingerprint of Ferroelectric Loops: Comprehension of the Material Properties and Structures,” J. Am. Ceram. Soc., **97**(1), pp. 1–27.

[66] Sawyer, C. B., and Tower, C. H., 1930, “Rochelle Salt as a Dielectric,” Phys. Rev., **35**, p. 269.

[67] Damjanovic, D., 2009, “Comments on Origins of Enhanced Piezoelectric Properties in Ferroelectrics,” IEEE Trans. Ultrason. Ferroelectr. Freq. Control, **56**(8), pp. 1574–1585.

[68] Ahart, M., Somayazulu, M., Cohen, R. E., Ganesh, P., Dera, P., Mao, H.-K., Hemley, R. J., Ren, Y., Liermann, P., and Wu, Z., 2008, “Origin of Morphotropic

Phase Boundaries in Ferroelectrics," Nature, **451**, pp. 545–548.

[69] Jaffe, B., Roth, R. S., and Marzullo, S., 1954, "Piezoelectric Properties of Lead Zirconate Titanate Solid-Solution Ceramics," J. Appl. Phys., **25**, pp. 809–810.

[70] Cox, D. E., Noheda, B., Shirane, G., Uesu, Y., Fujishiro, K., and Yamada, Y., 2001, "Universal Phase Diagram for High-Piezoelectric Perovskite Systems," Appl. Phys. Lett., **79**, p. 400.

[71] Guo, R., Cross, L. E., Park, S.-E., Noheda, B., Cox, D. E., and Shirane, G., 2000, "Origin of the High Piezoelectric Response in $PbZr_{1-x}Ti_xO_3$," Phys. Rev. Lett., **84**, p. 5423.

[72] Noheda, B., Gonzalo, J. A., Cross, L. E., Guo, R., Park, S.-E., Cox, D. E., and Shirane, G., 2000, "Tetragonal-to-Monoclinic Phase Transition in a Ferroelectric Perovskite: The Structure of $PbZr_{0.52}Ti_{0.48}O_3$," Phys. Rev. B, **61**, p. 8687.

[73] Zhang, N., Yokota, H., Glazer, A. M., Ren, Z., Keen, D. A., Keeble, D. S., Thomas, P. A., and Ye, Z.-G., 2014, "The Missing Boundary in the Phase Diagram of $PbZr_{1-x}Ti_xO_3$," Nat. Commun., **5**, p. 5231.

[74] Noheda, B., Cox, D. E., Shirane, G., Park, S.-E., Cross, L. E., and Zhong, Z., 2001, "Polarization Rotation via a Monoclinic Phase in the Piezoelectric 92% $PbZn_{1/3}Nb_{2/3}O_3$-8% $PbTiO_3$," Phys. Rev. Lett., **86**, p. 3891.

[75] Vanderbilt, D., and Cohen, M. H., 2001, "Monoclinic and Triclinic Phases in Higher-Order Devonshire Theory," Phys. Rev. B, **63**, p. 94108.

[76] La-Orauttapong, D., Noheda, B., Ye, Z.-G., Gehring, P. M., Toulouse, J., Cox, D. E., and Shirane, G., 2002, "Phase Diagram of the Relaxor Ferroelectric $(1-x)Pb(Zn_{1/3}Nb_{2/3})O_3 - xPbTiO_3$," Phys. Rev. B, **65**, p. 144101.

[77] Fu, H., and Cohen, R. E., 2000, "Polarization Rotation Mechanism for Ultrahigh Electromechanical Response in Single-Crystal Piezoelectrics," Nature, **403**, pp. 281–283.

[78] Cohen, R. E., 2006, "Materials Science: Relaxors Go Critical," Nature, **441**, pp. 941–942.

[79] Benes, E., Gröschl, M., Burger, W., and Schmid, M., 1995, "Sensors Based on Piezoelectric Resonators," Sensors Actuators A Phys., **48**(1), pp. 1–21.

[80] Jaffe, H., and Berlincourt, D. A., 1965, “Piezoelectric Transducer Materials,” Proc. IEEE, **53**(10), pp. 1372–1386.

[81] Benajes, J., Molina, S., Novella, R., Amorim, R., Ben Hadj Hamouda, H., and Hardy, J. P., 2010, “Comparison of Two Injection Systems in an HSDI Diesel Engine Using Split Injection and Different Injector Nozzles,” Int. J. Automot. Technol., **11**(2), pp. 139–146.

[82] Randall, C. A., Kelnberger, A., Yang, G. Y., Eitel, R. E., and Shrout, T. R., 2005, “High Strain Piezoelectric Multilayer Actuators - A Material Science and Engineering Challenge,” J. Electroceramics, **14**(3), pp. 177–191.

[83] Lin, C.-J., and Yang, S.-R., 2006, “Precise Positioning of Piezo-Actuated Stages Using Hysteresis-Observer Based Control,” Mechatronics, **16**(7), pp. 417–426.

[84] Chung, S. Y., Kim, S., Lee, J. H., Kim, K., Kim, S. W., Kang, C. Y., Yoon, S. J., and Kim, Y. S., 2012, “All-Solution-Processed Flexible Thin Film Piezoelectric Nanogenerator,” Adv. Mater., **24**(45), pp. 6022–6027.

[85] Park, K. I., Lee, M., Liu, Y., Moon, S., Hwang, G. T., Zhu, G., Kim, J. E., Kim, S. O., Kim, D. K., Wang, Z. L., and Lee, K. J., 2012, “Flexible Nanocomposite Generator Made of $BaTiO_3$ Nanoparticles and Graphitic Carbons,” Adv. Mater., **24**(22), pp. 2999–3004.

[86] Amin Karami, M., and Inman, D. J., 2012, “Powering Pacemakers from Heartbeat Vibrations Using Linear and Nonlinear Energy Harvesters,” Appl. Phys. Lett., **100**(4), p. 42901.

[87] Watson, B., Friend, J., and Yeo, L., 2009, “Piezoelectric Ultrasonic Micro/milli-Scale Actuators,” Sensors Actuators A Phys., **152**(2), pp. 219–233.

[88] Muralt, P., 2000, “Ferroelectric Thin Films for Micro-Sensors and Actuators: A Review,” J. Micromechanics Microengineering, **10**(2), pp. 136–146.

[89] Momma, K., and Izumi, F., 2011, “VESTA 3 for Three-Dimensional Visualization of Crystal, Volumetric and Morphology Data,” J. Appl. Crystallogr., **44**, pp. 1272–1276.

[90] Ashcroft, N. W., and Mermin, N. D., 1976, *Solid State Physics*, Saunders College, Philadelphia.

[91] Giacovazzo, C., 2011, *Fundamentals of Crystallography*, Oxford University Press, Oxford.

[92] Hammond, C., 2015, *The Basics of Crystallography and Diffraction*, Oxford University Press, Oxford.

[93] Jackson, J. D., 1998, *Classical Electrodynamics*, Wiley, New York.

[94] Warren, B. E., 1990, *X-Ray Diffraction*, Dover Publications, New York.

[95] Su, Z., and Coppens, P., 1997, "Relativistic X-Ray Elastic Scattering Factors for Neutral Atoms Z=1-54 from Multiconfiguration Dirac-Fock Wavefunctions in the 0-12 $Å^{-1}$ Sin θ / λ Range, and Six-Gaussian Analytical Expressions in the 0-6 $Å^{-1}$ Range," Acta Crystallogr. Sect. A, **53**, pp. 749–762.

[96] Macchi, P., and Coppens, P., 2001, "Relativistic Analytical Wave Functions and Scattering Factors for Neutral Atoms beyond Kr and for All Chemically Important Ions up to I^-," Acta Crystallogr. Sect. A, **57**, pp. 656–662.

[97] Prince, E., ed., 2004, *International Tables for Crystallography: Volume C*, Kluwer Academic, Dordrecht.

[98] Gorfman, S., Choe, H., Shvartsman, V. V., Ziolkowski, M., Vogt, M., Strempfer, J., Łukasiewicz, T., Pietsch, U., and Dec, J., 2015, "Time-Resolved X-Ray Diffraction Reveals the Hidden Mechanism of High Piezoelectric Activity in a Uniaxial Ferroelectric," Phys. Rev. Lett., **114**, p. 97601.

[99] Rietveld, H. M., 1969, "A Profile Refinement Method for Nuclear and Magnetic Structures," J. Appl. Crystallogr., **2**, pp. 65–71.

[100] Choe, H., Gorfman, S., Heidbrink, S., Pietsch, U., Vogt, M., Winter, J., and Ziolkowski, M., 2017, "Multichannel FPGA-Based Data-Acquisition-System for Time-Resolved Synchrotron Radiation Experiments," IEEE Trans. Nucl. Sci., **64**(6), pp. 1320–1326.

[101] Choe, H., Gorfman, S., Hinterstein, M., Ziolkowski, M., Knapp, M., Heidbrink, S., Vogt, M., Bednarcik, J., Berghäuser, A., Ehrenberg, H., and Pietsch, U., 2015, "Combining High Time and Angular Resolutions: Time-Resolved X-Ray Powder Diffraction Using a Multi-Channel Analyser Detector," J. Appl. Crystallogr., **48**, pp. 970–974.

[102] Gorfman, S., Simons, H., Iamsasri, T., Prasertpalichat, S., Cann, D. P., Choe, H., Pietsch, U., Watier, Y., and Jones, J. L., 2016, “Simultaneous Resonant X-Ray Diffraction Measurement of Polarization Inversion and Lattice Strain in Polycrystalline Ferroelectrics,” Sci. Rep., **6**, p. 20829.

[103] Fitch, A. N., 2004, “The High Resolution Powder Diffraction Beam Line at ESRF,” J. Res. Natl. Inst. Stand. Technol., **109**, pp. 133–142.

[104] Hodeau, J.-L., Bordet, P., Anne, M., Prat, A., Fitch, A. N., Dooryhee, E., Vaughan, G., and Freund, A. K., 1998, “Nine Crystal Multianalyzer Stage for High-Resolution Powder Diffraction between 6 keV and 40 keV,” Proc. SPIE, **3448**, pp. 353–361.

[105] Horst, A., Berghaeuser, A., Hinterstein, M., and Knapp, M., 2012, “MULTIKRISTALL-ANALYSATOR-DETEKTORSYSTEM FÜR 60 keV.”

[106] Usher, T.-M., Levin, I., Daniels, J. E., and Jones, J. L., 2015, “Electric-Field-Induced Local and Mesoscale Structural Changes in Polycrystalline Dielectrics and Ferroelectrics,” Sci. Rep., **5**, p. 14678.

[107] Jankowiak, A., “Operating Modi BESSY II: Standard Fill Pattern (Multi Bunch Hybrid)” [Online]. Available: http://www.helmholtz-berlin.de/quellen/bessy/betrieb-beschleuniger/betriebsmodi_en.html. [Accessed: 14-Feb-2017].

[108] Choe, H., Heidbrink, S., Ziolkowski, M., Pietsch, U., Dyadkin, V., Gorfman, S., and Chernyshov, D., 2017, “A Microcontroller for in Situ Single-Crystal Diffraction Measurements with a PILATUS-2M Detector under an Alternating Electric Field,” J. Appl. Crystallogr., **50**, pp. 975–977.

[109] Wang, Y., Chen, L., Yuan, G., Luo, H., Li, J., and Viehland, D., 2016, “Large Field-Induced-Strain at High Temperature in Ternary Ferroelectric Crystals,” Sci. Rep., **6**, p. 35120.

[110] Dyadkin, V., Pattison, P., Dmitriev, V., and Chernyshov, D., 2016, “A New Multipurpose Diffractometer PILATUS SNBL,” J. Synchrotron Radiat., **23**, pp. 825–829.

[111] Vergentev, T. Y., Dyadkin, V., and Chernyshov, D. Y., 2015, “In Situ Cell for X-Ray Single-Crystal Diffraction Experiment at Electric Field,” J. Surf. Investig. X-

ray, Synchrotron Neutron Tech., **9**(3), pp. 436–441.

[112] Vergentev, T., Bronwald, I., Chernyshov, D., Gorfman, S., Ryding, S. H. M., Thompson, P., and Cernik, R. J., 2016, "A Rapid Two-Dimensional Data Collection System for the Study of Ferroelectric Materials under External Applied Electric Fields," J. Appl. Crystallogr., **49**, pp. 1501–1507.

[113] Vakhrushev, S. B., Isupov, V. A., Kvyatkovsky, B. E., Okuneva, N. M., Pronin, I. P., Smolensky, G. A., and Syrnikov, P. P., 1985, "Phase Transitions and Soft Modes in Sodium Bismuth Titanate," Ferroelectrics, **63**(1), pp. 153–160.

[114] Roleder, K., Franke, I., Glazer, A. M., Thomas, P. A., Miga, S., and Suchanicz, J., 2002, "The Piezoelectric Effect in $Na_{0.5}Bi_{0.5}TiO_3$ Ceramics," J. Phys. Condens. Matter, **14**(21), p. 314.

[115] McQuade, R. R., and Dolgos, M. R., 2016, "A Review of the Structure-Property Relationships in Lead-Free Piezoelectric (1-x)$Na_{0.5}Bi_{0.5}TiO_3$-(x)$BaTiO_3$," J. Solid State Chem., **3**, pp. 140–147.

[116] Takenaka, T., Maruyama, K., and Sakata, K., 1991, "($Bi_{1/2}Na_{1/2}$)TiO_3-$BaTiO_3$ System for Lead-Free Piezoelectric Ceramics," Jpn. J. Appl. Phys., **30**(9B), pp. 2236–2239.

[117] Takenaka, T., Nagata, H., and Hiruma, Y., 2008, "Current Developments and Prospective of Lead-Free Piezoelectric Ceramics," Jpn. J. Appl. Phys., **47**(5), p. 37873801.

[118] Panda, P. K., 2009, "Review: Environmental Friendly Lead-Free Piezoelectric Materials," J. Mater. Sci., **44**(19), pp. 5049–5062.

[119] Rödel, J., Jo, W., Seifert, K. T. P., Anton, E.-M., Granzow, T., and Damjanovic, D., 2009, "Perspective on the Development of Lead-Free Piezoceramics," J. Am. Ceram. Soc., **92**(6), pp. 1153–1177.

[120] Jones, G. O., and Thomas, P. A., 2002, "Investigation of the Structure and Phase Transitions in the Novel A-Site Substituted Distorted Perovskite Compound $Na_{0.5}Bi_{0.5}TiO_3$," Acta Crystallogr. Sect. B, **58**, pp. 168–178.

[121] Gorfman, S., and Thomas, P. A., 2010, "Evidence for a Non-Rhombohedral Average Structure in the Lead-Free Piezoelectric Material $Na_{0.5}Bi_{0.5}TiO_3$," J. Appl. Crystallogr., **43**, pp. 1409–1414.

[122] Aksel, E., Forrester, J. S., Kowalski, B., Jones, J. L., and Thomas, P. A., 2011, "Phase Transition Sequence in Sodium Bismuth Titanate Observed Using High-Resolution X-Ray Diffraction," Appl. Phys. Lett., **99**, p. 222901.

[123] Gorfman, S., Glazer, A. M., Noguchi, Y., Miyayama, M., Luo, H., and Thomas, P. A., 2012, "Observation of a Low-Symmetry Phase in $Na_{0.5}Bi_{0.5}TiO_3$ Crystals by Optical Birefringence Microscopy," J. Appl. Crystallogr., **45**, pp. 444–452.

[124] Levin, I., and Reaney, I. M., 2012, "Nano- and Mesoscale Structure of $Na_{1/2}Bi_{1/2}TiO_3$: A TEM Perspective," Adv. Funct. Mater., **22**(16), pp. 3445–3452.

[125] Ma, C., Guo, H., and Tan, X., 2013, "A New Phase Boundary in $(Bi_{1/2}Na_{1/2})TiO_3$-$BaTiO_3$ Revealed via a Novel Method of Electron Diffraction Analysis," Adv. Funct. Mater., **23**(42), pp. 5261–5266.

[126] Kitanaka, Y., Yanai, K., Noguchi, Y., Miyayama, M., Kagawa, Y., Moriyoshi, C., and Kuroiwa, Y., 2014, "Non-180° Polarization Rotation of Ferroelectric $(Bi_{0.5}Na_{0.5})TiO_3$ Single Crystals under Electric Field," Phys. Rev. B, **89**, p. 104104.

[127] Ge, W., Liu, H., Zhao, X., Zhong, W., Pan, X., He, T., Lin, D., Xu, H., Jiang, X., and Luo, H., 2008, "Growth, Optical and Electrical Properties of Pure and Mn-Doped $Na_{0.5}Bi_{0.5}TiO_3$ Lead-Free Piezoelectric Crystals," J. Alloys Compd., **462**(1), pp. 256–261.

[128] Ge, W., Li, J., Viehland, D., and Luo, H., 2010, "Influence of Mn Doping on the Structure and Properties of $Na_{0.5}Bi_{0.5}TiO_3$ Single Crystals," J. Am. Ceram. Soc., **93**, pp. 1372–1377.

[129] MATLAB, "Find Minimum of Constrained Nonlinear Multivariable Function - Fmincon" [Online]. Available: https://www.mathworks.com/help/optim/ug/fmincon.html.

[130] Hiruma, Y., Nagata, H., and Takenaka, T., 2009, "Thermal Depoling Process and Piezoelectric Properties of Bismuth Sodium Titanate Ceramics," J. Appl. Phys., **105**, p. 84112.

[131] Hiruma, Y., Nagata, H., Hidaka, Y., Tsukada, S., Kojima, S., and Takenaka, T., 2010, "Depolarization Temperatures and Piezoelectric Properties of $(Bi_{0.5}Na_{0.5})TiO_3$ Ceramics and Single Crystal," Ferroelectrics, **404**(1), pp. 162–166.

[132] Foronda, H., Deluca, M., Aksel, E., Forrester, J. S., and Jones, J. L., 2014, "Thermally-Induced Loss of Piezoelectricity in Ferroelectric $Na_{0.5}Bi_{0.5}TiO_3$-$BaTiO_3$," Mater. Lett., **115**, pp. 132–135.

[133] Kreisel, J., Bouvier, P., Dkhil, B., Thomas, P. A., Glazer, A. M., Welberry, T. R., Chaabane, B., and Mezouar, M., 2003, "High-Pressure X-Ray Scattering of Oxides with a Nanoscale Local Structure: Application to $Na_{1/2}Bi_{1/2}TiO_3$," Phys. Rev. B, **68**, p. 14113.

[134] Thomas, P. A., Trujillo, S., Boudard, M., Gorfman, S., and Kreisel, J., 2010, "Diffuse X-Ray Scattering in the Lead-Free Piezoelectric Crystals $Na_{1/2}Bi_{1/2}TiO_3$ and Ba-Doped $Na_{1/2}Bi_{1/2}TiO_3$," Solid State Sci., **12**(3), pp. 311–317.

[135] Gorfman, S., Keeble, D. S., Bombardi, A., and Thomas, P. A., 2015, "Topology and Temperature Dependence of the Diffuse X-Ray Scattering in $Na_{0.5}Bi_{0.5}TiO_3$ Ferroelectric Single Crystals," J. Appl. Crystallogr., **48**, pp. 1543–1550.

[136] Keeble, D. S., Barney, E. R., Keen, D. A., Tucker, M. G., Kreisel, J., and Thomas, P. A., 2013, "Bifurcated Polarization Rotation in Bismuth-Based Piezoelectrics," Adv. Funct. Mater., **23**(2), pp. 185–190.

[137] Ewbank, M. D., Neurgaonkar, R. R., and Cory, W. K., 1987, "Photorefractive Properties of Strontium-barium Niobate," J. Appl. Phys., **62**, p. 374.

[138] Francombe, M. H., 1960, "The Relation between Structure and Ferroelectricity in Lead Barium and Barium Strontium Niobates," Acta Crystallogr., **13**, pp. 131–140.

[139] Glass, A. M., 1969, "Investigation of the Electrical Properties of $Sr_{1-x}Ba_xNb_2O_6$ with Special Reference to Pyroelectric Detection," J. Appl. Phys., **40**, p. 4699.

[140] Matsumoto, K., and Kojima, S., 2015, "Effect of Electric Field on Uniaxial Relaxor Ferroelectric Strontium Barium Niobate," Jpn. J. Appl. Phys., **54**, p. 10NC04.

[141] Neurgaonkar, R. R., and Cory, W. K., 1986, "Progress in Photorefractive Tungsten Bronze Crystals," J. Opt. Soc. Am. B, **3**(2), pp. 274–282.

[142] Paszkowski, R., Wokulska, K. B., Dec, J., and Łukasiewicz, T., 2014, "Precise Lattice Parameter Measurements of $Sr_{0.72}Ba_{0.25}Nb_2O_{5.97}$ Single Crystals," J. Cryst. Growth, **401**, pp. 327–329.

[143] Łukasiewicz, T., Swirkowicz, M. A., Dec, J., Hofman, W., and Szyrski, W., 2008, "Strontium–barium Niobate Single Crystals, Growth and Ferroelectric Properties," J. Cryst. Growth, **310**, pp. 1464–1469.

[144] Woike, T., Petrícek, V., Dusek, M., Hansen, N. K., Fertey, P., Lecomte, C., Arakcheeva, A., Chapuis, G., Imlau, M., and Pankrath, R., 2003, "The Modulated Structure of $Ba_{0.39}Sr_{0.61}Nb_2O_6$. I. Harmonic Solution," Acta Crystallogr. Sect. B, **59**, pp. 28–35.

[145] Jamieson, P. B., Abrahams, S. C., and Bernstein, J. L., 1968, "Ferroelectric Tungsten Bronze-Type Crystal Structures. I. Barium Strontium Niobate $Ba_{0.27}Sr_{0.75}Nb_2O_{5.78}$," J. Chem. Phys., **48**, p. 5048.

[146] Podlozhenov, S., Graetsch, H. A., Schneider, J., Ulex, M., Wöhlecke, M., and Betzler, K., 2006, "Structure of Strontium Barium Niobate $Sr_xBa_{1-x}Nb_2O_6$ (SBN) in the Composition Range $0.32 \leq X \leq 0.82$," Acta Crystallogr. Sect. B, **62**, pp. 960–965.

[147] Waser, R., Böttger, U., and Tiedke, S., eds., 2005, *Polar Oxides: Properties, Characterization, and Imaging*, WILEY-VCH Verlag GmbH & Co.KGaA, Weinheim.

[148] Bhalla, A. S., Guo, R., Cross, L. E., Burns, G., Dacol, F. H., and Neurgaonkar, R. R., 1992, "Glassy Polarization in the Ferroelectric Tungsten Bronze $(Ba,Sr)Nb_2O_6$," J. Appl. Phys., **71**, p. 5591.

[149] Graafsma, H., 1992, "Accurate Determination of Strain Tensors from Small Shifts of Reflections Measured on a Four-Circle Diffractometer," J. Appl. Crystallogr., **25**, p. 372.

[150] Schmidt, O., Gorfman, S., and Pietsch, U., 2008, "Electric-Field-Induced Internal Deformation in Piezoelectric BiB_3O_6 Crystals," Cryst. Res. Technol., **43**, pp. 1126–1132.

[151] Bieker, J., 2015, "Röntgenanalyse Elektromechanischer Kopplungen in Ferroelektrischen Kristallen," Universitätsbibliothek Siegen (in German).

[152] Bieker, J., 2013, "Röntgenstrukturanalyse von Ferroelektrischen Kristallen Unter Anregung Durch Ein Dynamisches Elektrisches Feld," Universitätsbibliothek Siegen (in German).

[153] Taylor, D. V., and Damjanovic, D., 1997, “Evidence of Domain Wall Contribution to the Dielectric Permittivity in PZT Thin Films at Sub-Switching Fields,” J. Appl. Phys., **82**, p. 1973.

[154] Trolier-McKinstry, S., Bassiri-Gharb, N., and Damjanovic, D., 2006, “Piezoelectric Nonlinearity due to Motion of 180° Domain Walls in Ferroelectric Materials at Subcoercive Fields: A Dynamic Poling Model,” Appl. Phys. Lett., **88**, p. 202901.

[155] Damjanovic, D., 1997, “Stress and Frequency Dependence of the Direct Piezoelectric Effect in Ferroelectric Ceramics,” J. Appl. Phys., **82**, p. 1788.

[156] Pramanick, A., Damjanovic, D., Daniels, J. E., Nino, J. C., and Jones, J. L., 2011, “Origins of Electro-Mechanical Coupling in Polycrystalline Ferroelectrics During Subcoercive Electrical Loading,” J. Am. Ceram. Soc., **94**, pp. 293–309.

[157] Xu, R., Liu, S., Grinberg, I., Karthik, J., Damodaran, A. R., Rappe, A. M., and Martin, L. W., 2015, “Ferroelectric Polarization Reversal via Successive Ferroelastic Transitions,” Nat. Mater., **14**, pp. 79–86.

[158] Bokov, A. A., and Ye, Z.-G., 2006, “Recent Progress in Relaxor Ferroelectrics with Perovskite Structure,” J. Mater. Sci., **41**, pp. 31–52.

[159] Daniels, J. E., Jo, W., Rödel, J., Rytz, D., and Donner, W., 2011, “Structural Origins of Relaxor Behavior in a $0.96(Bi_{1/2}Na_{1/2})TiO_3$–$0.04BaTiO_3$ Single Crystal under Electric Field,” Appl. Phys. Lett., **98**, p. 252904.

[160] Stern, E. A., 2004, “Character of Order-Disorder and Displacive Components in Barium Titanate,” Phys. Rev. Lett., **93**, p. 37601.

[161] Zalar, B., Laguta, V. V., and Blinc, R., 2003, “NMR Evidence for the Coexistence of Order-Disorder and Displacive Components in Barium Titanate,” Phys. Rev. Lett., **90**, p. 37601.

[162] Scott, J. F., 2010, “Switching of Ferroelectrics without Domains,” Adv. Mater., **22**, pp. 5315–5317.

[163] Deng, H., Zhang, H., Zhao, X., Chen, C., Wang, X., Li, X., Lin, D., Ren, B., Jia, J., and Luo, H., 2015, “Direct Observation of Monoclinic Ferroelectric Phase and Domain Switching Process in $(K_{0.25}Na_{0.75})NbO_3$ Single Crystals,” CrystEngComm, **17**, pp. 2872–2877.

[164] Ehara, Y., Yasui, S., Nagata, J., Kan, D., Anbusathaiah, V., Yamada, T., Sakata, O., Funakubo, H., and Nagarajan, V., 2011, “Ultrafast Switching of Ferroelastic Nanodomains in Bilayered Ferroelectric Thin Films,” Appl. Phys. Lett., **99**, p. 182906.

[165] Guillot, R., Fertey, P., Hansen, N. K., Allé, P., Elkaím, E., and Lecomte, C., 2004, “Diffraction Study of the Piezoelectric Properties of Low Quartz,” Eur. Phys. J. B, **42**, pp. 373–380.

[166] Bijvoet, J. M., Peerdeman, A. F., and van Bommel, A. J., 1951, “Determination of the Absolute Configuration of Optically Active Compounds by Means of X-Rays,” Nature, **168**, pp. 271–272.

[167] Friedel, G., 1913, “Sur Les Symétries Cristallines Que Peut Révéler La Diffraction Des Rayons X,” Comptes rendus (in French), **157**, pp. 1533–1536.

[168] Azimonte, C., Granado, E., Terashita, H., Park, S., and Cheong, S.-W., 2010, “Polar Atomic Displacements in Multiferroics Observed via Anomalous X-Ray Diffraction,” Phys. Rev. B, **81**, p. 12103.

[169] Grigoriev, A., Do, D.-H., Kim, D. M., Eom, C.-B., Adams, B., Dufresne, E. M., and Evans, P. G., 2006, “Nanosecond Domain Wall Dynamics in Ferroelectric $Pb(Zr,Ti)O_3$ Thin Films,” Phys. Rev. Lett., **96**, p. 187601.

[170] van Reeuwijk, S. J., Karakaya, K., Graafsma, H., and Harkema, S., 2004, “Polarization Switching in $BaTiO_3$ Thin Films Measured by X-Ray Diffraction Exploiting Anomalous Dispersion,” J. Appl. Crystallogr., **37**, pp. 193–199.

[171] Fabrizi, F., Thomas, P. A., Nisbet, G., and Collins, S. P., 2015, “Identification of Inversion Domains in $KTiOPO_4$ via Resonant X-Ray Diffraction,” Acta Crystallogr. Sect. A, **71**, pp. 361–367.

[172] Huang, C.-C., and Cann, D. P., 2008, “Phase Transitions and Dielectric Properties in $Bi(Zn_{1/2}Ti_{1/2})O_3$–$BaTiO_3$ Perovskite Solid Solutions,” J. Appl. Phys., **104**, p. 24117.

[173] Kissel, L., Zhou, B., Roy, S. C., Sen Gupta, S. K., and Pratt, R. H., 1995, “The Validity of Form-Factor, Modified-Form-Factor and Anomalous-Scattering-Factor Approximations in Elastic Scattering Calculations,” Acta Crystallogr. Sect. A, **51**, pp. 271–288.

Acknowledgements

First and foremost, I really would like to express my sincere appreciation and gratitude to my advisers, Ullrich Pietsch and Semën Gorfman, for their all great guidance, comments, helping and research opportunities. I also appreciate all supports and guidance from my committee members.

I would like to many thank the members in the electronics laboratory for great help discussions: Stefan Heidbrink, Marco Vogt, and Jens Winter for very helping with developments of the data-acquisition systems and joining many beamtimes; Michael Ziolkowski for many helpful discussions and comments in this dissertation.

I would like to thank all graduate students and postdocs (even Alumni) in the Solid State Physics group for help discussions and life in Siegen: Johannes Bieker and Behnam Khanbabaee for very helping discussions and joining many times with the time-resolved X-ray diffraction experiments; Ali Abboud, Arman Davtyan, Özgül Öztürk, and Zahra Molla for many helping comments and revisions in this dissertation and life throughout my studies. Ali Al Hassan and Danial Bahrami for very helping discussions and life in Siegen; Eduard Mikayelyan, Linda Grodd, Anton Davydok, Nadia Pashniak, Mohammad Shokr, Mahmoud Al Humaidi, Amir Tosson, and Mona Erfani for being amazing colleagues and friends.

I would like to many thank collaborators from other universities: Hugh Simon from Technical University of Denmark for very helping discussions and joining many times with time-resolved X-ray powder diffraction experiments; Dong Hou from North Carolina State University for preparing BT-BZT samples; Nan Zhang from Xi'an Jiaotong University for strongly helping discussions with several time-resolved single crystal X-ray diffraction experiments; Hiroko Yokota from Chiba University and Tikhon Vergentev from Peter the Great St. Petersburg Polytechnic University for helping with time-resolved three-dimensional reciprocal space mapping experiments; Manuel Hinterstein and Michael Knapp from Karlsruhe Institution of Technology for helping discussions and joining with time-resolved X-ray powder diffraction experiments.

My advisors and I would like to many acknowledge financial support for this research from the the German Federal Ministry of Education and Research (BMBF - Bundesministerium für Bildung und Forschung-Grant No. 05K13PSA).

I would be grateful to Dmitry Chernyshov at the Swiss-Norwegian Beamline (SNBL) BM01 of the European Synchrotron Radiation Facility (ESRF) for providing great assistant during several beamtimes. I would like to thank Andrew Fitch at the ID22 beamline of the ESRF for helping many things during the beamtime. I would like to many thank Genziana Bussone-Grifone at the P08 beamline of the PETRA III synchrotron facility for many helps during the beamtimes. I also would like to thank Wolfram Leitenberger for great helps during the beamitmes at the XPP-KMC3 beamline of the BESSY II synchrotron.

Over the past years, I have learned an incredible amount from all of you. Thank you so much!

Lastly, I really would like to many thank my family for encouraging and supporting me throughout my life; especially I thank Sun, for her love and patience.